sciendo Slovak Journal of Civil Engineering
Vol. 30, 2022, No. 4, 1 – 10
DOI: 10.2478/sjce-2022-0022

THE POTENTIAL AND IMPLICATIONS OF AUTOMATED PRE-PROCESSING OF LIDAR-BASED DIGITAL ELEVATION MODELS FOR LARGE-SCALE ARCHAEOLOGICAL LANDSCAPE ANALYSIS

David, NOVÁK[1], Filip, PRUŽINEC[2*], Tibor, LIESKOVSKÝ[2]

Abstract

LiDAR-derived digital elevation models (DEMs) have transformed the archaeological study of landscape features, broadened our technical capabilities, and enhanced the accuracy with which terrain relief is described. These models also place demands on how researchers and analysts interpret DEM content in the context of the modern landscape. LiDAR-based DEMs contain modern man-made structures that can significantly influence model properties. Although data are usually filtered and some of these artificial features are removed during bare-earth classification, many terrain interventions remain visible. This large-scale case study applies established methods to a freely available DEM of the Czech Republic in an attempt to evaluate differences between original and filtered DEMs. It applies a fully automated filtering procedure using vector topographic maps to avoid manual corrections that would make the procedure problematic when used on a macro scale. The results of our archaeological GIS analysis demonstrate that this procedure, despite its relative simplicity, can achieve a significantly better representation of a landscape compared to that offered by an unfiltered DEM. Finally, we propose a series of future steps with a view to developing a more comprehensive and accurate model and overcoming its limitations.

Address

[1] Institute of Archaeology of the Czech Academy of Sciences, Prague, Czech Republic

[2] Dept. of Theoretical Geodesy and Geoinformatics, Faculty of Civil Engineering, Slovak University of Technology in Bratislava, Slovakia

* ***Corresponding author:*** filip.pruzinec@stuba.sk

Key words

- Landscape archaeology,
- DEM filtering,
- GIS analysis,
- Visibility,
- Land surface curvature,
- Drainage networks
- Czech Republic.

1 INTRODUCTION

During recent decades, light detection and ranging (LiDAR) data has become an integral element of archaeological landscape research (Crutchley, Crow, 2009; Gojda, John, 2013; Posluschny, 2015; Chase et al., 2017; Garstki, 2020). As well as serving the purposes of surveying and documentation, LiDAR data offers significant promise for contemporary landscape analysis and the modeling of terrain attributes in relation to the past. The use of LiDAR-derived digital elevation models (DEM) for the analysis of large landscapes on a national scale has long been hampered by the inaccessibility of data. The situation has changed in recent years (Hobič, 2020). In the Czech Republic, it is now possible to freely obtain a relatively precise LiDAR-derived DEM raster grid through the portal of the Czech State Administration of Land Surveying and Cadastre (http://geoportal.cuzk.cz/). Researchers can now access a simplified Digital Terrain Model of the Czech Republic of the 5th Generation (DMR 5G), which significantly broadens the possibilities for landscape interpretation by facilitating automated algorithmic methods.

Taking advantage of this favorable situation, the Institute of Archaeology of the Czech Academy of Sciences in Prague recently partnered with the Slovak University of Technology to create a set of models for description and analysis of the landscape of the territory of Bohemia. These include a total visibility model (Llobera, 2003; Gillings, 2017; Brughmans et al., 2018), a stream network model (Kuna, Danielisová, 2009; Hengl, Reuter, 2009; Tarboton et al., 2009) and a terrain classification model (Hengl, Reuter, 2009; De Reu et al. 2013; Novák, 2018). In most cases, preparing these types of models on a large scale is time-consuming. The total visibility model in particular presents considerable computational demands (Rášová, 2017; Kuna et al. 2022).

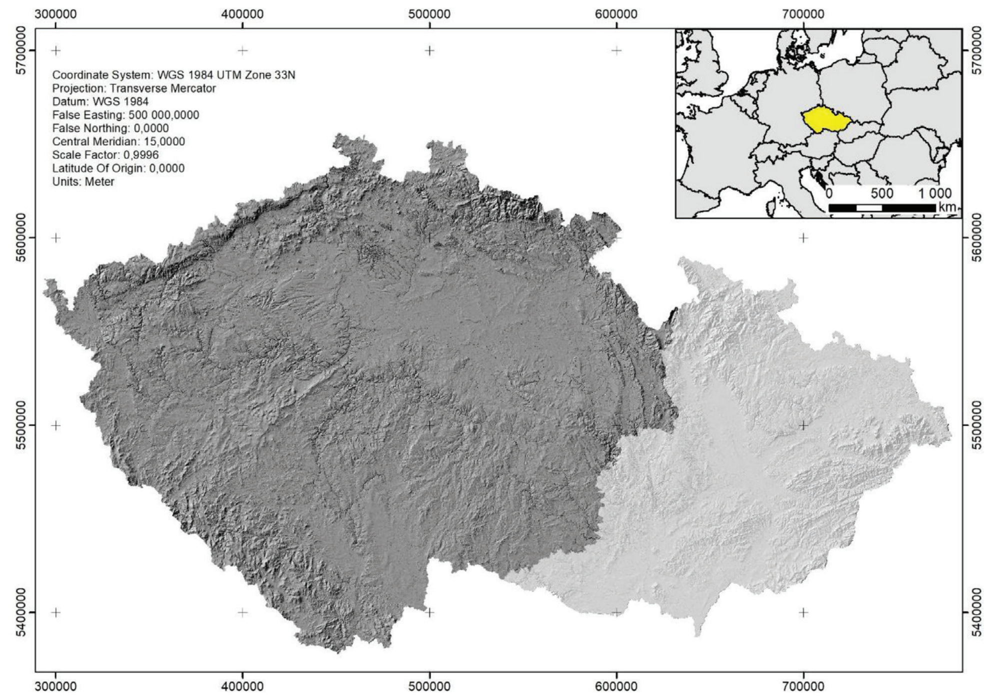

Fig. 1 *Hillshade DMR 5G of the region analyzed (data provided by ČÚZK and EuroGeographics).*

Therefore, the availability of centrally available reference models is of paramount importance for researchers tasked with analyzing datasets to ensure that results can be compared across different projects. The need for this kind of resource corresponds with the mission of the Archaeological Information System of the Czech Republic (https://www.aiscr.cz/), a central infrastructure that supports research in this domain.

The use of LiDAR-derived DEMs, however, also gives rise to a number of complications. An obvious issue that can introduce distortions is the presence of modern artificial features, which can be difficult to distinguish from the natural landscape relief. Bodies of infrastructure constructions, terrains destroyed by mining, built areas, and water management structures are some of the features that negatively impact results. One solution to this problem is to significantly reduce DEM resolution and thus suppress minor anthropogenic features. However, this approach is not recommended due to its tendency to distort the overall digital representation and deform natural landforms. It is also inadequate for handling large terrain interventions. The ideal method is to identify undesirable features and then to remove and replace them by interpolation or using legacy data (e.g. historical maps; see Zwertvaegher et al., 2010; 2013; Werbrouck et al., 2011; Schmidt et al., 2018). This paper presents a procedure used to create a filtered DEM of Bohemia (supplemented by the Vysočina region; Fig. 1) suitable for further spatial analysis. It also compares the extent and nature of the changes to archaeologically relevant properties brought about by the resulting DEM compared to the original unfiltered version. The total area under examination is relatively large at 57,019 km^2, which represents approximately two-thirds of the Czech Republic.

2 THEORY: WHAT TO FILTER OUT AND WHY?

DEMs derived from laser scanning represent a given landscape at the time of data collection and contain features produced by human activity. This is entirely consistent with the idea that – especially in the context of Central Europe – landscapes are a cultural product consisting of a set of artifacts and ecofacts (Kuna 2004; David, Thomas, 2008). Although it is difficult to find a location in the Czech Republic that has not undergone human intervention, from the point of view of analyzing digital landscape models, it is especially important to consider those interventions that have substantially altered the visibility, drainage conditions, and morphology of a landscape. Such interventions can typically be dated to periods close to the present, enabling them to be better distinguished from the natural terrain. Ideally, these features should be identified and removed to bring the resulting DEM surface representation more in line with pre-industrial topography and to reduce the risk of bias in future analyses (Werbrouck et al., 2011).

In addition to human intervention, landscapes have been permanently influenced by natural erosion and accumulation processes, leading to characteristic changes. However, capturing these processes is not the aim of this paper for several reasons. As demonstrated by previous studies (De Smedt et al., 2013; Habicht et al., 2017), the patterns and extent of erosion are strongly dependent on local conditions and should therefore be identified by targeted field surveying such as core sampling or geophysical prospecting. Moreover, erosion and accumulation are dynamic processes, the effects of which vary over time. Therefore, any such landscape reconstruction must take into account the specific time period on which it is modeled. It is also worth noting that in the case of Czech Republic, the effects of erosion processes on the overall landscape are particularly evident in river floodplains with meandering watercourses. Yet, even in these areas, recent interventions fundamentally changing the characteristics of the otherwise relatively well-preserved Holocene relief (see section 3.1) have had a strong impact.

The aim of this study was to identify a means of removing the maximum number of recent intrusions with the highest possible efficiency and the least possible manual interventions. Although previous studies have applied similar approaches, they have been typically limited to much smaller regions with uniform conditions involving the manual processing of input data or other interventions (Werbrouck et al., 2011; Zwertvaegher et al., 2010; 2013; Schmidt et al., 2018). This study evaluates the extent to which commonly available topographic data are adept at correcting DEMs for archaeological purposes. We outline a model that retains most of the qualitative parameters associated with accurate LiDAR images of natural landforms, which are typically represented with significant inaccuracies in DEMs derived from other sources (cf. Novák, 2018).

3 METHODS

Depending on the availability of data and the type of DEM analyzed, approaches adopted by various authors concerning the removal of more recent DEM features vary (Werbrouck et al., 2011; Höfler et al., 2015; Schmidt et al., 2018). The three most common steps involve the use of vector layers as a feature identifier, buffer masking of the affected surface, and interpolation. Other supplementary procedures used to retrieve missing data or to more clearly identify affected surfaces generally require manual work or terrain analysis, measures that can only be accomplished within a reasonable timeframe when analyzing small areas. Given that our area of interest was on a national scale, we selected a straightforward buffering approach based on inverse distance weighting (IDW) interpolation provided by the GDAL *FillNodata* tool. QGIS software (https://qgis.org/) was used for most of the data analysis, with data processing scripted in Python using the GDAL (https://gdal.org/) application programming interface (API).

3.1 Source data

The DEM (DMR 5G) source is a digital representation of a bare earth surface with a vertical accuracy of 0.18 m in an open landscape and 0.3 m in forested areas as well as local deviation extremes of up to 1 m. The model was created from data obtained by airborne laser scanning of the Czech Republic between the years 2010 and 2013, with an average density of points of approx. 1 p/m^2. The DMR 5G model itself is a result of automated filtering, manual corrections, TIN triangulation, and subsequent raw data smoothing. Therefore, the distribution of data points tends to be uneven, and they are only derivatives of the originally measured values (Brázdil et al. 2016). In its basic form, the DMR 5G is distributed as point-based data (LAS) and subject to significant financial charges. As a result, it is practically impossible for this data to be deployed in country-wide analysis. The public version of DMR 5G used in this paper has been downscaled and is distributed as a regular raster grid with a spatial resolution of 2 x 2 m. Considering the complex process of creating the DMR 5G and the possible vertical deviations involved, simplifications present in the public raster grid compared to the full DMR 5G were deemed insignificant, with negligible effects on properties such as visibility, drainage and local curvature.

To determine the modern features of the model, we selected a set of layers (Tab. 1) from the planimetry section of the Fundamental Base of Geographic Data of the Czech Republic (ZABAGED), available online (http://geoportal.cuzk.cz/). Maintained as a seamless database, ZABAGED contains two-dimensional spatial and descriptive information on settlements, communications, utility networks, pipelines, hydrology, administrative units, protected areas, vegetation, surfaces, and terrain relief within the territory of the Czech Republic. The version we used was acquired in 2014 and closely matches the terrain captured by DMR 5G laser scanning.

3.2 Preparation of the clipping mask

We first identified ZABAGED layers that would be most suitable for use as an extraction mask for modern terrain features. Once selected, these ZABAGED vector layers were then grouped according to buffer sizes large enough to cover the affected surface. The layers were divided into 10 groups with buffer sizes of 2, 4, 6, 12, 15, 16, 20, 25, 30 and 50 meters (Tab. 1). To determine the size of the buffer, we analyzed terrain profiles on the vector layers computed from the DEM across different landscape types (Fig. 2). The surfaces affected were generally defined based on an optical assessment of the DEM hillshade visualization. Areas of the natural terrain displaying the highest level of deformation were selected fo a profile analysis. For each ZABAGED layer type, dozens of profiles were monitored in order to determine maximum ranges within the altered terrain. Buffer sizes were then assigned according to the maximum range identified, with an addition of 5–10% based on anticipated deviations for the individual layer type. Due to the unique nature of the possible alterations across different landscape types and the need to estimate the original relief pattern, we primarily relied on qualified estimates based on the above procedure when assigning size groups. Finally, a single polygon mask layer was created as an input to compute the new DEM. The resulting buffer layer contained approx. 3.8 million polygons. Clipping buffers are available through the Zenodo repository (https://doi.org/10.5281/zenodo.6368001).

In the first iteration of the filtering of the model, all water streams and water bodies were included in the layers used for clipping. This approach proved problematic. Firstly, unlike infrastructure and other built features that are subject to targeted planning, the delineation of water streams in ZABAGED compared to DMR 5G is imprecise, mainly due to the dynamically changing stream channels in the natural landscape (Fig. 3). Secondly, although many watercourses pass

Tab. 1 *List of ZABAGED layers used for filtering, descriptions, geometric representations and clipping buffer sizes.*

Layer title	Description	Geometry	Buffer (m)
BudovaBlokBudov	blocks of buildings	polygon	4
Cesta	dirt roads	polyline	12
HaldaOdval	spoil heaps	polygon	2
HradbaVal	ramparts/defensive walls	polyline	12
ChladiciVez	cooling towers	polygon	25
Kolejiste	railway stations	polygon	4
KulnaSklenikFoliovnik	sheds/greenhouses	polygon	4
ParkovisteOdpocivadlo	parking areas	polygon	2
Pesina	footpaths	polyline	6
PovrchovaTezbaLom	open pit mines	polygon	4
PrehradniHrazJez	dams/weirs	polyline	6
RozvalinaZricenina	ruins	polygon	4
SilniceDalnice [D, R]	highways	polyline	50
SilniceDalnice [S1]	roads (first class)	polyline	30
SilniceDalnice [S2]	roads (second class)	polyline	20
SilniceDalnice [S3]	roads (third class)	polyline	15
SilniceNeevidovana	unlisted roads	polyline	12
SilniceVeVystavbe	roads under construction	polyline	20
Silo	silos	polygon	4
Skladka	dumps	polygon	25
TramvajovaDraha	tramways	polyline	12
Ulice	streets	polyline	12
UsazovaciNadrzOdkaliste	sedimentation tanks	polygon	4
ValcovaNadrzZasobnik	cylindrical tanks	polygon	2
VodniPlocha [see 3]	water bodies	polygon	20
Zed	walls	polyline	6
ZeleznicniTrat	railways	polyline	16
ZeleznicniVlecka	railway sidings	polyline	16

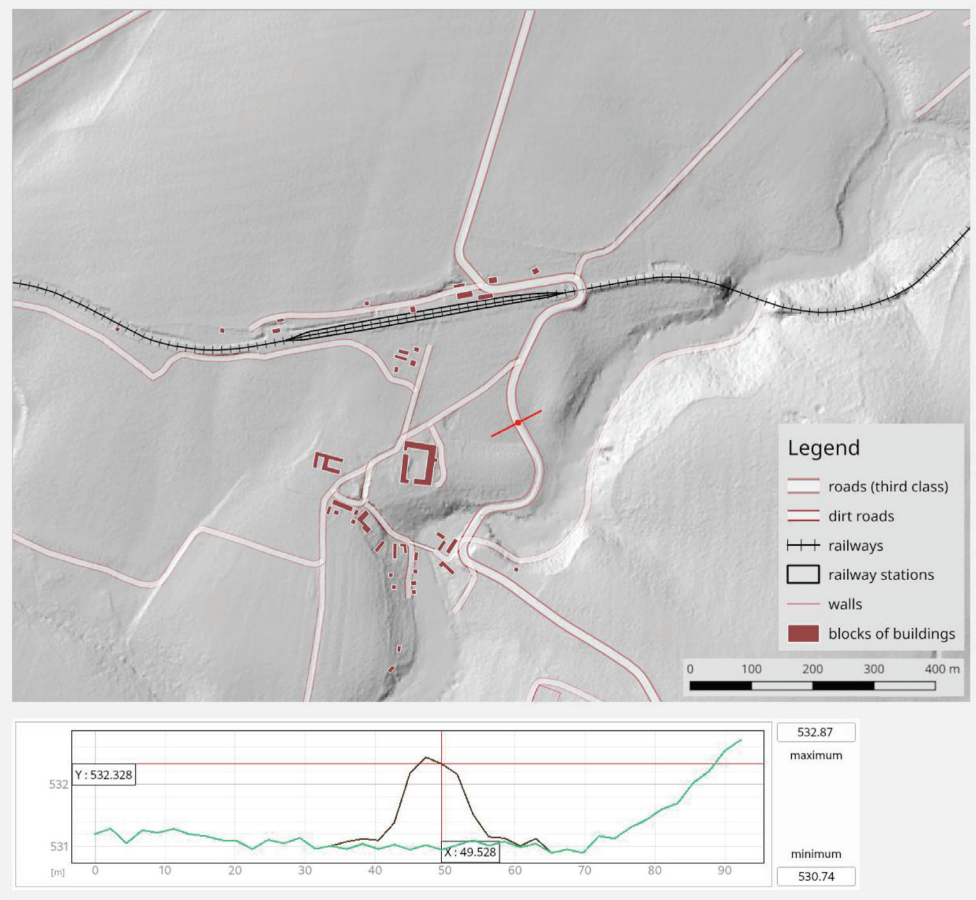

Fig. 2 *Example of a terrain profile (marked in red on map) computed from the input DEM (brown line on graph) and the filtered DEM (green line on graph). The terrain profile of the output DEM displays a continuous surface that most likely reflects the pre-construction terrain (data provided by ČÚZK).*

through artificial channels, a significant proportion of them flow through an open landscape and have thus avoided direct human modification. When these watercourses were used for clipping and subsequent interpolation, the ratio between the correctly removed artificial features and the newly introduced distortions proved unsatisfactory. Especially in the case of complex terrains with narrow, deeply incised valleys, the resulting surfaces were significantly reduced from the original well-defined landforms. Thirdly, in the case of large water bodies, interpolation proved unreliable when filling in missing data. Given these inaccuracies, we found it preferable to preserve the original flat-water surface for further modeling instead of creating an interpolated surface based on an insufficient number of known data points. Thus, water surfaces were only included for still waters with a total perimeter of up to 3000 m. In practical terms, this resulted in the exclusion of large reservoirs, where back-replacement produced the greatest deviations from the expected real terrain, especially reservoirs situated in deep river valleys with steep slopes such as the Vltava Cascade; fishponds and similar smaller features were masked out. Given that there are only six naturally occurring lakes in the country (out of 65,027 filtered water bodies), there was no need to find a solution for the undifferentiated artificial and natural water bodies in ZABAGED.

3.3 Interpolation process

To remove features from the DEM, we used a buffer layer to insert *nodata* values into a GeoTIFF raster (Fig. 4). New values were interpolated using the GDAL FillNodata tool, which uses IDW interpolation to compute unknown values from adjacent pixels within a given search distance specified in cells. For each cell, a four-direction conic search was performed to determine the values for interpolation. Once all the values were interpolated, zero or more smoothing iterations (3x3 average filters on the interpolated cells) were applied to smooth out the artifacts.

Small testing areas of the DEM, which were selected to represent most landscape types, were used to determine a suitable search distance and number of smoothing iterations. We chose a 200-meter (100-cell) search distance and 20 smoothing iterations. However, the buffer layer contained polygons that can generate *nodata* areas in the DEM beyond the scope of the 100-cell search distance specified by the *FillNodata* algorithm. Therefore, these polygons were identified and removed from the processing (Fig. 4). Furthermore, since interpolating values over such large areas can result in inaccuracies, the original values from the output DEM were retained. To identify these features, we converted polygons into closed lines and computed a buffer comprising a search distance radius for every line. Polygons (buffers) containing holes were selected and removed from the buffer layer. For this reason, 4.17% of the total buffer area originally included in the filtering went unresolved. As it was not possible to assess the significance of these individual exclusions, the exact impact of this step on the results could not be quantified. The affected areas, which consist mostly of large-scale mining zones, could be reliably reconstructed using legacy elevation data without the need for interpolation. In regions impacted by large-scale mining (e.g., the northwest Bohemia region), this shortcoming of the model is undoubtedly locally significant; on the other hand, it did not detract from the overall trajectory of the model or the degree of positive changes achieved (see section 4).

The new DEM was processed using a Python script that slices the

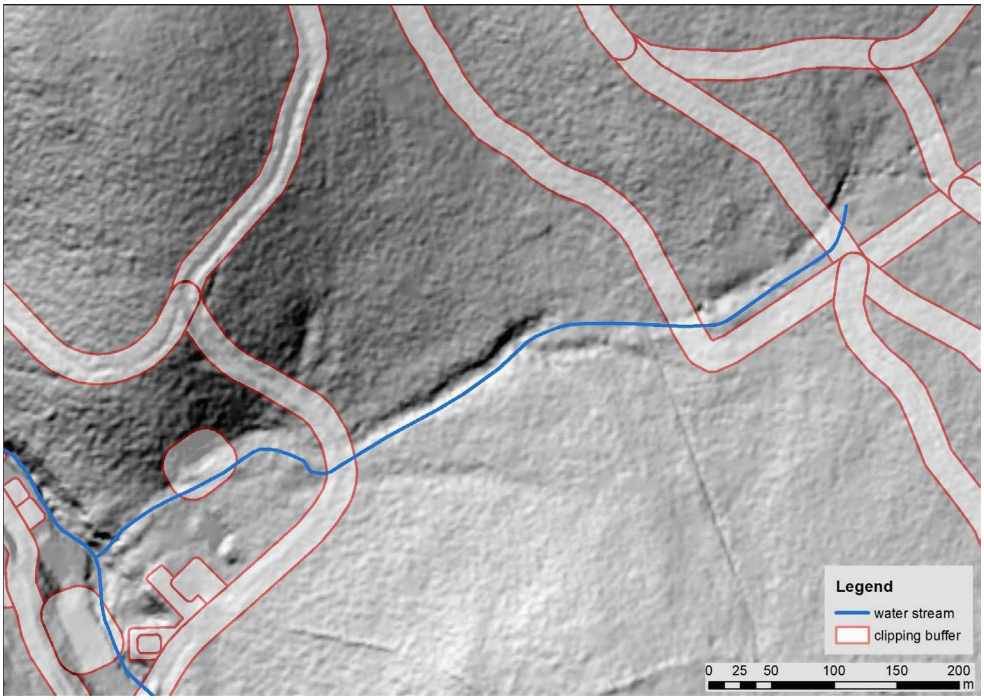

Fig. 3 *The difference in the real position of a watercourse (hillshade DMR 5G) and a stream delineated according to the ZABAGED vector map (blue line). The deviation visible in this section of the stream often exceeds 15 m. Buffers used for clipping are also shown (data provided by ČÚZK).*

DEM into 20 x 16 km raster tiles featuring 200-meter overlays. This ensures seamless merging of the tiles interpolated within a 100-cell search filter. Tiles with a specified extent were created using GDAL Python API's *Translate* function. The same extent was applied as a spatial filter to the mask layer. Where the tiles contained elevation data and polygons remained in the mask layer after applying the filter, the GDAL *RasterizeLayer* function was used to insert *nodata* values to the tile layer using polygons from the mask layer. Finally, the *FillNodata* function was used to interpolate missing values, with the tile cropped by the overlay distance using the *Translate* function. The other option involved merging tiles in this step, thereby saving some processing time; however, replacing an incorrectly processed tile is simpler than processing the whole DEM again in cases where the buffer filtering step did not finish properly. QGIS was used to build a virtual raster, which was then converted into a GeoTIFF. Since the *FillNodata* tool also interpolates values beyond the original border, the merged raster had to be cropped using the original raster value boundary (Fig. 4). To suppress the edge effect, additional data from MERIT DEM (http://hydro.iis.u-tokyo.ac.jp/~yamadai/MERIT_DEM/) was used to interpolate the area close to the Czech border.

The tiling step can be replaced with GDAL command-line tools used directly on the input DEM. However, this tiling approach takes 4-6 hours to process (without tile merging) on an average computer (Intel® Core™ i5-4690 CPU @ 3.50GHz × 4, 16GB RAM). Directly inserting *nodata* values to the whole DEM takes about 25 hours and interpolating new values takes an additional 8 hours. The duration of the tile merging varies, depending on the tools used and the read/write speed of the hard drive used.

3.4 Validation methodology

Some parts of the modern features fell outside the interpolated areas of the model, but it was unfortunately not possible to assess with any statistical precision the proportion of artificial elements removed or to reliably distinguish how many of them continued to produce distortions. Therefore, our evaluation was focused more on comparing the relevant properties of the input and output DEMs, while assessing changes and their possible influence on future archaeological analyses.

The main objective was to create a DEM with better analytical potential in terms of visibility, drainage networks, and terrain morphology. To reduce computational complexity with a view to testing these model properties, we used downscaled versions of the DEMs at a cell size of 8 x 8 m. The following models were created for both DEMs (original and interpolated): (1) cumulative visibility model; (2) stream network model; (3) land surface curvature (LSC) model. All the models were then used to assess the qualities of the filtered DEM compared to the input DEM. Validation-related data are available through the Zenodo repository (https://doi.org/10.5281/zenodo.6368001).

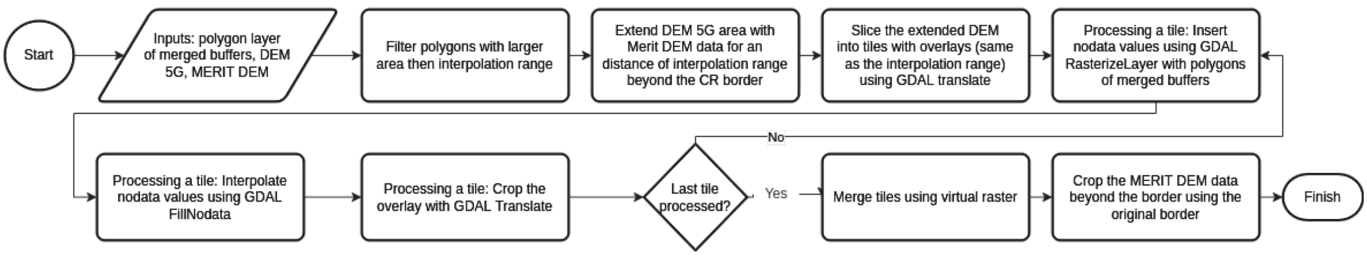

Fig. 4 *The interpolation process used to remove the more recent DEM features*

3.4.1 Testing the visibility properties

Visibility is a parameter with wide-ranging implications for the perception of historic human activity (Gibson 1986; Llobera 2007). Regardless of the specific application or theory, the principle of visibility analysis is to identify an uninterrupted visual link between two points in a terrain or DEM. However, the modern landscape is filled with objects that significantly alter visual properties and observability. When transcribed to LiDAR-derived DEMs, these features create potentially significant biases, which can compromise the analysis and study of pre-industrial landscapes. To evaluate the effect of these features on the visual properties of the original and filtered DEMs, two cumulative visibility models were calculated for regularly spaced points on a 10 x 10 km grid with a visibility radius of 5 km and an observer height of 2 m. In total, 574 viewsheds (without overlaps) were combined within a single model.

3.4.2 Testing drainage properties

As with visibility, runoff conditions are strongly influenced by the specific shape of the micro-relief. In particular, linear infrastructure features have a significant effect on the reconstruction of drainages, as they often act as channels that alter the natural gradient. To test the effect of filtration on the drainage modeling, a stream network for the original and filtered DEMs was calculated using standard ESRI ArcGIS tools and the TauDEM toolbox. Each input model was extended to the entire catchment using EU-DEM (https://www.eea.europa .eu/data-and-maps/data/copernicus-land-monitoring-service-eu-dem) as a data source for areas outside the Czech Republic (in particular, Lower Austria). Drainage-free zones were identified and filled in automatically. Drainages with a Strahler order greater than 4 were defined as potential watercourses (despite the simplifications, which had no bearing on our analysis).

3.4.3 Testing curvature properties

The degree of curvature is considered the basis for morphometric descriptions and analyses of the relief (Hengl and Reuter, 2009; Krebs et al. 2015; Minár et al., 2020). Landforms identified by curvature, especially terrain edges and ridges, are often the sites of building activity carried out by pre-modern societies, e.g., burial mounds (Kuna 2006) or feudal seats (Novák 2019). LiDAR-derived DEMs allow researchers to identify such shapes and to examine relationships between settlements and landforms in much greater detail. Accordingly, definitions of such landforms must be based on a model that is at least tentatively stripped of elements of the industrial landscape. These features are often characterized by linear or stepped cuts in the terrain, which tend to appear as unnatural structures, and which in turn affect the analytical properties of the DEM.

To evaluate the qualitative differences between the original and interpolated DEM, profile and plan LSC models were calculated using the *Curvature* function in ESRI ArcGIS. From these models, cells with a negative value exceeding the standard deviation were extracted in the case of profile curvatures (terrain edge peaks), while cells with a positive value exceeding the standard deviation were extracted in the case of plan curvatures (ridge peaks). In principle, the average of the values was close to zero for both models, as each concave feature has its own convex counterpart. The results were combined as a single model, indicating the location of significant relief features and then compared for both DEMs.

4 RESULTS

The DEM output was first validated with the same profile method used to determine the buffer sizes (Fig. 3). The total interpolated area of the DEM was 15% of the original model, i.e., 8,729 km^2. Changes in the DEM elevation within the interpolated areas were typically ± 5 m, with a minimum value of 64.5 m and a maximum value of 101.4 m (Fig. 5).

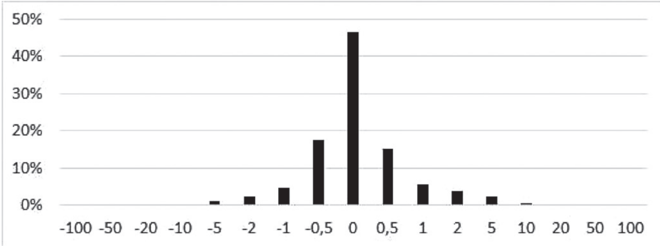

Fig. 5 *The difference in the distribution of the altitude values for the original and interpolated DEMs. The negative values indicate an increase in the terrain, while the positive values indicate a decrease. The measurements are in meters.*

4.1 Changes in the visibility properties

Based on the computations performed, it can be stated that even though the observer in the random sample was often placed in a highly unsuitable position and the overall visibility of the surroundings was therefore minimal (on average 4% of the defined radius), there was an improvement in overall visibility for the filtered DEM in 94% of the cases observed, with an average improvement of 11% (confidence interval +-5% for $p < 0.01$; standard deviation 51%; median 5%; Fig. 6). Statistically significant differences in observations at the individual sample points were validated by the paired two-sample t-test, which confirmed changes in the values measured at a significance level of $p < 0.01$ ($p = 7.36e-34$; $t = -12.96$; $t_{crit} = 2.58$).[1] The overall impact of the filtration on the visual properties of the resulting model was so great that even after allowing for the fact that the samples were independent and validated by the two-sample t-test, which assumes unequal variances (despite these values representing the same individuals), the difference between the two samples reached a significance level of $p < 0.1$ ($p = 0.099989$; $t = -1.64624$; $t_{crit} = 1.64619$).[2]

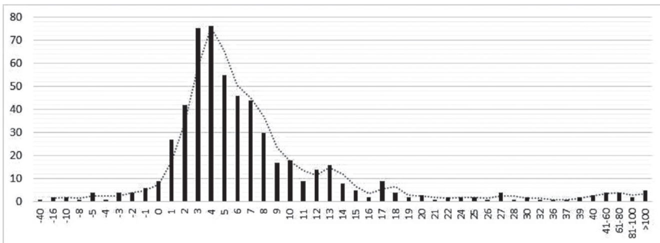

Fig. 6 *The difference in the distribution of the visibility values in the original and interpolated DEMs (based on a random sample of 574 viewsheds). There is a strong prevalence for positive values (improvement in visibility).*

These findings undoubtedly demonstrate that the use of the unfiltered DEM featuring modern formations had a significant impact on the results. In order to create the total visibility models mentioned in the introduction, our adjustment was a crucial step without which the models would have generated significantly different values compared to the previous state. Conditions around the early medieval hillfort

[1] Null hypothesis: *the number of cells visible from the selected point in the original model did not significantly differ from the number of cells visible from the same point in the filtered model*.

[2] Null hypothesis: *the set of visibility values derived from the original model was significantly different compared to the set of values acquired for the filtered DEM.*

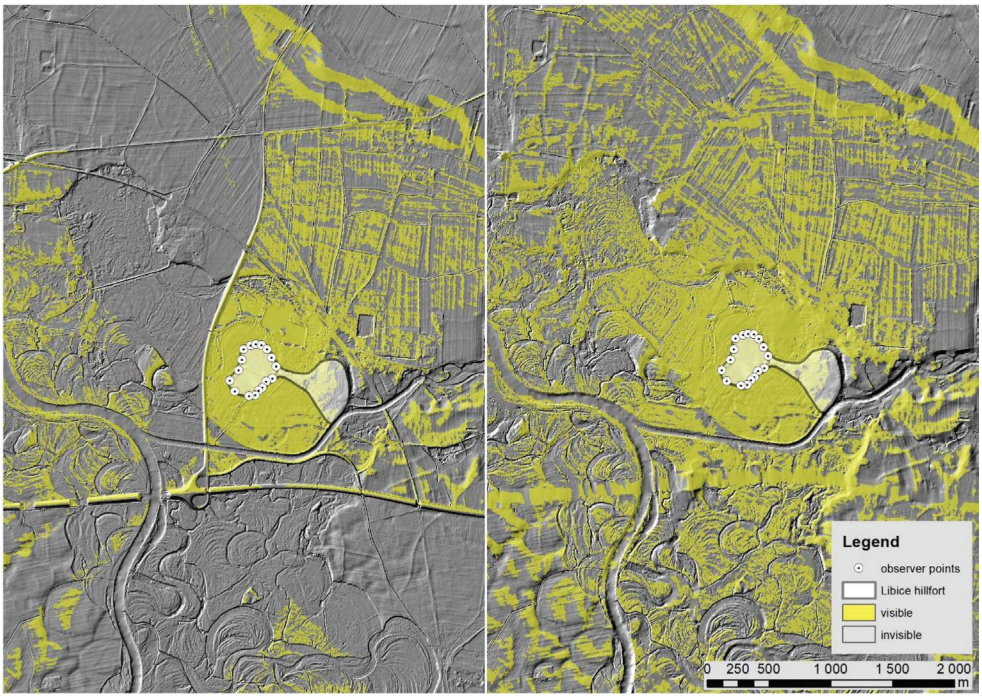

Fig. 7 *Viewshed comparison of the surroundings of the Libice nad Cidlinou hillfort before (left) and after DEM filtering (right). The visible sites are shaded in yellow (observer height 2 m; observation points located on the edge of the acropolis). In the flat terrain, the removal of road bodies had a significant impact, e.g., changing the visibility conditions considerably (data provided by ČÚZK).*

in Libice nad Cidlinou are illustrative in this respect, where a fundamental difference in the visibility of the surroundings from the hillfort acropolis before and after the filtering is clearly visible (Fig. 7).

4.2 Changes in the drainage properties

The results show that of the total 22,194,177 cells identified as part of the original drainage network, only half (52%) retained their location using the filtered DEM, while the total percentage of the interpolated terrain did not exceed 15% of the model area. Using a paired two-sample t-test on a sample area of one randomly selected sheet of the 1:50,000 Base Map (No. 22-11; 459 km^2; 205,911 drainage cells in the original model), at a significance level of $p < 0.01$ ($p = 0$; $t = 462$; $t_{crit} = 2.6$), we can completely reject the null hypothesis that the original drainage network has not changed.[3] These figures suggest large differences between the drainage patterns in the pre-industrial and modern landscapes, which are reflected by the substan-

[3] Null hypothesis: *If the cell in the original model is part of the drainage, it is also present in the filtered model and in the same Strahler order.*

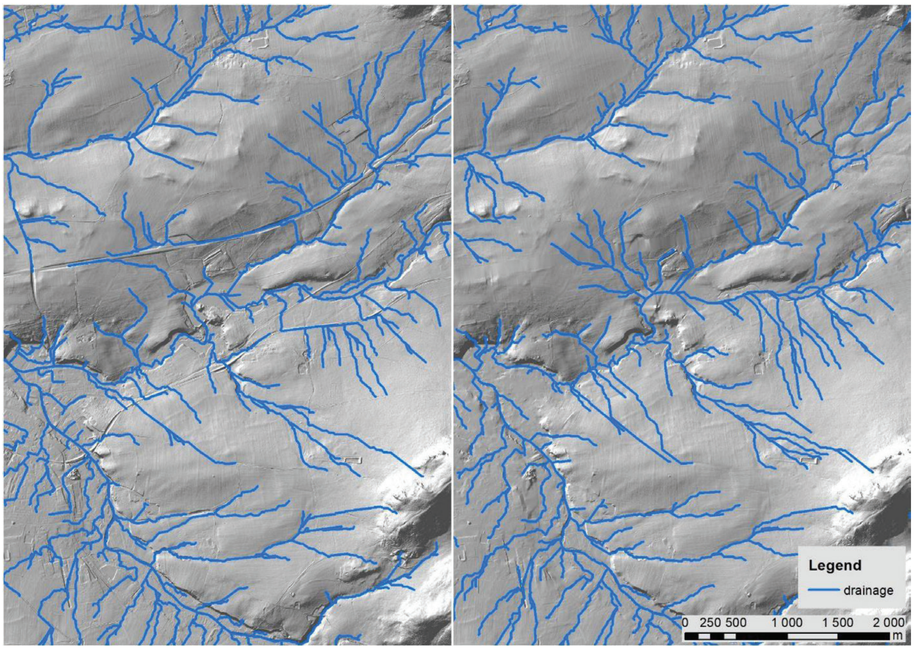

Fig. 8 *Comparison of the drainage network before (left) and after the DEM filtering (right). The drainage conditions more closely approximate the characteristics of the natural landscape, both in the open terrain and in the built-up areas (data provided by ČÚZK).*

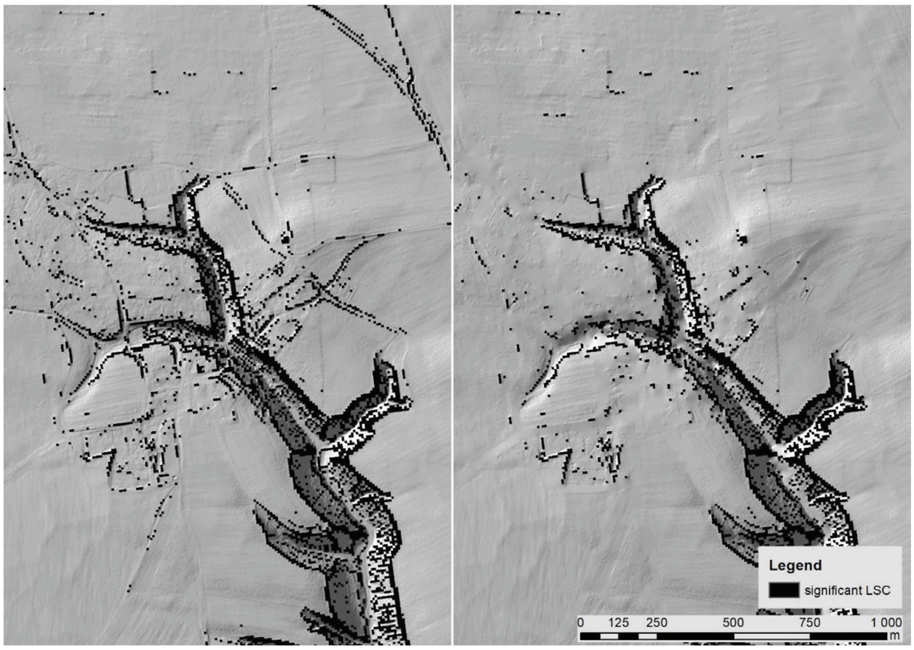

Fig. 9 *A comparison of LSC before (left) and after DEM filtering (right). Cells with a significant profile or plan curvature are highlighted in black. Only some of the more prominent artificial edges remain visible after cleaning, but most of the curvature follows the natural course of the terrain, and the noise fraction has been reduced (data provided by ČÚZK).*

tially different characteristics of the two models. An optical comparison of the models below shows that the filtering rectified the major shortcomings of the original DEM (Fig. 8).

4.3 Changes in the curvature properties

Based on our evaluation, the interpolated DEM contained 9% fewer significant edges and ridges than the original unrefined model. Using the paired two-sample t-test validation for the sample area once again (see 4.2; 330,590 cells with significant LSC in the original model), the difference between the models was also confirmed at a significance level of $p < 0.01$ ($p = 0$; $t = 422$; $t_{crit} = 1.96$).[4] Moreover, if we take into account that the clipping buffers contained 27% of the significant LSCs but occupied only 15% of the total DEM area, it is clear that a considerable part of the significant LSCs was due to modern man-made features captured by the laser scanner. It was therefore desirable that in the interpolated areas, the reduction of significant LSCs would reach 75% of the original occurrences. An optical comparison of the two results indicates that the interpolation removed substantial sections of the unnatural breaks, while preserving the basic characteristics and form of the original terrain (Fig. 9). Although many man-made features of the model were not removed, this type of interpolation substantially increases the opportunities for geomorphometric analysis of the DEM.

5 DISCUSSION

Our results convincingly demonstrate that DEM filtering, at least to the extent presented here, is a valuable technique for DMR 5G (or any similar LiDAR-derived DEM) and general archaeological geomorphometric applications. For the purposes of the surveying and documentation of archaeological sites, the application of the clipping mask can assist in the processing of data for automated classifications and also in removing disturbances before manual (visual) identification of burial sites (cf. Werbrouck et al., 2011). Based on a visual assessment of the outputs, the smooth interpolated segments of the DEM at first seem unnatural. To remedy this effect, a certain amount of noise can be applied to the interpolated values to make the shaded DEM appear more natural. On balance, however, retaining the smooth surface is recommended for future processing steps such as viewshed or stream network analysis.

As expected, and as can be seen from the resulting model, some of the modern elements in the interpolated DEM remain. In principle, these deficiencies are not caused by the chosen method, but by the quality of the input data (clipping mask). With a more complete record of modern interventions, such as marginal roads, sections of channelised streams, and other similar features, the credibility of the output model and the impact of the filtration would improve further. Interpolation is also problematic when used in highly urbanized environments, where achieving a plausible reconstruction of the original surface requires considerably more complex approaches (cf. Boháčová and Herichová, 2004; Bini et al. 2016; Herichová, 2019), which are extremely difficult to implement across such a general level.

The most extensive interventions, such as open-pit mines and water reservoirs, posed a persistent problem. In these instances, a reconstruction of the relief would likely require the use of historical mapping data containing elevation information. Therefore, in regions affected by large-scale mining, our approach would benefit from additional measures. There were local zones in the model where reconstruction was essentially impossible, resulting in the preservation of the original data from the output DEM. Some residues also remained from larger infrastructure constructions where the ground disturbance exceeded the normal extent evaluated in the initial analysis, as reflected by the size of the clipping buffers. These shortcomings may be overcome by optimizing the generation of clipping zones, so that the complexity (especially the local curvature) of the surrounding terrain is properly defined, e.g., by using the principle of mean curvature watersheds (Romstad and Etzelmüller, 2012).

Based on the properties of the input and output DEMs, our procedure, despite its limitations, significantly improves the applicability of the model for archaeological landscape research. Although it is not possible to precisely determine how closely the modifications reflect

[4] Null hypothesis: *if the cell in the original model has a significant LSC, the same cell will also have a significant LSC in the filtered model*.

the original terrain shape, and, despite the filtered DEM containing potential distortions (some caused by the filtering and interpolation itself), our results overwhelmingly point to a significant enhancement of the original model, thus increasing the potential for further analysis. At the same time, it should be noted that the objective of the modifications was not to completely reconstruct the pre-industrial landscape *per se*, but rather to eliminate the major deficiencies of DMR 5G when performing further calculations (see section 1). Creating a completely accurate reconstruction would require a much more complex approach, i.e., one that considers the many processes that led to these artificial changes in the landscape. That would also require the addition of historical data for large areas of the landscape that have been mined or otherwise deformed, which, in principle, cannot be achieved by interpolation alone.

6 CONCLUSIONS

LiDAR-derived DEMs have undoubtedly advanced technical capabilities in the field of archaeology, but their integration within landscape-archaeological analysis remains limited. One of the reasons for this may be an issue discussed in this paper, i.e., the presence of modern terrain interventions, which make the practical use of accurate elevation models for spatial analysis more difficult. Our study shows that the application of practical corrective methods to even large-scale DEMs, without high input costs (time or financial), produces a significant qualitative shift in the modeling of landscape properties.

Focusing on the territory of Bohemia, we extracted areas identified by vector topographic maps to clean the DEM of modern features. Due to the extent of the processed area, it was not possible to use procedures involving manual editing or cleaning. Although straightforward in principle, our approach is novel due to its practical applicability on the large scale. As our results show, this relatively simple method of DEM correction can fundamentally affect the properties of the model and its usefulness for subsequent analysis. Using filtering and interpolation, we managed to improve the model properties with respect to the visibility, drainage patterns, and geomorphological properties represented by the curvature.

Future improvements to the model should be aimed at bridging problems connected with removing certain typically modern large-scale landscape features (surface mining, large water bodies, urbanization zones, etc.). To that end, it will be necessary to create a yet-to-be-established databank of digitized historical elevation data based on legacy topographic maps to be used as a basis for the interpolation of accurate pre-industrial DEMs. We also recommend that the DEM raster grid be supplemented by a secondary layer with an estimate of the expected vertical resolution based on the filtering and interpolation methods, source data, and filtered features used. Considering the Czech context, enabling free access to the DMR 5G in the form of a point cloud would be another important step. This would allow researchers to select specific data points and subsequently triangulate missing data instead of making modifications to the raster grid. Notwithstanding these possible future measures, we consider that our filtered DMR 5G model, even in its present form, is the most suitable and best available centrally provided framework for archaeological use that can facilitate standardized derivations of total visibility, relief classification, and drainage networks on a national scale in the Czech Republic.

Acknowledgements

The authors would like to thank Alexandra Bucha Rášová, Martin Kuna and Peter Demján for their help, particularly their contributions to the theoretical discussions that informed the concept for this paper.

Funding: This work was supported by the European Union through the OP VVV programme administered by MEYS, within the project Archaeological Information System of the Czech Republic – Second Generation [Grant No. CZ.02.1.01/0.0/0.0/16_013/0001439] and by the Grant Agency of the Ministry of Education, Science, Research and Sport of the Slovak Republic and the Slovak Academy of Sciences, VEGA [Grant Nos. 1/0300/19 and 1/0468/20].

REFERENCES

Bini, M. – Pappalardo, M. – Rossi, V. – Noti, V. – Amorosi, A. – Sarti, G. (2018) *Deciphering the effects of human activity on urban areas through morphostratigraphic analysis: The case of Pisa, Northwest Italy.* Geoarchaeology, Vol. 33, pp. 43–51.

Boháčová, I. – Herichová, I. (2004) *Georeliéf jako zdroj poznání historického vývoje lokality.* Forum urbes medii aevi, Vol. 1, pp. 10-17.

Brázdil, K. – Bělka, L. – Dušánek, P. – Fiala, R. – Gamrát, J. – Kafka, O. – Peichl, J. – Šíma, **J. (2016)** *Technická zpráva k Digitálnímu modelu reliéfu 5. generace: DMR 5G* Available at: https://geoportal.cuzk.cz/Dokumenty/TECHNICKA_ZPRAVA_DMR_5G .pdf, (accessed at 09/03/2022).

Brughmans, T. – Van Garderen, M. – Gillings, M. (2018) *Introducing visual neighbourhood configurations for total viewsheds.* Journal of Archaeological Science, Vol. 96, pp. 14–25.

Chase, A.S.Z. – Chase, D.Z. – Chase, A.F. (2017) *LiDAR for Archaeological Research and the Study of Historical Landscapes.* In: N. Masini, F. Soldovieri, eds. *Sensing the Past: From artifact to historical site.* Geotechnologies and the Environment, Vol. 16, Cham: Springer.

Crutchley, S. – Crow, P. (2009) *The light fantastic: using airborne laser scanning in archaeological survey.* Swindon: English Heritage.

David, B. – Thomas, J. (eds.) (2008) *Handbook of Landscape Archaeology*. London and NY: Routledge.

De Reu, J. – Bourgeois, J. – Bats, M. – Zwertvaegher, A. – Gelorini, V. – De Smedt, P. – Chu, W. – Antrop, M. – De Maeyer, P. – Finke, P. – Van Meirvenne, M. – Verniers, J. – Crombé, P. (2013) *Application of the topographic position index to heterogeneous landscapes.* Geomorphology, Vol. 186, pp. 39–49.

De Smedt, P. – Van Meirvenne, M. – Davies, N.S. – Bats, M. – Saey, T. – De Reu, J. – Meerschman, E. – Gelorini, V. – Zwertvaegher, A. – Antrop, M. – Bourgeois, J. – De Maeyer, P. – Finke, P.A. – Verniers, J. – Crombé, P. (2013) *A multidisciplinary approach to reconstructing Late Glacial and Early Holocene landscapes.* Journal of Archaeological Science, Vol. 40(2), pp. 1260–1267.

Garstki, K. (2020) *Digital Innovations in European Archaeology*. Elements in the Archaeology of Europe. Cambridge: Cambridge University Press.

Gibson, J.J. (1986) *The Ecological Approach to Visual Perception*. NJ: Psychology Press.

Gillings, M. (2017) *Mapping liminality: Critical frameworks for the GIS-based modelling of visibility.* Journal of Archaeological Science, Vol. 84, pp. 121–128.

Gojda, M. – John, J. (eds.) (2013) *Archeologie a letecké laserové skenování krajiny / Archaeology and airborne laser scanning of the landscape*. Plzeň: Katedra archeologie FF ZČU.

Habicht, H.L. – Rosentau, A. – Jõeleht, A. – Heinsalu, A. – Kriiska, A. – Kohv, M. – Hang, T. – Aunap, R. (2017) *GIS-based multiproxy coastline reconstruction of the eastern Gulf of Riga, Baltic Sea, during the Stone Age.* Boreas, Vol. 46, pp. 83–99.

Hengl, T. – Reuter – H.I. (eds.) (2009) *Geomorphometry: Concepts, Software, Applications*. Amsterdam: Elsevier.

Herichová, I. (2019) *Vrch hradní. Vývoj georeliéfu Pražského hradu v raném středověku.* Prague: Archeologický ústav AV ČR.

Hobič, J. (2020) *List of freely accessible LiDAR data and digital terrain models [online].* Archaeology of Slovenia. Available at: https://arheologijaslovenija.blogspot.com/p/ blog-page_81.html (accessed at 06/08/2021)

Höfler, V. – Wessollek, C. – Karrasch, P. (2015) *Modelling prehistoric terrain Models using LiDAR-data: a geomorphological approach.* I Proc. of SPIE, 9644, Earth Resources and Environmental Remote Sensing/GIS Applications VI, 96440B.

Krebs, P. – Stocker, M. – Pezzatti, G.B. – Conedera, M. (2015) *An alternative approach to transverse and profile terrain curvature.* International Journal of Geographical Information Science, Vol. 29(4), pp. 643–666.

Kuna, M. (2004) *Nedestruktivní archeologie: Teorie, metody a cíle*. Prague: Academia.

Kuna, M. (2006) *Burial mounds in the landscape.* In: L. Šmejda, ed. Archaeology of Burial Mounds. Plzeň: Dryada, pp. 83–97.

Kuna, M. – Danielisová, A. (2009) *Geomorfometrie a analýza reliéfu v archeologii.* Živá archeologie, Vol. 10, pp. 56–60.

Kuna, M. – Novák, D. – Bucha Rašová, A. – Bucha, B. – Machová, B. – Havlice, J. – John, J. – Chvojka, O. (2022) *Total viewshed in archaeology: problem solved, issues remain.* Journal of Archaeological Science, Vol. 142, pp. 105596.

Llobera, M. (2003) *Extending GIS-based visual analysis: the concept of visualscapes.* International Journal of Geographical Information Science, Vol. 17, pp. 25–48.

Llobera, M. (2007) *Reconstructing visual landscapes.* World Archaeology, Vol. 39, pp. 51–69.

Minár, J. – Evans, I.S. – Jenčo, M. (2020) *A comprehensive system of definitions of land surface (topographic) curvatures, with implications for their application in geoscience modelling and prediction.* Earth-Science Reviews, Vol. 211, pp. 103414.

Novák, D. (2018) *Wykorzystanie ALS do zautomatyzowanej analizy krajobrazu.* In: M. Gojda, Z. Kobyliński, eds. Lotnicze skanowanie laserowe jako narzędzie archeologii. Archaeologica Hereditas, 11. Warszawa: Instytut Archeologii Uniwersytetu Kardynała Stefana Wyszyńskiego w Warszawie, pp. 69–84 [in Polish].

Novák, D. (2019) *Funkční klasifikace a vývoj vrchnostenských sídel ve středověkých a raně novověkých* Čechách*.* Památky archeologické, Vol. 110, pp. 307–382.

Posluschny, A.G. (ed.) (2015) *Sensing the Past: Contributions from the ArcLand Conference on Remote Sensing for Archaeology.* Bonn: Habelt-Verlag.

Rášová, A. (2017) *Substanciálna analýza viditeľnosti v prostredí GIS*. Unpublished thesis (PhD), Slovak University of Technology in Bratislava [in Slovak].

Romstad, B. – Etzelmüller, B. (2012) *Mean-curvature watersheds: A simple method for segmentation of a digital elevation model into terrain units.* Geomorphology, Vol. 139-140, pp. 293–302.

Schmidt, J. – Werther, L. – Zielhofer C. (2018) *Shaping pre-modern digital terrain models: The former topography at Charlemagne's canal construction site.* PLoS ONE, Vol. 13(7), pp. e0200167.

Tarboton, D.G. – Schreuders, K.A.T. – Watson, D.W. – Baker, M.E. (2009) *Generalized terrain-based flow analysis of digital elevation models.* In: R.S. Anderssen, R.D. Braddock, and L.T.H. Newham, eds. *1*8th World IMACS Congress and MODSIM09 International Congress on Modelling and Simulation*.* Christchurch: Modelling and Simulation Society of Australia and New Zealand, pp. 2000–2006.

Werbrouck, I. – Antrop, M. – Van Eetvelde, V. – Stal, C. – De Maeyer, Ph. – Bats, M. – Bourgeois, J. – Court-Picon, M. – Crombe, Ph. – De Reu, J. – De Smedt, Ph. – Finke, P.A. – Van Meirvenne, M. – Verniers, J. – Zwertvaegher, A. (2011) *Digital Elevation Model generation for historical landscape analysis based on LiDAR data, a case study in Flanders (Belgium).* Expert Systems with Applications, Vol. 38(7), pp. 8178–8185.

Zwertvaegher, A. – Finke, P. – De Reu, J. – Vandenbohede, A. – Lebbe, L. – Bats, M. – De Clercq, W. – De Smedt, P. – Gelorini, V. – Sergant, J. – Antrop, M. – Bourgeois, J. – De Maeyer, P. – Van Meirvenne, M. – Verniers, J. – Crombé, P. (2013) Reconstructing Phreatic Palaeogroundwater Levels in a Geoarchaeological Context: A Case Study in Flanders, Belgium. *Geoarchaeology*, 28, 170–189.

Zwertvaegher, A. – Werbrouck, I. – Finke, P.A. – De Reu, J. – Crombé, P. – Bats, M. – Antrop, M. – Bourgeois, J. – Court-Picon, M. – De Maeyer, P. – De Smedt, P. – Sergant, J. – Van Meirvenne, M. – Verniers, J. (2010) *On the use of integrated process models to reconstruct prehistoric occupation, with examples from Sandy Flanders, Belgium.* Geoarchaeology, Vol. 25, pp. 784–814.

Slovak Journal of Civil Engineering

Vol. 30, 2022, No. 4, 11 – 16
DOI: 10.2478/sjce-2022-0023

COMPARATIVE STUDY OF LIGHTWEIGHT CONCRETES BASED ON HEMP AND FLAX STRAW

Maryna BABENKO[1*], Adriana ESTOKOVA[2], Stanislav UNČIK[1], Mykola SAVYTSKYI[3]

Abstract

The article presents the results of a study involving the properties of flax and hemp-based lightweight concretes as well as the initial characteristics of different straw-based materials. A comparison of straw-based lightweight concretes with and without ordinary Portland cement (OPC) showed that hemp concrete has a 5.6 % higher strength at a 10% deformation, and at the same time, has a 13% greater thermal conductivity coefficient than flax concrete. The physical-chemical study based on a thermal analysis in an air environment has shown that the overall picture of thermal degradation for flax and hemp concretes is similar. Nevertheless, additional peaks of mass loss have been defined for flax concrete. The demonstrated exothermal process is a positive aspect, considering the life cycle of the material and the recycling stage. The paper proposes reference points for the development of new building materials based on straw.

Address

[1] Department of Materials Engineering and Physics, Civil Engineering Faculty, Slovak University of Technology in Bratislava, Radlinského 2766/11, 810 05 Bratislava Slovak Republic,

[2] Department of Material Engineering/Institute of Environmental Engineering, Faculty of Civil Engineering, Technical University of Kosice, Slovakia,

[3] Department of Reinforced-Concrete and Stone Constructions, State Higher Education Establishment, Pridneprovska State Academy of Civil Engineering and Architecture, Ukraine

* ***Corresponding author:*** maryna.babenko@stuba.sk

Key words

- Flax,
- Hemp,
- Straw,
- Lightweight concrete,
- Energy efficiency,
- Sustainable development.

1 INTRODUCTION

One of the most important issues today in the construction sector is saving energy and ensuring the high-quality thermal insulation of walls for buildings. Construction is a very energy-intensive process, and the continuing increase in energy prices significantly increases the costs of the erection of new buildings and the exploitation of existing ones. This issue was discussed extensively during the Climate Conference in Paris (COP21). (Gurwitt, S. et al., 2017) It underscored that buildings and communal services are one of the most energy-intensive sectors of the world economy. Thirty (30) to forty (40) percent of total energy consumption is spent in the operation of building constructions. (Paiva, R.d.L.M et al., 2021)

One of the ways to save fuel on and energy resources is to reduce heat losses through enclosing structures but also by taking into account the whole life cycle of a structure and its insulation materials. Toughening of heat engineering requirements for enclosing structures requires using highly effective heat-insulating materials. To date, the existing housing stock of Ukraine requires the renovation and construction of new energy-efficient, comfortable and, at the same time, affordable housing.

Well-known complex materials are based on straw, e.g., adobe, fibrolite, wood concrete, bitumen, reed concrete, flax and peat heat-insulating slabs, etc. The building techniques that use these materials are mostly seen in vernacular architecture and rural local constructions. Approximately 115 million tonnes of agricultural plant waste are generated annually in Ukraine (Pryshliak, N., & Tokarchuk, D., 2020), which creates an incentive to implement agricultural plant waste as a source of ecological building material. To encourage large-scale use of agriculture waste in the building sector, raw materials and composites made from them should be studied to develop industrial solutions to be applied during the construction or renovation of buildings.

Pressed heat-insulating plates based on chopped rye straw (particle length: 20-40 mm), flax straw (particle length: up to 5 mm) and sodium water glass have been investigated in (Bakatovich A.A. et al., 2011). The results showed that the average density of the samples was 212 - 230 kg / m^3; the coefficient of thermal conductivity was 0.046-0.051 W / (m·K); and the compressive strength reached 0.55-0.83 MPa. At the Faculty of Civil Engineering of the Technical University of Kosice (Slovakia), research is being conducted on the use of hemp straw for the production of composite materials made of fibrous aggregates, e.g., hemp straw and an alternative calcium free binder such as MgO, i.e., a binder consisting of calcined natural MgO, siliceous river sand, and sodium bicarbonate. In (Stevulova N. et al., 2012), the effect of three different fractions of filler (with mean particle lengths of 33.7; 27.7; and 7.3 mm) on the selected physical and mechanical properties of 28 - day hardened bio-composites were investigated. The most favorable values of the compressive strength (5.2 MPa), water absorption (11.88 %), and the thermal conductivity coefficient (0.11 W/(m·K) of hemp hurd composites were recorded for a composite based on a fraction with the smallest length of the hemp aggregates.

However, a complex approach considering the correspondence of the materials to sustainability has not been conducted. Hence, the main purpose of this study was formulated to be:

- a **theoretical study** of the composition and structure of materials of an organic origin, e.g., wheat, reed hemp and flax straw, as bases for the formation of a composition;
- the **mechanical properties** of the materials received, e.g., density under a 10% deformation, MPa
- **physical properties** of the materials received, e.g., moisture, %; coefficient of thermal conductivity, W/(m K)
- **physical-chemical properties** of the materials received and thermal analysis in an air environment, e.g., mass change, thermal stability.

The proposed research is dedicated to evaluating the overall properties of straw insulation materials, taking into account their correspondence to the main demands of sustainable development and the optimization of building life cycle stages.

2 MATERIALS AND METHODS

The research presented was realized according to an approach consisting of the theoretical and experimental study of agricultural waste plant materials. The general schema of the research is shown in Fig. 1.

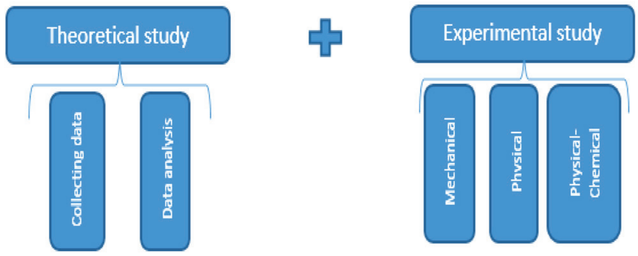

Fig. 1 *General schema of the research*

2.1 Theoretical study

Hemp (*Cannabis sativa cultivars*) is a genetically diverse and variable crop that produces raw products in three distinct categories: seed/oil, fiber, and metabolites. (Craig Schluttenhofer et al., 2017) Hemp can be harvested in as little as 60 days. Hemp concrete is a “carbon-negative” or “better-than-zero-carbon” substance because the hemp plant absorbs more carbon from the environment than it releases during its preparation and application on site (Salim Barbhuiya and Bibhuti Bhusan Das, 2022). Fiber hemp can be considered as an alternative to wood as a raw material for pulp and paper production. Additionally, hemp fiber is durable and can be used to make clothes, canvas, fishnets, construction materials, and reinforcements when preparing composite parts such in, e.g., thermal and acoustic insulation (Meijer, W. J. M. et al.,1995; Vonapartis E. et al., 2015; Rehman, M. et al., 2021).

Flax (*Linum usitatissimum*), a herbaceous annual plant (referred to as “fiber” or “seed” flax) (Manian A.P. et al., 2021, Nikolsky, S.N. et al., 2022), is grown for its oil or stem fiber. Compared to other typical agricultural products, flax straw takes substantially longer to naturally degrade (Anthony W.S., 2002). The use of flax straw thus becomes one of the main issues facing modern agriculture. The positive environmental characteristics and effective performance of flax fibers has been significantly developed for various applications, including construction, in recent years (Zhu, J. et al., 2013)

This theoretical study of the composition and structure of materials of an organic origin, i.e., hemp and flax straw, has been realized on the basis of a literature review by collecting data from different sources and comparing them. As is well-known, the quality of a multicomponent material structure is determined by the characteristics of its constituent components and the physicochemical processes between them. Therefore, to understand the process of the structural formation of a composite material based on raw plant materials, theoretical information on the chemical composition of the plant fibers and their structure was studied.

Cellulose, lignin, hemicellulose, pectin and extractives are included in the fiber of a plant tissue. Cellulose and lignin are persistent substances that do not adversely affect the hardening of clinker cements. The pectin and hemicellulose part of plant material in an alkaline medium are able to pass into water-soluble sugars (sucrose, fructose, glucose), which, along with extractive substances, are “cement poisons”. These substances form the finest shells on the surface of cement particles; they isolate them from water, which slows down the process of the hydration of cement. Water-soluble substances are partially washed out with hot water or blocked with solutions of

Tab. 1 *Composition of the composite mixture*

Concrete	Straw, mass fractions	Water Glass, mass fractions	Portland Cement, mass fractions	Water, mass fractions
hemp straw concrete (HSC)	1	1	1	4
flax straw concrete (FSC)	1	1.5	-	-

Tab. 2 *The parameters of the thermal analysis of the straw-based lightweight concretes*

Lightweight concretes	Initial mass, mg	Heating rate, K/min	Temperature interval, °C	Atmosphere
HSC	12.73	10	26-900	air
FSC	17.87	10	27-900	air

a “mineralizer”. The most famous “mineralizers” are calcium chloride and water glass.

The mentioned particularities and other known properties of straw material have been taken into consideration for further research and development of the material.

2.2 Experimental study

The hemp and flax straw used in the experiments were stored for three months under the same temperature and humidity conditions (T = 18-25°C, humidity 50%). The straw was ground before testing it. Dry hemp straw sized 20-35 mm and flax straw sized 15 – 25 mm were used in the experiment. The straw was sifted through a sieve with a mesh size of 15 mm to prevent inclusions of straw dust. Sodium silicate (Na2O(SiO2)) in the form of a liquid solution with a density of 1.30 g/cm^3 was used as a binder for a lightweight concrete based on straw. For the composition of the lightweight hemp concrete, Type I, B 32.5 (M400) ordinary Portland cement was used.

The light concrete mixtures studied were produced according to the following procedure. The dry components were mixed for 2 minutes; water glass was then added; and the composition obtained was stirred for 2-3 minutes until it was a homogeneous mass. Before adding the water glass, the concrete was diluted with the necessary amount of water. The contents of the concrete samples used are in Table 1 (Babenko M. et al., 2018).

The lightweight concrete samples were sized 70 x 70 x 70 mm (Fig. 2), and were made by the manual compaction method in molds. The mixture in the molds was fed layer by layer (3 layers); each layer was sealed after it was fed into the molds. In the manufacture and holding of the samples, the air temperature was 18-20°C, and the humidity was 45-50%. After stripping, the concrete compositions were dried at a temperature of 60-100° C to a constant weight. Three samples of each composition were produced for the tests.

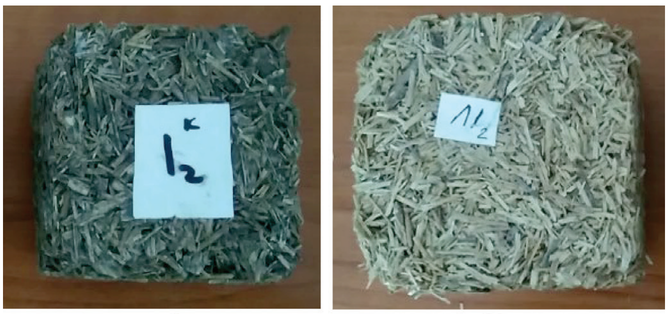

Fig. 2 *The lightweight concrete samples of a) HSC- based on hemp straw ($1^{к}_{2}$); b) FSC – based on flax straw ($Л1_2$)*

The compressive strength, bulk density, thermal conductivity, and thermal stability were investigated according to the mechanical and physical properties of the composites.

The compressive strength of the concrete in MPa was determined after drying the samples according to the normative document (DSTU, 2009) The samples were destroyed on a 0.4 ton press with a loading speed of 4 kg per second. The compressive strength was determined by the ratio of the breaking load to the cross-sectional area of the sample.

The moisture content of the freshly formed samples relative to those dried to a constant weight was determined according to (GOST, 1979) and was calculated by the formula:

$$W = \frac{m_1 - m_2}{m_2} \times 100,$$

where is the mass of the sample before drying; is the mass of the sample after drying. The results of the calculations are rounded up to 0.1%.

The determination of the **thermal conductivity** of the lightweight concrete was performed using the BI-TO21 (BI-TO, 2000). The device is designed in accordance with (DSTU, 1996) and uses a non-destructive method for the accelerated determination of the thermal conductivity.

The thermal analysis in an air environment was conducted to study the mass change, thermal stability, and energy balance. The study was realized on a STA 449 F3 Jupiter® simultaneous thermal analyzer. The tests were performed on the selected samples of lightweight concrete based on the hemp and flax using the TG/DSC mode. The samples were heated in Al_2O_3 crucibles. The parameters of the measurements are presented in Table 2 (Babenko M. et al., 2018).

3 RESULTS AND DISCUSSION

The initial results of the combined theoretical study and the use of the elements of the experimental study of raw basic materials for ecologically lightweight concrete are presented in

Tab. 3 *Properties of basic raw materials*

Material source of straw	Granulometric size, mm	Average apparent density, kg /m³	Porosity, %	Thermal conductivity coefficient W/(m·K) at volumetric humidity,%		
				0	5	10
Hemp	20-35	70-120	88	0.0465	0.0628	0.077
Wheat	20-40	38-45	89	0.058	0.0767	0.095
Flax	2-15	120-135	85	0.0481	0.0632	0.085
Reed	15-42	150-200	84	0.07	0.089	0.105
Wood	8-15	220-300	82	0.098	0.107	0.145

Tab. 4 *Results of the mechanical and physical studies*

Name of lightweight concrete sample	Average density of the material, kg/m³	Thermal conductivity coefficient W/(m·K)	Strength at 10% deformation, MPa	Moisture, %
HSC	300	0.09	0.38	38
FSC	250	0.078	0.36	41

Table 3. The study conducted has defined the basic properties for straws of different origins. It is necessary to mention than the primary similarity of the granulometric size of the fibers gives different average apparent densities and, as a result, different thermal conductivities. The difference in the straw surface is an essential detail that is important for the formation of the composition (Savitsky, N. V. et al., 2012; Novosad, Petro V., et al., 2019; Savytskyi, M., et al. 2015).

The nature of the filler surface is of great importance when forming the structure of a newly composed material. The rough surface of the particles of flax and hemp straw has a positive effect on the degree of adhesion of the aggregate to the matrix of the binder. Hence, the subsequent research was focused on the study of the lightweight concretes based on flax and hemp straw.

According to the defined methodology, the tests of the mechanical and physical properties were carried out. The results of the tests performed according to the mechanical and physical studies are given in Table 4.

The flax straw-based concrete showed better thermal properties, while the hemp-based concrete showed better strength characteristics. At the same time, it is noted that the difference in strength coincides with the difference in the thermal conductivity.

The temperatures of the thermal decomposition of the composites based on the Difference Thermo Gravimetry (DTG) curves (Fig. 3) are given in Table 5.

As is shown in the DTG curves (Fig. 3), the composites decomposed in several steps. The thermal degradation of the flax composite was manifested by four mass-loss peaks, while the degradation of the hemp composite consisted of three steps represented by the mass loss. The second peaks at about

Tab. 5 Temperature *ranges of the degradation and corresponding mass losses (air atmosphere) of the straw-based lightweight concrete components*

Sample	Temperature ranges of degradation of components, °C in an air atmosphere				
	1st peak	2nd peak	3rd peak	4th peak	Total mass loss,%
HSC	-	103.0	277.9	-	46.94
FSC	70.0	108.1	278.9	807.4	53.08

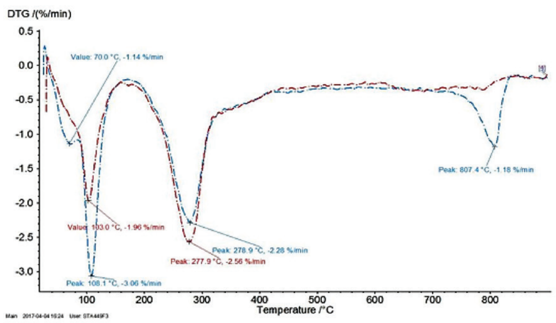

Figure 3: DTG curves for flax and hemp straw-based lightweight concretes:

Fig. 3 *DTG curves for flax and hemp straw-based lightweight concretes:*

■ - flax straw-based lightweight concrete;
■ - hemp straw-based lightweight concrete

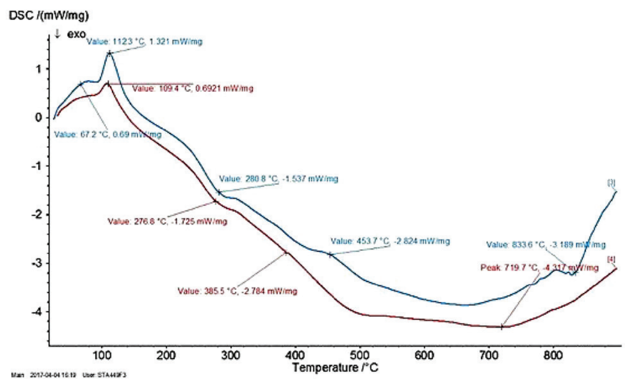

Fig. 4 *DSC curves of the flax and hemp samples:*

■ - flax straw-based lightweight concrete;
■ - hemp straw-based lightweight concrete

100 °C and the third peaks at about 300 °C represent the decomposition of the organic compounds. Based on these temperatures, when comparing the flax and hemp-based samples, the flax-based one degrades at higher temperatures.

The thermal decomposition process for the flax concrete is more complex, but at the same time, it is accompanied by the release of more energy according to the DSC curves in Fig. 4, which probably refer to the totally organic decomposition of the flax concrete. This is considered to be an important aspect in the context of the life cycle assessment of the stage of material recycling as, for example, the energy source.

CONCLUSIONS

The research presented defined future possibilities of agricultural waste, i.e., flax and hemp straw for lightweight concrete production. They have important properties as raw material, i.e., the fibers` jagged surface and thermal conductivity coefficient of 0.0465-0.085 W/(m·K), which permit them to be used as an effective filler for lightweight concretes and composite insulation materials. The ratio mixes of hemp and flax straw-based concretes have been developed in terms of sustainability principles such as environmental friendliness and energy efficiency. Straw-based lightweight concretes have been compared with and without using Portland cement (PC), which showed that the hemp concrete with the use of PC has a strength 5.6 % higher at a 10% deformation, and, at the same time, a 13 % higher thermal conductivity coefficient than the flax concrete. Thus, from the point of view of energy efficiency, lightweight flax concrete of the proposed composition is more favorable for sustainable constructions. The physical-chemical study has shown that the overall picture of thermal degradation for flax and hemp concretes is similar. Nevertheless, additional peaks of mass loss were defined for flax concrete accompanied by an exothermal process, which is a positive aspect when taking into account the life cycle of a material and its recycling stages.

Acknowledgments

This work is partially supported by the Visegrad scholarship project 52111088.

REFERENCES

Gurwitt, S., Malkki, K. & Mitra, M. (2017) *Global issue, developed country bias: the Paris climate conference as covered by daily print news organizations in 13 nations. Climatic Change* 143, 281–296. https://doi.org/10.1007/s10584-017-2004-2

Paiva, R.d.L.M.; Caldas, L.R.; Martins, A.P.d.S.; de Sousa, P.B.; de Oliveira, G.F.; Toledo Filho, R.D. (2021) *Thermal-Energy Analysis and Life Cycle GHG Emissions Assessments of Innovative Earth-Based Bamboo Plastering Mortars*. Sustainability, 13, 10429. https://doi.org/10.3390/su131810429

Pryshliak, N., & Tokarchuk, D. (2020) *Socio-economic and environmental benefits of biofuel production development from agricultural waste in Ukraine.* Environmental & Socio-economic Studies. 2020. Vol. 8. No. 1. pp. 18-27.

Bakatovich A.A., Davydenko N.V. (2009), *Pat. 20091414 The Republic of Belarus MPK C 04B 28/00, C 08B 18/04. Mixture for insulation material* /: applicant and patent holder Educational Institution "Polotsk State University". — № 20091414; 10.05.09; published 30.04.11.

Stevulova N., Kidalova L., Junak J., Cigasova J., Terpakova E. (2012) *Effect of hemp shive sizes on mechanical properties of lightweight fibrous composites*/ Procedia Engineering – Vol. 42. – pp. 496–500.

Craig Schluttenhofer, Ling Yuan (2017), *Challenges towards Revitalizing Hemp: A Multifaceted Crop*, Trends in Plant Science, Vol. 22, No. 11, pp. 917-929, ISSN 1360-1385, https://doi.org/10.1016/j.tplants.2017.08.004.

Salim Barbhuiya, Bibhuti Bhusan Das (2022), *A comprehensive review on the use of hemp in concrete*, Construction and Building Materials, Vol. 341, 127857, ISSN 0950-0618, https://doi.org/10.1016/j.conbuildmat.2022.127857.

Meijer, W. J. M., van der Werf, H. M. G., Mathijssen, E. W. J. M., & van den Brink, P. W. M. (1995) *Constraints to dry matter production in fiber hemp (Cannabis sativa L.)*. European Journal of Agronomy, 4, 109-117. https://doi.org/10.1016/s1161-0301(14)80022-1

Vonapartis E., Aubin M.P., Seguin P., Mustafa A.F., Charron J.B. (2015) *Seed composition of ten industrial hemp cultivars approved for production in Canada*. J Food Compost Anal 39:8–12

Rehman, M., Fahad, S., Du, G. et al. (2021) *Evaluation of hemp (Cannabis sativa L.) as an industrial crop: a review*. Environ Sci Pollut Res 28, 52832–52843. https://doi.org/10.1007/s11356-021-16264-5.

Manian A.P., Cordin M., Pham T. (2021) *Extraction of cellulose fibers from flax and hemp: a review*. Cellulose 28:8275–2894. https://doi.org/10.1007/s10570-021-04051-x

Nikolsky, S.N., Zlenko, D.V., Gatin, A.K. et al. (2022) *Oil flax straw processing and utilization*. Biomass Conv. Bioref. https://doi.org/10.1007/s13399-022-02584-0

Anthony W.S. (2002) *Separation of fiber from seed flax straw*. Appl Eng Agric 18(2):227–233. https://doi.org/10.13031/2013.7788

Zhu, J.; Zhu, H.; Njuguna, J.; Abhyankar, H. (2013) *Recent Development of Flax Fibres and Their Reinforced Composites Based on Different Polymeric Matrices*. Materials, 6, 5171-5198. https://doi.org/10.3390/ma6115171.

Babenko M., Estokova A., Savytskyi M. and Unčík S. (2018) *Study of Thermal Properties of Lightweight Insulation Made of Flax Straw*, Slovak Journal of Civil Engineering, vol. 26, no. 2, pp. 9-14. https://doi.org/10.2478/sjce-2018-0008

DSTU B.V.2.7 - 214: 2009. Building materials. **(2009)** *Concretes. Method for determining the strength of control samples*. - K .: NIISK, Kievgorstroy, 2010.

GOST 12730.2 – 78 (1979) *Concretes. Method for determination of humidity*. - Moscow: Publishing Standards.

BI-TO 21 (2000) *Technical description and operating conditions* - OOO Budindustriya LTD, Ukraine - 25 pp.

DSTU B V.2.7-41-95 (1996) *Materials and products of building. Method for determining the thermal conductivity by a surface transformer*: - [Effective from 01/01/1996]. K: Minregiodobud of Ukraine, 1996 – pp. 11-23 (National Standard of Ukraine).

Savitsky, N. V. et al. (2012) *Thermotechnical characteristics of organic heat insulators from local materials for the construction of ecological buildings.* Theoretical foundations of everyday life. Zb. Sciences. Praci: 373-376.

Novosad, Petro V., et al. (2019) *Porous thermal insulation materials on organic and mineral fillers*. International Conference on Current Issues of Civil and Environmental Engineering, Lviv-Košice–Rzeszów. Springer, Cham.

Savytskyi, M., et al. (2015) *Integrated use of agricultural waste for the sustainable development of agricultural socio-eco-complexes as closed ecosystem*. Constr Mater Sci Mech Eng 82: 179-186.

Slovak Journal of Civil Engineering

Vol. 30, 2022, No. 4, 17 – 22
DOI: 10.2478/sjce-2022-0024

THE EFFECTIVENESS OF THE IMPLEMENTATION OF RESEARCH RESULTS IN A TECHNOLOGICAL SCHEME OF WATER PURIFICATION

Olena GALKINA[*1], Sergiy KUNYTSKYI[2], Tamara SHEVCHENKO[1]

Abstract

The paper proposes technical solutions for the use of the reagent method of water preparation at coke plants in order to bring it to a quality suitable for use in the circulating water supply system of the PJSC Kharkiv Coke Plan. It is proposed to dilute phenolic water in a biochemical installation in a mixer before purification and to purify water with a flocculant. The paper recommends dosing the flocculant solution automatically using a preparation station. Additional purification of the clarified water is carried out using a filtration unit with a filter media from a layer of quartz sand. The economic effect from the implementation of the technical measures is achieved not only due to the reduction in fresh water consumption by 60 540 m3/year and the cessation of the discharge of phenolic water into the city sewer network, but also the replacement of the reagent with a more efficient one and a decrease in its consumption. It has been found that the introduction of the technical solutions for the circulating water supply system is economically and environmentally justifiable.

Address

[1] Dept. of Water and Wastewater Engineering, O.M. Beketov National University of Urban Economy (O.M. Beketov NUUE), Kharkiv, Ukraine

[2] Dept. of Research, National University of Water and Environmental Engineering, Rivne, Ukraine

* ***Corresponding author:*** helen.smilka31@gmail.com

Key words

- Purification,
- Coke plants,
- Effectiveness,
- Flocculant,
- Phenolic water.

1 INTRODUCTION

In today's environmental conditions, industrial waste water purification regulations are becoming more restrictive. Therefore, there is a need to develop new technological solutions that will ensure the high efficiency of technological water purification of industrial enterprises, including coke plants. It is recommended to use technology for the utilization of phenolic waste water from coke plants, which allows minimizing and, in some cases, preventing the discharge of phenolic waste water into a city sewerage system (Bargieł, P., Zabochnicka-Świątek, M., 2018; Pal, P., Kumar, R., 2014; Lei, G. et al., 2004; Chenglong, Y., et al., 2000; Kwarciak-Kozłowska, A., et al., 2011; Shatnyi, S., Kunytskyi, S., Volkov, V., Shatna, A., 2021).

Depending on the nature and concentration of contaminants contained in waste water from coke plants, as well as on the directions for the use of this water, it can require different preparations (Lei, G. et al., 2004).

A peculiarity of coke-chemical production technology is determining a significant amount of waste water in the process of coking coal charge, capturing and processing the chemical products. Waste water is formed in chemical plants (phenolic waste water) in the process of quenching coke during the cooling of coke oven gas. The largest source of water pollution is the excess ammonia water formed from the pyrogenetic moisture of the charge. An analysis of the quality of the waste water from coke-chemical production showed the following characteristic contaminants: suspended solids, resins and oils, phenols, ammonia, cyanides, rhodanides, organic matter, BOD5, etc. (Bargieł, P., Zabochnicka-Świątek, M., 2018; Pal, P., Kumar, R., 2014; Lei, G. et al., 2004; Chenglong, Y., et al., 2000).

The complex qualitative composition of phenolic waste water and a large amount of chemical pollution creates a number of difficulties in its purification and implementation into the technology of a plant and therefore requires several stages of purification.

Filtration and coagulation are used to remove resins and oils in water. More often, water filtration is carried out on gravel filters, the efficiency of which is 85 %. The advantage of this method of purification is the relatively low cost of the process, while a disadvantage is the lack of the degradation of pollutants (Bargieł, P., Zabochnicka-Świątek, M., 2018; Chenglong, Y., et al., 2000; Lee, C. S., Robinson, J., Chong, M. F., 2014).

Phenolic waste water purification technologies involve the use of a complex of physicochemical and biological methods, including nitrification, denitrification, etc. (Bargieł, P., Zabochnicka-Świątek, M., 2018; Pal, P., Kumar, R., 2014; Lei, G. et al., 2004; Chenglong, Y., et al., 2000). The complexity of the mechanism for the purification of phenolic water is explained by the fact that phenolic water is classified as hazardous water (among industrial waste waters) and as a source of environmental pollution.

As a result of the analysis performed, it has been determined that the purification of phenolic waste water from coke plants is ineffective and is caused by insufficient treatment at biochemical plants. This is due to insufficient purification at the previous stages, in particular at the physico-chemical stage of the purification of water from suspended solids, resins, oils, etc. Therefore, the improvement of reagent water treatment processes at coke plants is the main factor in the preparation of water for reuse in water supply systems.

Thus, the purpose of the work is to develop and apply effective technological and environmental solutions for the purification of phenolic waste water at coke plants with the industrial testing of the application of the solution. In the present work, we have developed methods using effective reagents and the method of dosing these reagents, together with the additional purification of water with filters.

2 MATERIALS AND METHODS

2.1 Analysis of the technological scheme of water purification at the PJSC Kharkiv Coke Plant

The research was carried out in laboratory and production conditions on the circulating water supply system of the PJSC Kharkiv Coke Plant. Waste water purification at the PJSC Kharkiv Coke Plant is carried out at a biochemical installation. On the territory of the site there is a mechanical purification unit building:

– 2 filters loaded with coke breeze;
– 1 primary heat exchanger;
– 2 secondary heat exchangers;
– 1 resin settling tank;
–1 collector of water from the ammonia column;
–2 pumps;
–2 averaging settlers;
–1 tank for the coagulant.

The biological purification block building contains:

– 1 aeration unit;
– 1 water clarification unit;
– 1 water and sludge injection unit;
– 1 air supply unit;
– 1 panel board;
– 1 operating control room.

According to the technological scheme (Fig. 1), sewage treatment has the following sequence: after the ammonia column, the wastewater is collected in the storage of the condensation compartment collector. Then, after passing through the spiral heat exchanger, it enters the waste water collector, from where it is pumped by a pump for cooling into the plate heat exchanger, after which the waste water with a temperature of 30-35 °C is fed into two concentrators, from which it flows by gravity to the oil separator for the purpose of the resin and oil removal. Next, the water is sent by gravity through the overflow tray to two aerotanks. Air consumption in the aeration tanks is at least 90 m^3 per 1 m^3 of waste water.

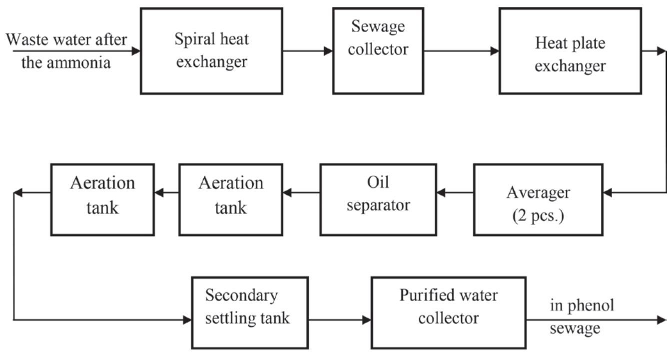

Fig. 1 *Technological scheme of the biochemical units at the PJSC Kharkiv Coke Plant*

After going through the second aeration tank, the purified waste water flows through the overflow tray into the secondary sump. The water separated from the activated sludge flows by gravity to the purified water collector, from where it is sent to the phenolic sewage system. The return of activated sludge to the aeration tanks from the bottom of the secondary sedimentation tank is carried out by a centrifugal pump.

The facilities of the biochemical installation (BCI) at the PJSC Kharkiv Coke Plant are used for:

– mechanical purification of waste water on filters with the loading of the coke breeze;
– physical and chemical purification with the use of a composite coagulant and settling in the averaging settler;
– biochemical purification in the aeration tanks.

2.2 Analysis of the quality of the purified waste water

The analysis of the quality of the purified waste water at the biochemical installation of the PJSC Kharkiv Coke Plant was carried out in accordance with standard methods.

The water quality control was carried out using a physico-chemical analysis of the samples according to standard methods of titration, complexometry, etc. (Baird, R. B., Eaton, A. D., Clesceri, L. S., 2012).

The water quality results showed an inconsistency with the requirements for the use of water in the circulating water supply cycle of the plant by several indicators (see Tab. 1). Thus, it is has been established that the concentrations of suspended solids, phenols and rhodanides in the purified water are higher and do not meet the requirements for the use of water in the reversible water supply cycle of the plant.

Tab. 1 *The results of the waste water quality analysis at the PJSC Kharkiv Coke Plant (Galkina, O., Blahodarna, H., 2019)*

Indicators	Indicator values, mg · dm-3		
	Before the biochemical unit	After the biochemical unit	For use in a reverse cycle established by the Kharkivkommunochist-vod trust
pH, ea	8.3	8.3	6.5-8.5
Suspended substances, mg · dm-3	300-500	60	40
Phenols, mg · dm-3	263	17	1-2
BOD full, mgO2 · dm-3	1800	150	150
Ester-soluble, mg · l -1	9	6	20
Sulfides, mg · l-1	1	1	1
Phosphates, mg · dm-3	3	3	5
SSAA, mg · dm-3	0,1	0,1	-
Total iron, mg · dm-3	5	3	4
Rodanides, mg · dm-3	955	47.2	5
Ammonium nitrogen, mg · dm-3	780	50	150
Petrochemicals, mg · dm-3	30	3	50
Cyanides, mg · dm-3	30	5.0	28
Salt content, mg · dm-3	1200	1200	2000

Note: Water quality results provided by the laboratories of the PJSC Kharkiv Coke Plant and "UkrVODGEO"

3 RESULTS AND DISCUSSION

3.1 Implementation of the research results into the water purification technological scheme

The results of the analysis of the existing state of the waste water purification of the plant, the water and sewage system, the study of various technical methods for the phenolic waste water purification, and the experience of other coke-chemical plants indicate the possibility of changing the existing water use scheme of the plant as follows:

- by mixing industrial and domestic waste water before purification;
- by preventing the discharge of phenolic effluents into the public sewer network;
- by increasing the efficiency of the biochemical purification installation.

Thus, in order to improve the waste water purification process at the plant and meet the requirements for its quality, a number of measures have been envisaged.

First, before the phenolic waste water is purified in a biochemical installation in order to dilute it, we propose to mix industrial waste water from the condensation department with domestic waste water in a mixer in a separate container with a volume of 100 m^3. This will reduce the concentration of phe-

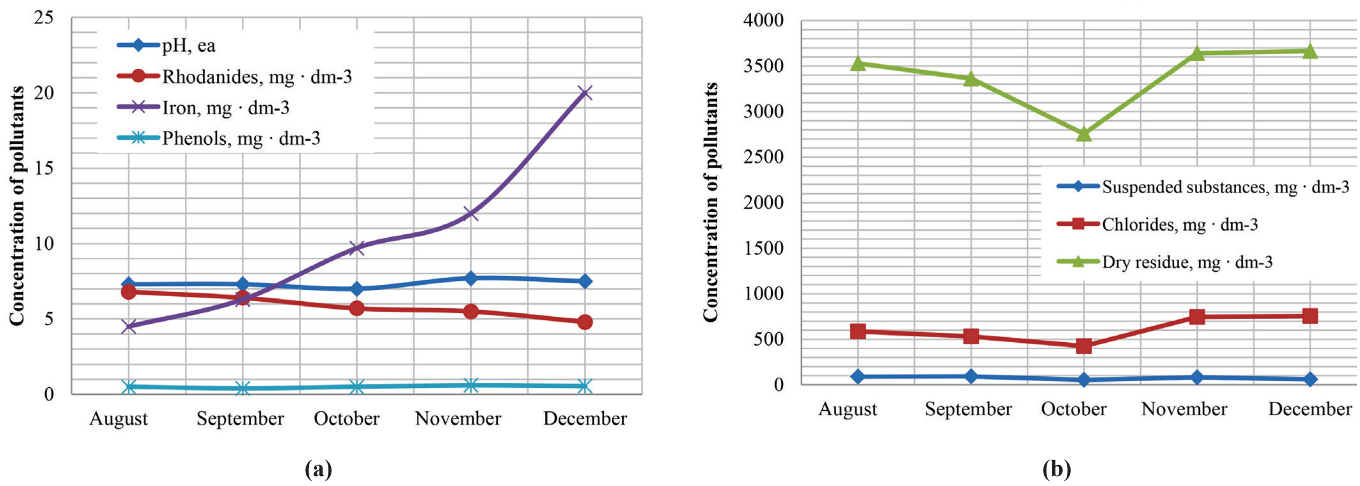

Fig. 2 *Effect of the Besfloc flocculants at a dosage of 4 mg · dm-3 on the quality of the circulating water (a, b) of the cycle of the primary gas coolers at the PJSC Kharkiv Coke Plant when using the Besfloc flocculant*

nols and thiocyanates in the purified water. Then the waste water can be filtered before entering the biochemical plant.

Secondly, it is possible to increase the efficiency of the biochemical purification installation by improving the biological purification and an additional deep purification of the water. For this purpose it is necessary:

– to intensify the process of the physico-chemical purification of phenolic water by using effective reagents (Besfloc or Extraflock flocculant with a recommended dose of 4 mg/dm^3);
– to dose the flocculant solution in the technological scheme of the phenolic water purification by means of the SPR 2100 BV reagent preparation station of the Ekoton Industrial Group (Ekoton Product Catalogue, 2018).
– to additionally purify the clarified waste water (after the secondary sedimentation tanks) with a filtration unit using a layer of quartz sand as a filtering load.

The effect of dosing a solution of Besfloc flocculant on the quality of circulating water was carried out in the circulating water supply system of the PJSC Kharkiv Coke Plant (Figs. 2 a, b).

The analysis of the water quality proves the effectiveness of its purification at a 0.1 % dosage of the flocculant solution. This reduces the content of the suspended solids from 500-600 mg · dm-3 to 50-100 mg · dm-3.

The efficiency of the flocculant application is explained by the proposed reagent supply technology (Galkina, O., Blahodarna, H., 2019):

– feeding the circulating water supply system with an effective quality of this water;
– using the method for dosing the flocculant solution;
– supplying water after the dosing reagents settle in a separate container.

In the technological scheme of the phenolic water purification, the flocculant solution is recommended to be dosed using the SPR 2100 BV reagent preparation station of the Ekoton Industrial Group (Lee, C. S., Robinson, J., Chong, M. F., 2014; Ekoton Product Catalogue: Ekoton Industrial Group (Ekoton), 2018) with a capacity of 100 liter per hour, made of a structural material, i. e., polypropylene.

The equipment is a two-chamber unit for the cyclical preparation of a polymer solution from a dry starting product and continuous dosing of the finished solution.

The preparation process takes place periodically or continuously in the upper chamber (solution preparation chamber); then, the finished solution is poured into the lower chamber (dosing chamber), where the finished solution for dosing has been selected. Dosing of the reagent into the upper chamber is carried out using a screw dispenser. The dry reagent is poured into the receiving tank. The receiving tank is equipped with a reagent level sensor and a vibrating device to prevent agglomeration of the bulk materials.

The recommended quality of the water purification for use in the reversible cycle is achieved by deep water purification after the secondary settling tanks. It is necessary to install an additional filtration unit using a layer of quartz sand as a filtering load (Klimov, S., Pinchuk, O., Kunytskiy, S., Klimova, A., 2019), to accomplish this.

We designed filters with an ascending stream. Water filtration occurs from the bottom up, which significantly improves

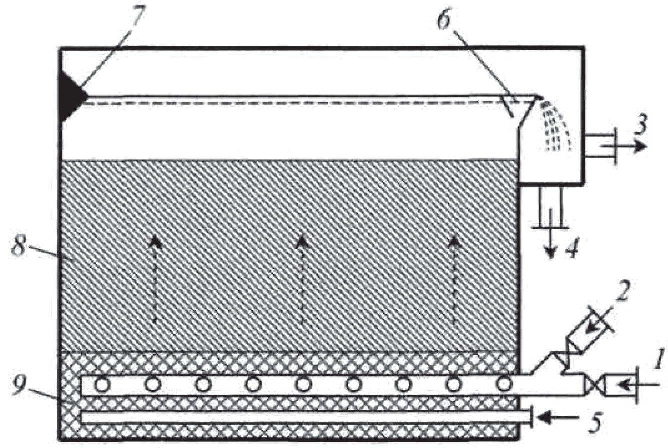

1 – water supply; 2 – flush water supply;
3 – filtrate discharge; 4 – wash water drain; 5 – air supply;
6 – sand-catching gutter; 7 – jet-directing protrusion;
8 – downloads; 9 – supporting layer

Fig. 3 *Filter with ascending water flow (Karmanov, A., Polina, I., 2022)*

the operating conditions of the filter as a result of the implementation of the principle of decreasing grain size along the flow (Fig. 3).

As a result of using this filter, the dirt holding capacity of the filter and the duration of the filter cycle increases, and also the silting of the fine-grained layers is excluded (Dushkin, S. S., Galkina, O. P., 2021). To remove such accumulations during the regeneration of the load before washing, it is necessary to blow the load with air for 10-15 minutes at an intensity of 18-20 l / s m^2. After blowing the load with air, it should be washed for 7 minutes with purified water. The filtrate is then discharged into a sludge compactor. Purified water flows by gravity into the purified water collector, from where the water is supplied by a network of pipelines to the circulating water supply cycle of the plant.

Waste water for additional purification is supplied to the filter from the clarified water collector after purification in the secondary settling tank. The unit consists of three filters with sand loading, as well as three piping systems (for each filter), which are designed to control and regulate the filtration process. The filter loading consists of a layer of quartz sand, under which there are several layers of gravel.

Tab. 2 *Designed quality of waste water purification on filters (Galkina, O., Blahodarna, H., 2019)*

Indicators	Average indicators	
	before filter , mg · dm-3	after filter, mg · dm-3
pH, ea	7-8.5	6.5-8.5
Suspended substances, mg · dm-3	60	20
Phenols, mg · dm-3	0.4	0.4
Rhodanides, mg · dm-3	5	5
Resins and oils, mg · dm-3	25	2
Cyanides, mg · dm-3	0.7	0.7

Thus, by reducing the amount of suspended solids to 20 mg · dm-3, the use of the proposed solution provides and allows for reusing the water in the circulating water supply system (Tab. 2).

Thus, the research results show that the implementation of the proposed measures makes it possible to achieve the required quality of the purified wastewater that will meet the requirements for the use of water for technical purposes of the circulating water supply cycle of the plant and ensure uninterrupted operation of the heat exchange equipment (Galkina, O., Blahodarna, H., 2019). Such purified waste water can be used for the technical purposes of the plant.

Provided that the above requirements are met, the quality of the purified waste water will meet the requirements for the use of water for the technical purposes of the circulating water supply cycle of the plant. The purified waste water can be used for technical purposes of the plant (Fig. 4).

It has been calculated that the introduction of a circulating water supply system at the plant (Fig. 4):

– will reduce the consumption of fresh water (artesian water from wells) from 241,200 m^3 in year to 180,660 m^3 in year;
– will reduce phenol emissions on the quenching tower by 10 times;
– will stop the discharge of phenolic effluents into the city sewer network.

Therefore, the introduction of this technical solution using phenolic effluent together with fresh water permits reducing the amount of reagents required for water purification, as well as significantly reducing the discharge of wastewater into the public sewer network and the withdrawal of fresh water from an artesian well. That is, through the introduction of these measures, a technical effect is achieved, as well as economic and environmental effects are achieved.

Reducing the discharge of water into the public sewer network and reducing the consumption of fresh water improves the state of the environment, i.e., the ecological situation at the plant and confirms the effectiveness of the proposed measures.

The economic effect of the introduction of water purification technology at the PJSC Kharkiv Coke Plant has been achieved by the introduction of a circulating water supply system, and the following technical solutions have been provided:

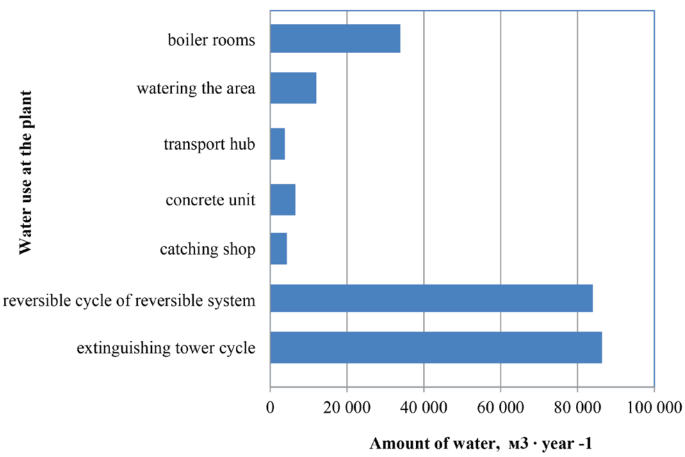

Fig. 4 *Use of purified water for technical purposes at the PJSC Kharkiv Coke Plant*

– the introduction of flocculant solutions using an automatic station for preparation of “Smart Mix” flocculant solutions;
– increasing the efficiency of the biochemical installation by adding additional purification of the filtration unit for clarification of waste water using a layer of quartz sand as a filter load;
– pipelines for the supply of technical purified water to the circulating water supply network of the plant.

The economic effect therefore consists of capital and operating costs, taking into account the effectiveness of the proposed measures (Goodstein, E. S., Polasky, S., 2017; Caputo, A. C., Pelagagge, P. M., Salini, P., 2008).

This technological solution involves the use of a solution of flocculant to intensify the process of water purification at the plant. To that end, there are additional costs associated with the use of reagents (replacement of the composite coagulant, i.e., a mixture of ferrous sulfate ($FeSO_4$) and aluminum chloride ($AlCl_3$) with Extraflock or Besfloc flocculant). In this case, cost savings are achieved by changing the reagent and reducing the dose.

So, the capital costs for the intensification of the water purification process at the coke plant include:

– the cost of the reagent preparation station;
– the cost of the filtration unit for water purification;
– the operating costs (installation of the equipment and the equipment maintenance costs).

The operating costs, in turn, take into account the following parameters:

– maintenance costs of the SPF 2100 reagent preparation station;
– maintenance costs of the filtration unit for waste water clarification using a layer of quartz sand as a filter load;
– maintenance costs for a mixer for the industrial and domestic waste water.

Thereby, the economic effect from the implementation of the results of the technical solutions (the use of an effective flocculant and additional water purification on the sand filters, taking into account the use of phenolic water as a supplying water) into the technological scheme of water purification at the plant in the first year of operation will be 49.5 US Dol / year.

4 CONCLUSIONS

It has been determined that the reuse of water in the circulating water supply system can be achieved by improving the quality of the purified water, i.e., the introduction of a number of measures in the technological scheme of the water purification at the coke plant. The results of the work were used during the development of technical solutions for the intensification of the water purification process at coke plants, particularly the PJSC Kharkiv Coke Plant.

It has been established that the introduction of technical solutions in the water purification process can be achieved by improving the biological purification units (using effective reagents) and by deep additional purification of the water after it is in secondary sedimentation tanks (using a filtration unit with a layer of quartz sand as a filtering load).

The economic and environmental effects are achieved by reducing the consumption of artesian water from wells by 60,540 m^3 per year and preventing the discharge of phenolic wastewater into the municipal sewerage network, as well as by replacing the reagent with a more efficient one and reducing its consumption.

It has been determined that the implementation of the technical solutions of the circulating water supply system at the PJSC Kharkiv Coke Plant is economically feasible and proves the positive effect of the proposed technical solutions.

REFERENCES

Baird, R. B. - Eaton, A. D. - Clesceri, L. S. (2012) Standard methods for the examination of water and wastewater (Vol. 10). E. W. Rice. Washington, DC: American Public Health Association.

Bargieł, P. - Zabochnicka-Świątek, M. (2018) *Technologies of coke wastewater treatment in the frame of legislation in force*. Environmental Protection and Natural Resources/Ochrona Środowiska i Zasobów Naturalnych, 29(1), 11-15.

Caputo, A. C. - Pelagagge, P. M. - Salini, P. (2008) *Heat exchanger design based on economic optimisation*. Applied thermal engineering, 28(10), 1151-1159.

Chenglong, Y. - Zhongjian, S. - Jinzhi, Z. (2000) *Problems and Solutions of Wastewater Treatment of Coking Plant [J]*. Water & Wastewater Engineering, *6*.

Dushkin, S. S. - Galkina, O. P. (2021) *Thin-Layer Sedimentation Tanks in Water Clarification at Coke Plants*. Coke and Chemistry, 64(8), 380-385.

Galkina, O. - Blahodarna, H. (2019) *The use of effective coagulants and flocculants to intensify the process of water purification at coke plants*. Slovak Journal of Civil Engineering, 27(2), 21-28.

Goodstein, E. S. - Polasky, S. (2017) *Economics and the Environment*. John Wiley & Sons.

Karmanov, A. - Polina, I. (2022) *Tekhnologiya ochistki stochnyh vod (Wastewater treatment technology)*. Litres.

Klimov, S. - Pinchuk, O. - Kunytskiy, S. - Klimova, A. (2019) *Limiting horizontal water filtration using drainage-screened modules.* Journal of Water and Land Development, (43), 90-95.

Kwarciak-Kozłowska, A. - Bohdziewicz, J. - Mielczarek, K. - Krzywicka, A. (2011) *Treatment of meat industry wastewater using coagulation and Fenton's reagent*. Civil and Environmental Engineering Reports, 6, 45–58.

Lee, C. S. - Robinson, J. - Chong, M. F. (2014) *A review on application of flocculants in wastewater treatment*. Process safety and environmental protection, 92(6), 489-508.

Lei, G. - Xiaojun, X. (2004) *Technologies of coke plant wastewater treatment.* INDUSTRIAL WATER TREATMENT-TIANJIN-, 24(3), 9-11.

Pal, P. - Kumar, R. (2014) *Treatment of coke wastewater: a critical review for developing sustainable management strategies*. Separation & Purification Reviews, 43(2), 89-123.

Product Catalogue: Ekoton Industrial Group (Ekoton) (2018) OOO EKO INVEST LTD. Available at: https://www.ekoton.com.

Shatnyi, S. - Kunytskyi, S. - Volkov, V. - Shatna, A. (2021, September) *Information Technology of Data Processing and Analysis on Automated Measuring Complex of Water Systems Stability*. In 2021 IEEE 16th International Conference on Computer Sciences and Information Technologies (CSIT) (Vol. 2, pp. 123-127). IEEE, 123-127.

sciendo Slovak Journal of Civil Engineering
Vol. 30, 2022, No. 4, 23 – 30
DOI: 10.2478/sjce-2022-0025

THE COMPACTION OF ENERGY AND PROPERTIES OF ROLLER-COMPACTED CONCRETE PAVEMENT WITH FILLERS

Nacira SAOUDI[1*], Hayet CHERFA[2], Brahim SAOUDI[1], Bodjemaa ZAANOUN[1]

Abstract

This case study aims to investigate the effects of compaction methods on the mechanical behavior of roller compacted concrete pavement (RCCP) mixtures, which consist of the replacement of different cement by 0%, 5%, and 10% limestone by volume fraction and which were compacted by two compaction methods. These methods are commonly discussed in the literature and were developed to simulate the site conditions in the laboratory. A modified Proctor test was adopted in the mix's proportional process to optimize the aggregate's percentage content of RCCP. The experimental series consisted of compression and split tensile performance tests to investigate the development of compaction performances at 28 days. The results showed that, where 10% of the cement was substituted by limestone, the RCC gives important flexural strength values compared to the quantity of the cement substitute. Qualitatively, the reduction in the strength of the concrete using the modified Proctor compaction method led to the weakness of the bond between the layers.

Address

1 Department of Civil Engineering, Akli Mohand Oulhadj University Bouira (UAMOB) Bouira, Algeria
2 University of Sciences and Technology Houari Boumediene, BP 32 Bab Ezzouar, 16111 - Algiers, Algeria

* ***Corresponding author:*** saoudinacira@gmail.com

Key words

- Proctor compaction,
- Concrete,
- Hammer,
- Pavements.

1 INTRODUCTION

The most important factor achieved during pavement projects is the high degree of rigidity, where the changes from last year's climate causes cracking, shrinkage, and fatigue, because of the temperature gradients.

Roller concrete pavement compacting methods do not reflect laboratory conditions, when the sub-product is incorporated for reinforcement, because of the lower energy of the compaction machines and their speed.

A concrete pavement is cost-effective and beneficial because of its sustainability and durability. The maintenance and renovation periods for such a pavement compared to other pavements are relatively long. The standard methods used are the ASTM C1176 vibrating table and the vibrating hammer found in (ASTM, 2014; C1435, EN 13286-51) ; the modified Proctor ASTM WK59339, and the Superpave Compactor Gyrators (SGC) (ASTM WK33682).

Roller compacted concrete (RCC) technology offers a viable alternative for many construction projects such a pavements, dams, airports, and parking lots, mainly due to its rapidity and economic advantages (Aghaeipour and Madhkhan, 2020).

(Şengün et al, 2019) noted that the ideal laboratory compaction methods in terms of the strength and compaction ratio within the acceptable Vebe consistency time were determined to be the SGC first and the vibrating hammer second. We have recapitulated studies on RCC focused on such mixture parameters as the type of aggregate, the gradation, the amount of cementitious material and water, and their effects on the RCC performance, including the resistance to frost, the effects of the water-to-cement (W/C) ratio, waste aggregates, and nano

SiO_2 (Chhorn and Lee, 2017; Hazaree et al., 2011, Madhkhan et al., 2012; Vahedifard et al., 2010; Harrington et al., 2010; Shen et al., 2020; Rahmani et al., 2020; Tavakoli et al., 2020).

In the present work, the performance of RCC containing a local commercialized limestone as a cementitious replacement material and two different compaction energies were investigated. Uniaxial compressive strength *[σ (MPa), t (second)]* and Extensometer compressive *[σ (MPa), ε (µm) diametral deformation]* tensile tests at two different temperatures were performed on specimens containing water to a constant binder ratio, but the W/C depended on the quantity replaced of the limestone.

2 MATERIALS AND METHODS

2.1 Materials

The cement used was Portland CPJ -CEM II/B 42.5 R, conforming to NA 442, EN 197-1 and norm NF P 15-301194 with compressive strengths of 11.2 MPa and 46 MPa, and flexural strength of 7.5 MPa and 9.5 MPa at 2 and 28 days, respectively. The ordinary cement had a specific weight and surface area of 3.06 g/cm^3 and 5000 cm^2/g, respectively.

The Portland Cement Association (PCA) has proposed an aggregate gradation for RCC pavements, which is applied and similar to the gradation of an intermediate asphalt layer (Harrington et al, 2010). In this investigation, however, we opted for the materials actually used by companies, so as to identify problems in the field.

Local sand (Kef Azrou), with a fineness modulus of 3.08, ES Sand equivalent to 52.89, a density of 2.70, and 24 h water absorption of 0.69% was used in all the mixtures (Harrington et al., 2010). A maximum size of an aggregate as small as 13 mm can be used to reduce segregation, enhance cohesiveness, and provide a closed surface. The two coarse aggregate classes used in this investigation had a maximum nominal size of 15 mm, a specific density of 2.53, and a 24 h water absorption of 1.79%. However, for the medium coarse 3/8 aggregate, the 24 h water absorption is 1.05%; the Los Angeles abrasion coefficient is respectively LA=31.24% and 27.44% for the coarse 3/8 and 8/15 mm aggregates). The grading curves of the coarse and fine aggregates were within the NF EN standard, as shown in (Figure1).

The percentage of fine sand passing through the sieve (0.08 mm) was 19%, but for the optimum mix chosen, the percentage is 7%. The Portland Cement Association (PCA) and American Concrete Institute (ACI) have limited the percentage of fine aggregate passing through a 200 sieve (0.075 mm) to 2–8% and a 100 sieve (0.150 mm) to 6–18% for sand used in RCCP. The limestone used presented a granulometry size of less than 150 µm.

Tab. 1 *Limestone Characteristics*

Fe_2O_3	*MgO*	*$CaCO_3$*	*Fire loss masses*	*HCL*	*Duration*	*density*
0.01%	0.14%	99%	43.9%	0.005%	3	2.7

2.2 Optimization mixtures and the mixing procedure

The mixture should contain 50 – 65% of fine aggregate passing N°. 4 (4.75 mm) [(Khayat and Libre, 2014), which consists of 2–8% of aggregate finer than N°. 200 (75 µm) (Harrington et al, 2010).

The fresh properties and hardened strength of the concrete are strongly influenced by the aggregates (Lin et al., 2011; M. Rao et al., 2016). Moreover, the most efficient way to achieve workable and high strength RCCP is by providing a well-graded aggregate (Harrington et al., 2010; Luhr, 2006; Khayat and Libre, 2014).

In this study, where the mixing procedure and proportions are realized in two parts, we firstly optimized the coarse aggregate's density; secondly, we investigated the liant (mortar).

2.2.1 Optimisation of aggregates

First, five combinations of the coarse aggregates were initially prepared to produce the RCC (see Table 2); without using any limestone, the cement content in the RCC usually has been recommended to be between 11% and 13% by weight of the concrete and oven-dried aggregates.

Tab. 2 *RCC Composition using density method (compactness)*

Mixes	Gravel 3/8	Gravel 8/15	density
1	20%	80%	2.50
2	25%	75%	2.53
3	30%	70%	2.56
4	35%	65%	2.60
5	40%	60%	2.49

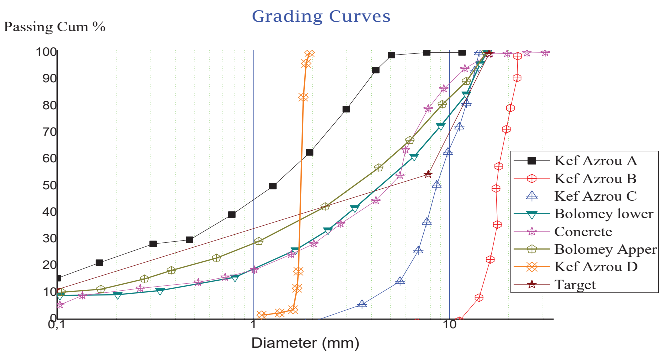

Fig. 1 *Grading curves of aggregates used.*

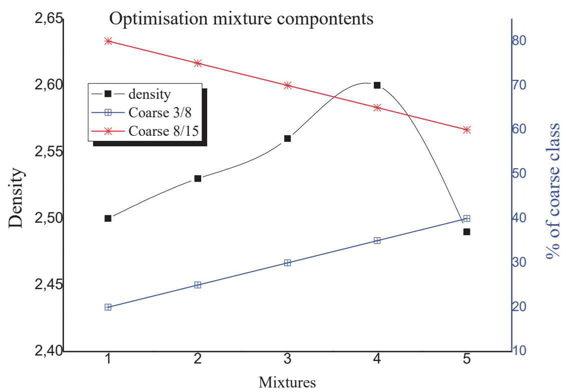

Fig. 2 *Optimisation of percentage mixtures of agregates*

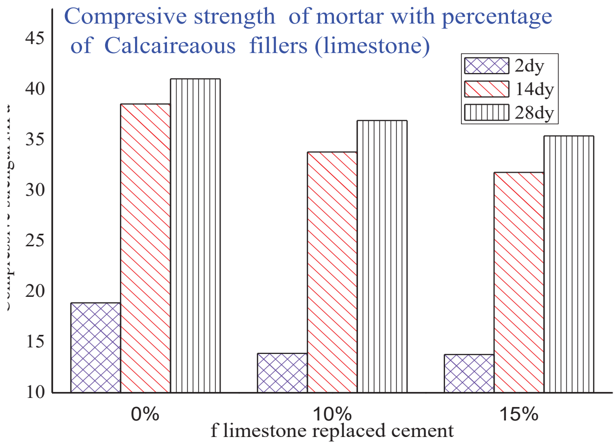

Fig. 3 *Compressive strength of standard mortar*.

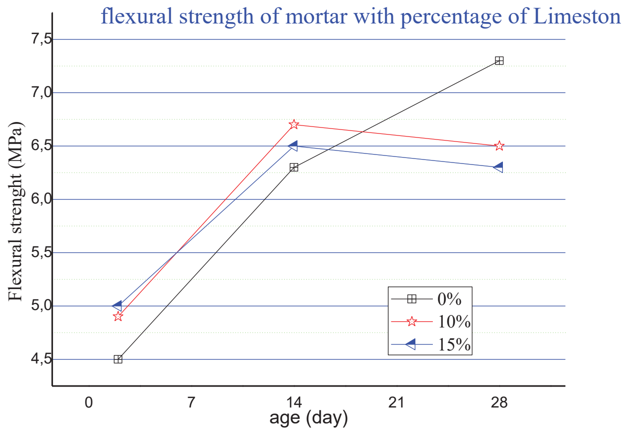

Fig. 4 *Flexural strength of standard mortar*

Therefore, in this experimental investigation, the weight of the cement was fixed at 11.4% of the total weight of the mixed concrete.

Figure 2 shows the suggested aggregate gradation mixed using the method based on the compactness. The maximum density is given with the fourth mixture.

2.2.2 Optimisation of the limestone mortar

Second, the local limestone's mechanical behavior was tested in standard mortar; the percentages of cement substituted are shown in Figure 3; the compressive strength decreases with the increasing percentage of the limestone substitute, but 10% of the limestone gives the important value of flexural strength compared to the quantity of the cement substitute.

The flexural strength of standard mortars increases with decreasing the limestone that replaces the cement, but the difference is minor, compared with the quantity of cement replaced until 28 days. The replacement of 10% of the cement by limestone reduces the flexural strength by about 1.5 MPa. This is an important result, both economically and environmentally.

Tab.3 Optimization *of limestone percentage in mortar standards*

Mixes [kg]	sand	3/8	8/15	cement	water	Limestone
LS0%	963	517	692	280	111	0
LS10%	963	517	692	252	111	28
LS15%	963	517	692	238	111	42

Furthermore, our research demonstrates the optimum composite mixtures that result in significant density were 963 kg, 517 kg, and 692 kg for the sand, 3/8 coarse aggregates and 8/15 coarse aggregates respectively, 280 kg of cement, and 111 liters of water.

In this study, three groups of RCCP were used, containing 0%, 10% and 15% (limestone) replacements of Portland cement by mass for two environmental conditions.

We have a constant value of the (water /binder), as the water content seems to be dependent on the compaction ratio and has a small effect on the strength (Şengün et al., 2019), The proportions of the mixture variants optimized in this investigation are presented in Table 3.

2.2.3 Preparation of specimens

The freshly-mixed concretes were molded in cylindrical molds; for the RCC with zero slump concrete, it needs to achieve an optimum density using modified Proctor compaction or a vibrating hammer.

The specimens of (15 cm diameter, 30 cm high) concrete corresponded to the California Bearing Ratio (CBR) used for Proctor compaction, with 55 hits for each layer.

The concrete mixture obtained was poured into the specially made molds in five layers and compacted by putting on a surcharge according to the Proctor standard.

The vibrating hammer is equipped with a shaft and a circular and rectangular steel plate area slightly smaller than that of the cylindrical steel mold, with a diameter ≥0.6 D, having a diameter of 12.2 cm.

To achieve the appropriate consolidation and compaction for the samples using the electric vibrating hammer, the concrete is placed in five layers in the pre-oiled molds. Each layer is compacted until rejection for one minute.

Fifty-eight cylindrical specimens were molded to determine the 28 days' compressive strength and the 28 days' split tensile strength for each case.

The samples were demolded one day after casting and then cured (25 °C with 15% humidity) for one group of specimens and 35 °C for the other. There was zero percentage humidity for the others until testing. Three samples were prepared for each test.

3 RESULTS AND DISCUSSIONS

3.1 Porosity

While the void index ratio for soil applications is calculated based on the dry density (ρ_d) for the RCCP specimens that are the subject of the study, the significant porosity ratio (η) was calculated based on the maximum theoretical free air of the fresh density of the concrete, considering the average (γ_s). This ratio was then used to compare the properties of the concrete samples compacted using the two methods.

The following equation (1. 2) was used to calculate the compaction ratio of the RCC specimens :

$$Sr \times e = \omega \times Gs \quad (1)$$

$$\rho_d = \frac{\rho_s}{1+e} \quad (2)$$

Sr: saturation degree [%]
e: void index ratio

ω: water content [%]
Gs: solid grain density
ρ_s: solid grain mass volumic [kg/m^3]
ρ_s: dry soil mass volumic [kg/m^3]

This chosen graded curve of the aggregates for RCC can guarantee the minimum void space, optimize the content of the paste, and provide compact, dense material and a smooth and tight surface.

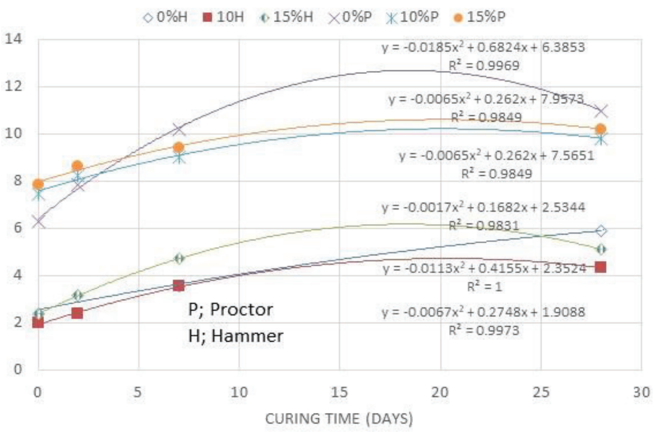

Fig. 5 *Relationship between porosity and curing time.*

In Figure 5, the relationship between the curing time and the porosity is seen for the low and high cement replacement dosage mixtures. It was realized that the porosity results are affected too much by the compaction method, i.e., around 50%.

The relationship took a polynomial form for the two compaction methods; the correlation coefficient was ($R^2 = 0.98 \approx 1$). As seen from the figure, the effects of the change in the compaction method in both the 10% and 15% limestone cement replacements resulted in lower porosity registered with the electric hammer vibrating method for the RCC mixtures.

3.2 Modified Proctor Compaction

The property most often used to describe the quality of concrete in practice is compressive strength. The 28 days' cylinder compressive strength should not be less than 17 MPa (Neville and Brooks, 1987). The compressive strength of RCC is comparable to that of conventional concrete and typically ranges from 28 MPa to 41 MPa.

For Proctor compaction (Figure 7), the compressive strength of the RCC was found to be lower than that of the conventional concrete estimated using various temperatures for the cement replacement given (Figure 8).

(LIU et al., 2007) confirms in their study that limestone powder has a filling, active effect and also an accelerating effect during the hydration process under conditions of a high temperature and steam curing. In this study, 20 MPa was obtained for a low cement dosage at 28 days at 20 °C, and 15% humidity, while only 24.51 MPa was obtained for the high cement dosage mixes (conventional). Moreover, the negative effect of decreasing the amount of cement and the negative effect of inefficient compaction (Proctor) can clearly be seen (Figure 8).

Fig. 6. *Specimen conditions*

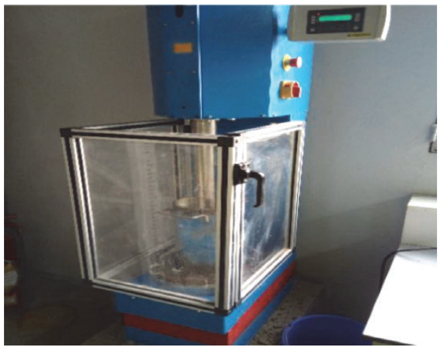

Fig. 7 *Proctor*

Using Proctor compaction at nearly 35 °C, the compressive strength decreases about 19% for the RCC substitute of 15% cement by limestone compared to the conventional RCC in the same temperature conditions.

It can also be seen that a high strength can only be reached through a combination of compaction and a high amount of cement. In this part we have limited tests on the concrete compacted with the Proctor standards, since (LaHucik and Roesler, 2017) in their study showed that the pair's compressive strength in the laboratory and the field core specimens (of the same size) were statistically different at a 95% confidence interval (LaHucik and Roesler, 2017).

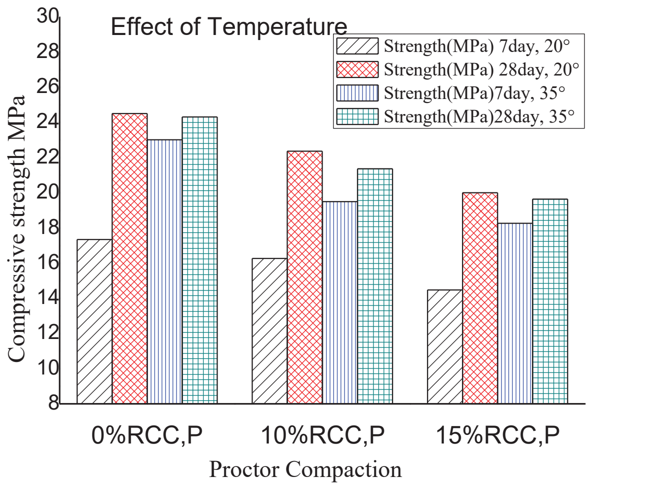

Fig. 8 *Compacted concrete compressive strength (Proctor compaction)*

Fig 9. *Hammer apparatus*

3.3 Vibrating electric hammer

3.3.1 Compressive strength (Comparison of two dosages)

For the first time we studied two cement dosages of 240 and 280Kg/m^3, with the aim of observing the compactibility of RCC pavements and confirming the effect of the capacity of the vibrating hammer apparatus (Figure 9) on the two conventional roller concrete mixtures.

In the literature, the cement content is around 300 kg/m^3 (Harrington et al., 2010). The lower dosage of 200 kg/m^3 was also utilized to cover the compacted concrete mixtures utilized in the dam type mass concrete.

In this investigation, the two cement dosages were tested using the electric vibrating hammer with the aim of determining their characteristics (Figure 10). The results indicate that similar density values for 240 Kg/m^3 and 280 Kg/m^3, respectively, were in a range of 2.31-2.36 and 2.45.

Figure. 10 shows the compressive strength at 7 and 28 days. The 280Kg/m^3 cement mixture has the highest compressive strength values in comparison with the mortar based mixture with 240Kg/m^3 in all the stages. The first mixture, which has a higher cement dosage, achieved 83.75% of its curing at 7 days; the second one achieved 84.24% of its total compressive strength. This could be caused by the constant binder-to-water ratio, the absorption of the cement paste, and the vibrating.

Compared to the compressive strength of the specimens containing trass (Ghahari et al., 2017), which is 35% lower than that of the plain concrete at early ages, this could be due to the low pozzolanic activity of the trass (volcanic tuff). In this study, the compacted concrete containing limestone (partial replacement of the cement) exhibited a 20% reduction in compressive strength after 28 days' curing. Zajac et al., (2014) reported that limestone powder does not have pozzolanic activity; it always remains unhydrated at the age of 28 days.

As seen in Figure 11, the compressive duration is affected by the amount of the limestone cement replacement used in the RCC mixture. Due to the compaction procedure, the maximum value of the 10% RCC sample approaches the plain RCC, as the amount of water utilized in the mixture was constant. As for the low cement replacement mixtures (10% RCC limestone), the vibrating hammer caused a higher degree of compaction when compared with the modified Proctor.

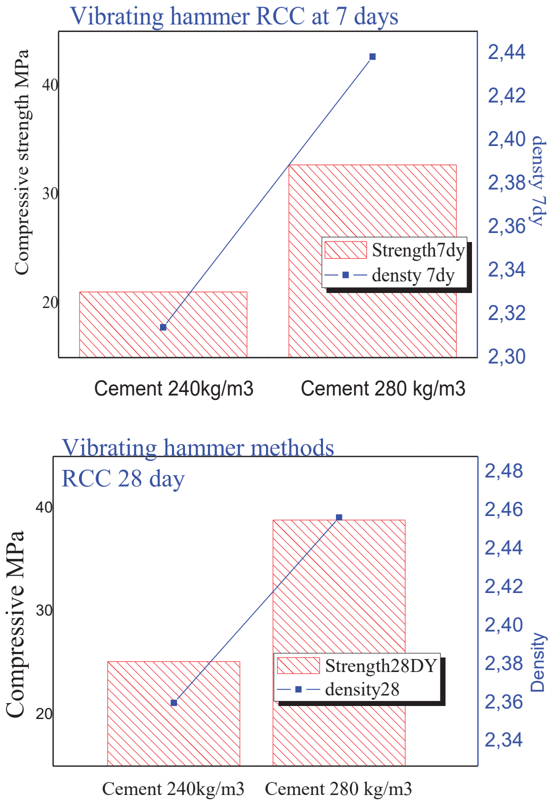

Fig. 10 *Relation between compressive strength and density*

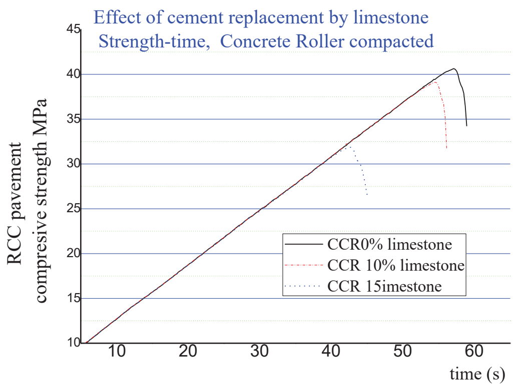

Fig 11. *Compressive Strength comparison [σ (MPa),t (second)]*

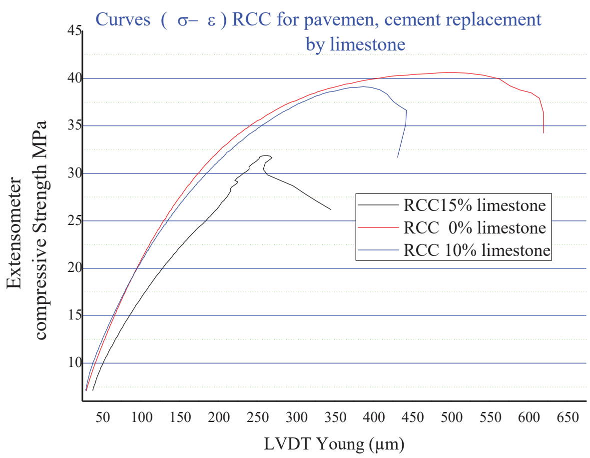

Fig. 12 *Compressive extensometer RCC, vibrating hammer [σ(MPa),ε(μm)]*

3.3.2 Extensometer Compressive

Compressive extensometer curves indicating the resistance of uni-axial compressive diametral-strength deformation for RCC are shown in Figure 12. In this part, the curves are presented at specified ages (28 days).

According to Figure 12, the deformations of the three groups grew linearly with increasing strength for the first parts, especially for the 0% limestone and LS 10 %. The figure shows that the two curves are superposed before 350 µm, although the values of the two curves do not exceed that of the 0%LS; the 10% mixture of the cement substitute by the limestone proved to be a homogeneous characteristic compared to the 15% LS.

The spliting tensile strength of the RCC mixtures at different W/C was determined at the age of 28 days. According to the literature, the RCCP can vary from 2 to 4 MPa (C D Atiş et al., 2004; Chi Huang, 2014; Cengiz Duran Atiş, 2005).

As shown in Figure 13, by increasing the limestone in the mixtures, the tensile strength slightly decreases. The variations in the split tensile strength results are related to the porosity of the RCC at 28 days, with specific hammer vibrating to compare the 0%, 10%, and 15% LS, as the split tensile strength values changed from a low to high amount of limestone peaks up to 3.45 MPa, which is a decrease of 6.37% and 7.24% (compared to 10% LS and 15% LS).

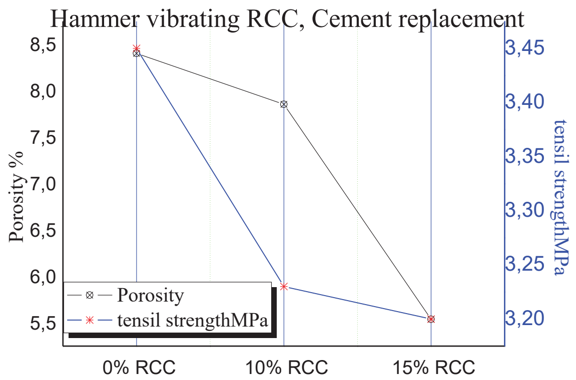

Fig. 13 *Tensile strength related to theoretical porosity.*

It appears that the substitution of the cement by limestone is not unfavorable to the split tensile strength of the specimens, which is related to the quantity of the cement substitute, i.e., only a difference of 7.24% in tensile strength between the plain and RCC 15% of the cement replacement. Compared to (Ghahari et al., 2017), the tensile strength of the specimens containing trass (volcanic tuff) is 12% lower than that of the plain concrete.

As observed, the cement replacement by limestone in RCC increases, whereas the theoretical porosity decreases. The results reported by other researchers are scattered due to the variations in materials used in the RCC mixtures.

3.3.3 Proposed relation of compressive and split tensile strengths

After investigating the feasibility of substituting cement by limestone (LS) powder as supplementary cementitious materials in RCC for a pavement, our experimental study focused on optimization of the compacity mixtures (aggregates, binder) and the mechanical properties at 28 days, including the compressive strength and splitting the tensile strength. The aim of this work is the possibility of developing a relationship between the laboratory characteristics of the data investigated.

The mechanical characteristics reported in Table 4 have been calculated from the mean values of three specimens. The analysis showed that the compressive and splitting tensile strengths are quite mathematically related using the hammer compaction methods, regarding the cement content (Rahmani et al., 2020). The relation between (f_t) and (f_c) can be expressed as a power law function. With the use of the regression analysis, the following relation was attained through the experimental data , R^2=0.91, for various water-to-cement (W /C) values.

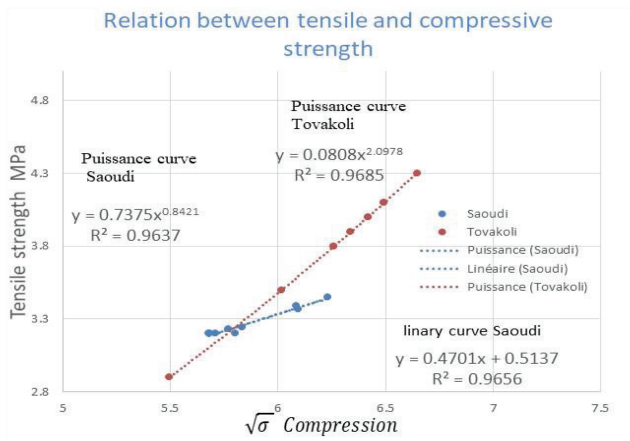

Fig.14 Relation *between compressive and tensile strength (straight line and puissance Relationship curve)*

It was reported that a loss of 1% to 2% in the density of RCC could cause a reduction of 10–17% in strength [(Amer et al., 2004)], but our investigation showed a gain of density is found in the limestone particles.

In application of the equation proposed by (Rahmani et al., 2020)'s equation $ft = 0.69\sqrt{fc}$, the data given in this paper are assigned as $ft = 0.4701\sqrt{fc} + 0.5137$, with a correlation coefficient $R^2 = 0.9656$ a constant W/C and variation of LS.

We proposed $ft = m\sqrt{fc}^{\ n}$, compared to the proposed linear equation. The results of this investigation are assigned as $ft = 0.7375\sqrt{fc}^{\ 0.8421}$, $R^2 = 0.9637$, for the (Tavakoli et al., 2020)'s data are reported as $ft = 0{,}0808\sqrt{fc}^{\ 2{,}0978}$, $R^2 = 0.96$.

Tab.4 Compressive *and tensile strength results using vibrating hammer.*

Compressive strength (MPa)	38.84	37.15	37	33.66	34	33.3	32.61	32.3	32.24
Spliting tensile strength (MPa)	3.45	3.37	3.389	3.2	3.246	3.232	3.2	3.2	3.2
Number of specimens	3	3	3	3	3	3	3	3	3

Tab.5 Recapitulation *of relationship between tensile strength and compressive strength*

	Equation	R^2	Equation	R^2	RCCP
Saoudi	$ft = 0.4701\sqrt{fc} + 0.5137,$	0.9656	$ft = 0.7375\sqrt{fc}^{\,0.8421}$	0.9637	limestone
(Lam et al., 2017)	$ft = 0.7356\sqrt{fc} - 0.3841$	0.8048	$ft = 0.3589\sqrt{fc}^{\,1.3583}$	0.9749	
(Rahmani et al., 2020)	$ft = 0.9279\sqrt{fc} - 1.4415$	0.9769	$ft = 0.3552\sqrt{fc}^{\,1.3668}$	0.9716	W/C. and C/A
(Şengün et al.,2019)	$ft = 0.9447\sqrt{fc} - 1.938$	0.8854	$ft = 0.1013\sqrt{fc}^{\,2.0203}$	0.8844	W/C and fine to total Aggregate ratio
(Tavakoli et al.,2020)	$ft = 1.3062\sqrt{fc} - 4.3768$	0.9745	$ft = 0.0808\sqrt{fc}^{\,2.0978}$	0.9685	Nano SiO_2 and replaced sand
(Shamsaei et al., 2017)	$ft = 1.0778\ln(fc) - 0.5718$ proposed $ft = 0.5428\sqrt{fc} + 0.1474$	0.9146 0.9476	$ft = 0.6238\sqrt{fc}^{\,0.9469}$	0.9672	Cross-linked polyethylene

In Table 5, as can be seen, the recent proposition of the relation between the compressive strength and tensile strength and the correlation coefficient R is important for the two propositions.

4 CONCLUSION

Advances in construction methods have facilitated the extensive use of zero-slump concrete in practice where zero-slump concrete gained attention as an innovative material with applications in concrete and roller compacted concrete (RCC). In this study, the effect of limestone and energy compaction on the mechanical behavior and specific density variations of roller-compacted concrete was investigated. The compaction methods that were used to produce RCC specimens in the LAFARGE laboratory and University of Bouira laboratory, in this paper are the Proctor and vibrating hammer.

1) The tests of local limestone in the standard mortar show that compressive strength decreases with an increasing percentage of cement substitute, but 10% of limestone results in a significant value of flexural strength compared to the quantity of cement substitute.
2) A high content of fine sand (19%) did not affect the compressive strength of RCC containing 10% and 15% cement at early ages of 1 and 7 days. However, there was a slight reduction of about 3% to 4% in the 28-day compressive strength of RCC containing 10% and 15% cement replacements, respectively.
3) The porosity results are affected too much by compaction methods; they were around 50%; a polynomial equation form relate the porosity and time of curing for the two compaction methods gives correlation coefficient (R^2 = 0,98–1).
4) With the Proctor compaction, the compressive strength decreases about 19% and 18.4% for the RCC 15% limestone compared to conventional RCC at temperatures of 35 °C and (20 °C with 15% humidity) respectively. Qualitatively, the reduction in strength of concrete made with the Proctor compaction may be the weak bond between the layers.
5) The use of a vibrating hammer instead of Proctor compaction in RCC using the same RCC contents significantly affects the theoretical porosity. Additionally, the low Proctor compaction energy decreased both the compressive and tensile strengths. Due to the vibrating hammer compaction procedure, it produced similar results on the compressive behavior curves between the plain and LS10%, although the amount of water utilized in the mixture was constant.
6) There was a reduction in compressive strength of about 20% at 28 days for the compacted concrete containing limestone (partial replacement of cement) using the modified Proctor.
7) The substitution of cement by limestone is not unfavorable to the split tensile strength of the compacted concrete specimens, which is related to the significant quantity of the cement substitute. Only a difference of 7.24% in tensile strength between the plain and RCC 15% of cement replacement was shown.
8) The RCC containing 15% of limestone showed the lowest compressive extensometer and an irregular curve σ=f(ε) in comparison with the RCC containing 0% and 10% limestone using the hammer compaction.
9) The results also showed that the relationship presented by the researchers for the W/C for the nano-silice can provide acceptable estimates of the (tensile and compressive, strength) f_t and f_c of the RCCP for different limestone contents.

REFERENCES

Aghaeipour, A. –Madhkhan, M. (2020) Mechanical properties and durability of roller compacted concrete pavement (RCCP)–a review. Road Materials and Pavement Design, 21(7), 1775–1798.

Amer, N. – Storey, C. – Delatte, N. (2004) Roller-compacted concrete mix design procedure with gyratory compactor. Transportation Research Record, 1893(1), 46–52.

ASTM. (2014). Standard practice for molding roller-compacted concrete in cylinder molds using a vibrating hammer.

Atiş, C D, Sevim, U. K. – Özcan, F.– Bilim, C. – Karahan, O. – Tanrikulu, A. H. – Ekşi, A. (2004) *Strength properties of roller compacted concrete containing a non-standard high calcium fly ash*. Materials Letters, 58(9), 1446–1450.

Atiş Cengiz Duran. (2005). *Strength properties of high-volume fly ash roller compacted and workable concrete, and influence of curing condition*. Cement and Concrete Research, 35(6), 1112–1121.

Chhorn, C.– Lee, S.-W. (2017). *Consistency control of roller-compacted concrete for pavement.* KSCE Journal of Civil Engineering, 21(5), 1757–1763.

Chi, M.– Huang, R. (2014). *Effect of circulating fluidized bed combustion ash on the properties of roller compacted concrete*. Cement and Concrete Composites, 45, 148–156.

Ghahari, S. A. – Mohammadi, A. – Ramezanianpour, A. A. (2017). *Performance assessment of natural pozzolan roller compacted concrete pavements*. Case Studies in Construction Materials, 7, 82–90.

Harrington, D. – Abdo, F. – Adaska, W.– Hazaree, C. V, Ceylan, H. – Bektas, F. (2010). Guide for roller-compacted concrete pavements.

Hazaree, C. – Ceylan, H. – Wang, K. (2011). *Influences of mixture composition on properties and freeze–thaw resistance of RCC.* Construction and Building Materials, 25(1), 313–319.

Khayat, K. H. – Libre, N. A. (2014). *Roller compacted concrete: field evaluation and mixture optimization. Missouri University of Science and Technology*. Center for Transportation Infrastructure and Safety, USA.

LaHucik, J. – Roesler, J. (2017). *Field and laboratory properties of roller-compacted concrete pavements*. Transportation Research Record, 2630(1), 33–40.

Lam, M. N. T. – Jaritngam, S. – Le, D. H. (2017). *Roller-compacted concrete pavement made of Electric Arc Furnace slag aggregate: Mix design and mechanical properties*. Construction and Building Materials, 154, 482–495. https://doi.org/10.1016/j.conbuildmat.2017.07.240

Lin, Y. Q. – Shi, Y. – Guo, D. M., Li, J. Z. – Yang, H. Q. (2011). *Study on site construction technology of four-graded RCC*. Advanced Materials Research, 250, 2927–2930.

LIU, J. – TIAN, Y. – Liu, Z. (2007). *Study on porosity of low-temperature concrete with mineral admixture.* Journal of Shenyang Jianzhu University (Natural Science), 4.

Luhr, D. R. (2006). *Frost Durability of Roller-Compacted Concrete Pavements: Research Synopsis*. Portland Cement Association.

Madhkhan, M. – Azizkhani, R. – Harchegani, M. E. T. (2012). *Effects of pozzolans together with steel and polypropylene fibers on mechanical properties of RCC pavements*. Construction and Building Materials, 26(1), 102–112.

Neville, A. M., & Brooks, J. J. (1987). *Concrete technology*. Longman Scientific & Technical England.

Rahmani, E. – Sharbatdar, M. K. – Beygi, M. H. A. (2020). *A comprehensive investigation into the effect of water to cement ratios and cement contents on the physical and mechanical properties of Roller Compacted Concrete Pavement (RCCP*). Construction and Building Materials, 253, 119177.

Rao, M. – Yang, H. – Lin, Y. – Li, J. – Shi, Y. (2016). Influence of maximum aggregate sizes on the performance of RCC. Construction and Building Materials, 115, 42–47.

Rao, S. K. – Sravana, P. – Rao, T. C. (2016). *Abrasion resistance and mechanical properties of Roller Compacted Concrete with GGBS*. Construction and Building Materials, 114, 925–933.

Şengün, E. **– Alam, B. – Shabani, R. – Yaman, I. O. (2019).** *The effects of compaction methods and mix parameters on the properties of roller compacted concrete mixtures*. Construction and Building Materials, 228, 116807.

Shamsaei, M. – Aghayan, I. – & Kazemi, K. A. (2017). *Experimental investigation of using cross-linked polyethylene waste as aggregate in roller compacted concrete pavement*. Journal of Cleaner Production, 165, 290–297. https://doi.org/10.1016/j.jclepro.2017.07.109

Shen, L. – Li, Q. – Ge, W. – Xu, S. (2020). *The mechanical property and frost resistance of roller compacted concrete by mixing silica fume and limestone powder: Experimental study*. Construction and Building Materials, 239, 117882.

Tavakoli, D. – Dehkordi, R. S. – Divandari, H. – de Brito, J. (2020). *Properties of roller-compacted concrete pavement containing waste aggregates and nano SiO2.* Construction and Building Materials, 249, 118747.

Vahedifard, F. – Nili, M. – Meehan, C. L. (2010). *Assessing the effects of supplementary cementitious materials on the performance of low-cement roller compacted concrete pavement*. Construction and Building Materials, 24(12), 2528–2535.

Zajac, M. – Rossberg, A. – Le Saout, G.– Lothenbach, B. (2014). *Influence of limestone and anhydrite on the hydration of Portland cements*. Cement and Concrete Composites, 46, 99–108.

Slovak Journal of Civil Engineering
Vol. 30, 2022, No. 4, 31 – 38
DOI: 10.2478/sjce-2022-0026

THE PRESSURE RESISTANCE OF ODOR TRAPS FOR SANITARY APPLIANCES AND THEIR IMPACT ON THE HYGIENE OF AN INDOOR ENVIRONMENT

Martin Sokol[1*], Jana Peráčková[1]

Abstract

The biggest problem with sanitary technology in high-rise buildings is the design of foul water stacks in which high negative pressure and overpressure values must not occur. When pressure exceeds maximum values, water from the trap is ejected, sucked out, or left bubbling in the trap. Measurements by other researchers have shown that when traps lose their function, in addition to the spreading of unpleasant odors, there is also the spreading of various viruses from the sewer and drainage systems. The paper deals with the mathematical analysis and simulation of the pressure resistance of different traps under various boundary conditions, considering the quality of the internal environment. The effect of water evaporation on pressure resistance was also simulated and assessed. The results of the work are clear tables of pressure resistances with a description of their effect on the water level in the trap.

Address

[1] Dept. of Building Services, Faculty of Civil Engineering, Slovak University of Technology in Bratislava, Bratislava, Slovakia

* ***Corresponding author:*** martin.sokol@stuba.sk

Key words

- Sanitary appliances,
- Odor traps,
- Hydraulic conditions in stacks,
- Simulations,
- Water evaporation,
- Public health.

1 INTRODUCTION

High negative pressure and overpressure in foul water stacks are often a problem of drainage systems in buildings. Nowadays, due to the increasing number of building floors and demanding layouts of sanitary rooms, the design of stacks is becoming more complicated. Existing standards are primarily focused on the design of stacks for buildings with a lower number of floors; for high and complicated stacks, it is necessary to proceed primarily from measurements taken outside Slovakia (Öngören and Weiss, 2018). Many factors influence pressure fluctuations in stacks. In addition to the correct design of dimensions, fittings, accessories, and ventilation, changes in the direction of stacks must also be resolved appropriately (Öngören et al., 2005). Overpressure most often occurs due to changes in the direction of stacks. Water bubbles in the traps at lower overpressures, while at a higher value, water is ejected from the sanitary appliances (Fig. 1b). Negative pressure occurs at the connection points of branch pipes with the flow or under a change of direction of the stack. When the negative pressure limit is exceeded, water is sucked out from the trap, which causes the spread of an annoying smell in the building (Fig. 1a) (Yabe et al., 2015). All these drainage system problems reduce the comfort of building users and endanger their health (Gormley et al., 2021). The first simulation task in Ansys 2021 Workbench R1 was to define the limiting values of the negative pressure and overpressure in a stack that negatively affect the functioning of the trap. The second task was to assess the effect of water evaporation on its pressure resistance.

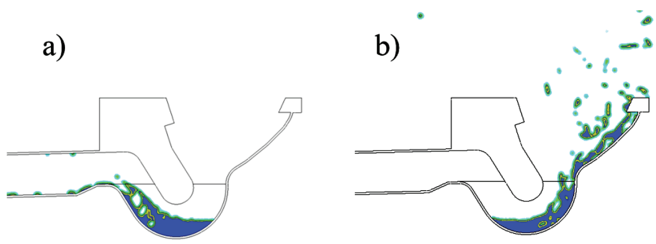

Fig. 1 *Effect of pressure fluctuations on the water in a trap a) suction of water from the trap, b) ejection of water from the sanitary appliance*

2 SPREAD OF ODORS AND VIRUSES IN HYGIENIC ROOMS

Odor traps protect a building's interior from the spread of annoying odors and possible viruses from a drainage or sewer system. A loss of trap functioning represents:

- complete water suction from the trap (Fig. 1a),
- bubbling of water in the trap (Fig. 13),
- ejection of water from the trap (Fig. 1b).

Many measurements outside Slovakia have been intensively carried out in recent years to address the presence of viruses in sewage and drainage systems, e.g., SARS-CoV-2 in human feces and urine (Gormley et al., 2020). The presence of this virus in the stool ranges from several tens of days in adults and an average of 5 days in children (Zheng et al., 2020). Several scientific and medical studies have confirmed drainage systems as a possible route of virus transmission to humans (Scheutz and Strockbine, 2015). The most common contact point for spreading viruses is sanitary appliances, especially water closets (WCs) (Scheutz and Strockbine, 2015). In addition to the contact areas with human skin, the loss of the functioning of traps poses a great risk of spreading viruses when the virus in the form of an aerosol is already spreading into the air during flushing (Hung et al., 2006).

3 FLOW OF WATER IN A FOUL WATER STACK

The water from a branch pipe hits the opposite wall of a stack at the point of connection and then falls downwards (Pomogaeva et al., 2018). As it falls downwards, water flows around the inner pipe walls, forming a hollow cylinder with an air core in the middle. At the connection point of the branch pipes with the flow, the air core closes, which causes a piston effect and the consequent creation of negative pressure (Fig. 2a).

During the piston effect, a large amount of air is sucked into the stack from the vent pipe. If the stack design is incorrect, the air is also sucked from the branch pipes, which causes the extraction of water from the trap. If the direction of the stack changes by more than 45°, the water stops flowing around the inner pipe walls, and the cross-section starts to fill up (Fig. 2b). Overpressure occurs above a change of direction, and negative pressure occurs below a change of direction (Fig. 2c) (Peráčková, 2018) (Cheng et al., 2004). If there is little or no flow in a stack, the air flows in the stack from the bottom to the top. The pressure loss that occurs in such a flow is one of the other causes of negative pressure in a stack (Vrána, 2021).

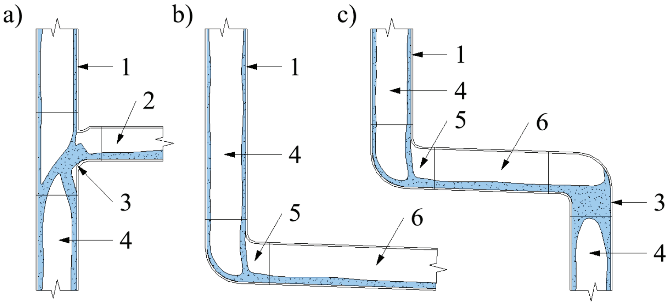

Fig. 2 *Water flow in the stack*
a) at the point of connection of a branch pipe, b) at the point of transition of the stack to the drain, c) at the point of the stack offset, 1 – water flow along the inner walls of the pipe, 2 – water flow from the branch pipe, 3 – the creation of a piston effect, 4 – air core, 5 – the impact of water on the wall of the arch, 6 – steady flow mode

4 MATHEMATICAL ANALYSIS OF THE PRESSURE RESISTANCE OF A TRAP

Stacks that exceed a 70 m limit must be assessed for maximum negative pressure (Valášek et al., 2005). The assessment consists of several parts, but in the end, the results are compared with the pressure resistance of the trap (Valášek, 1982). Traps are the only protection against the spread of annoying smells from a drainage system. According to EN 12056 and STN 73 6760, the minimum water level in the trap at the connection to a foul water pipe is h_{tot} = 50 mm, and at the connection to the rainwater pipe, it is h_{tot} = 80 mm, Fig. 3. Nowadays, traps with water levels of 50, 60 and 70 mm are most commonly produced. When designing foul water stacks, the height of the water level must be taken into account. The maximum pressure that the trap can resist Δp_{cr} (Pa) is calculated according to the formula:

$$\Delta p_{cr} = 1.1 \times \rho \times g \times h_{tot} \qquad \text{(Pa)} \tag{1}$$

where:
ρ - water density (kg/m^3),
g - gravitational acceleration (m/s^2),
h_{tot} - height of water in the trap (m) (Valášek, 1986).

According to formula (1), the pressure resistance of a trap with a 50 mm water level should be approximately 540 Pa (9.81 m/s^2, 999 kg/m^3) (Fig. 4). However, this calculation does not consider, for example, the effect of the shape of the trap. It is also impossible to detect unwanted concomitant phenomena when water starts bubbling in the trap due to overpressure or when the branch pipe starts to draw small amounts of air through the trap without disturbing the function of the trap (Figs. 10, 13).

In the 1980s, various questions arose as to whether the pressure resistance of the odor trap is affected by water evap-

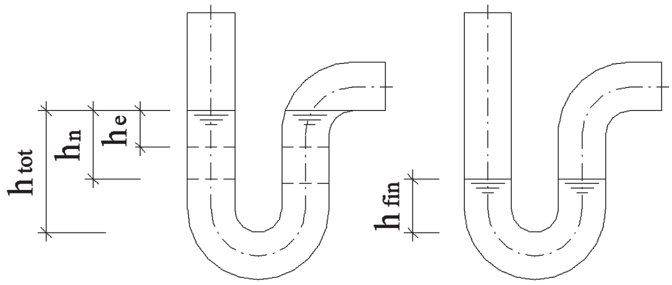

Fig. 3 *Odor trap*
h_{tot} – the height of the water in the trap, h_n – a decrease of water in the trap due to negative pressure, h_e – a decrease of water in the trap due to evaporation, h_{fin} - the height of water in the trap after evaporation and the suction of water due to negative pressure

oration (Dobromyslov, 1978). An experimental value of 0.5 mm/day at an indoor air temperature of 20 °C was used to account for water evaporation from the trap (Valášek, 1982). This value takes into account the following two factors: the replenishment of the water level due to the condensation of water vapor from the drainage system near the trap and the condensation of water on the inner surface of the trap, which also replenishes the water level. After modifying formula (1), we calculate the maximum pressure that the trap can resist, taking into account the evaporation $\Delta p_{cr,e}$ (Pa):

$$\Delta p_{cr,e} = 1.1 \times \rho \times g \times (h_{tot} - h_e) \qquad \text{(Pa)} \qquad (2)$$

where:

- ρ - water density (kg/m³),
- g - gravitational acceleration (m/s²),
- h_{tot} - the height of water in the trap (m),
- h_e - decrease of water in the trap due to evaporation (m) (Valášek, 1986).

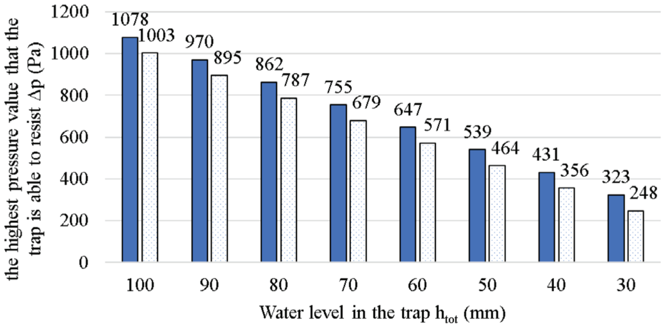

Fig. 4 *Resistance of the trap to pressure according to the water level* ■ *without taking into account evaporation according to Formula (1),* □ *taking into account the evaporation after 14 days of not using the sanitary appliance according to Formula (2)*

5 SIMULATION OF THE PRESSURE RESISTANCE OF A TRAP

Our simulation observed the effect of pressure fluctuations in a stack on the water level in the trap. Two reference traps, which are most commonly used for sinks or basins and toilets (Figs. 5a, c), were used. To compare the effect of water evaporation on the pressure resistance of a trap, different water level heights in the trap were used in Fig. 5a and in the experimental trap from Fig. 5b; pressure ranging from – 550 Pa to + 1500 Pa was simulated in the stack. The range of values was chosen based on various experimental measurements outside of Slovakia, where similar ranges of pressures were measured (Yabe et al., 2015). The boundary conditions of the simulation are shown in Fig. 6. The following inputs and settings were used for the simulation (Fig. 6):

- the trap contained water with a density of 999.1 kg/m³,
- air with a density of 1.225 kg/m³ was present in the stack and branch pipe,
- pressure values ranging from – 550 Pa to + 1500 Pa were generated in the stack (Yabe et al., 2015),
- calculations were performed with 1000 time steps, a time step length of 0.005 s, and a number of iterations per time step of 40.

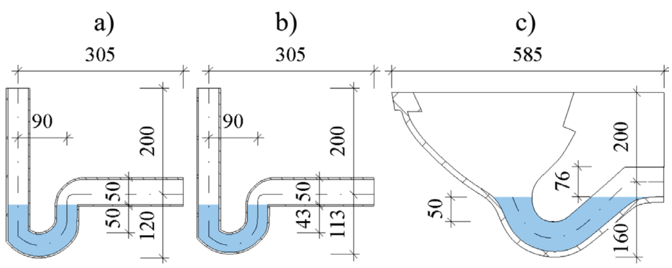

Fig. 5 *Shapes and dimensions of the traps used*
a) trap for sink or basin with 50 mm height of the water, b) experimental trap with 43 mm height of the water, c) trap for WC with 50 mm height of the water

The length of the calculations of one pressure value was approximately 3 h. Thirty different pressure values were assumed in the calculations for 2 types of traps, representing approximately 180 h of calculations.

The following water level conditions were monitored in the trap:

- water level fluctuations due to overpressure or negative pressure (without compromising the functioning),
- the suction of part of the water due to negative pressure (without compromising the function/ with compromising the functioning),
- complete suctioning of the water due to negative pressure (loss of function),
- water bubbling due to overpressure (loss of function),
- ejection of water due to overpressure (loss of function).

5.1 Quality of the mesh

The calculations generated a network with a number of elements ranging from 185 643 (sink, basin) to 185 867 (WC), depending on the type of trap. The details of the computational network are shown in Fig. 7. Based on the assumed accuracy of the computations, it can be concluded that the computational network has a very good quality.

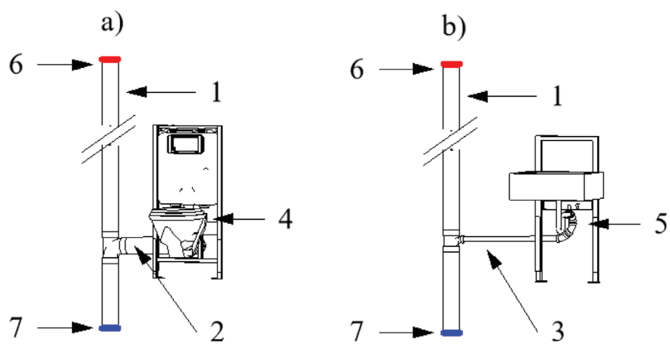

Fig. 6 *Simulation of boundary conditions*
a) WC connection to the stack, b) connection of the sink or basin to the stack, 1 – DN 100 stack,
2 – DN 100 branch pipes with a length of 1 m, 3 – DN 50 branch pipes with a length of 1 m, 4 – the trap for WC with a water seal height of 50 mm, 5 – the trap for the sink or basin with a water seal height of 50 mm, 6 – pressure outlet (atmosphere), 7 – pressure inlet (– 550 to + 1500 Pa)

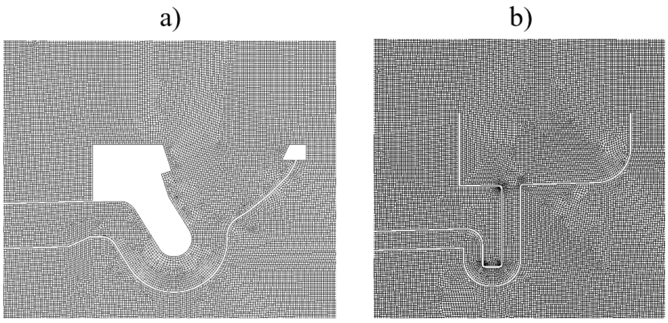

Fig. 7 *Quality of the mesh*
a) the trap for the WC, b) the trap for a basin or sink

5.2 Simulation of the effect of negative pressure on the water level in the trap

The traps from Figs. 5a, c were tested for negative pressures ranging from 0 to 550 Pa. The above-mentioned water level conditions were observed in the trap, see section 4. The toilet trap, which could withstand a negative pressure of p_n = 525 Pa without any loss of function, achieved the best results in this test. The trap for the basin or sink withstood a negative pressure of p_n = 475 Pa. The detailed simulation results are shown in Tables 1 and 2.

From the point of view of safety, the lowest risk of sucking water out of the water seal is the negative pressure $p_n \leq 300$ Pa. At these values, the water drop in the trap is minimal (Fig. 8). The safest design method is to assess the stacks for a negative pressure $p_n \leq 300$ Pa.

Tab. 1 *Effect of negative pressure on the water level in the sink trap*

Negative pressure p_n (Pa)	Effect on the water level
≤ 300	without compromising its functioning, drop in water minimal
300 to 450	without compromising its functioning, drop in water up to 25 mm
450 to 475	compromising its function, drop in water up to 30 mm, suctioning of air from the interior
> 475	loss of functioning, complete suction of water from the trap

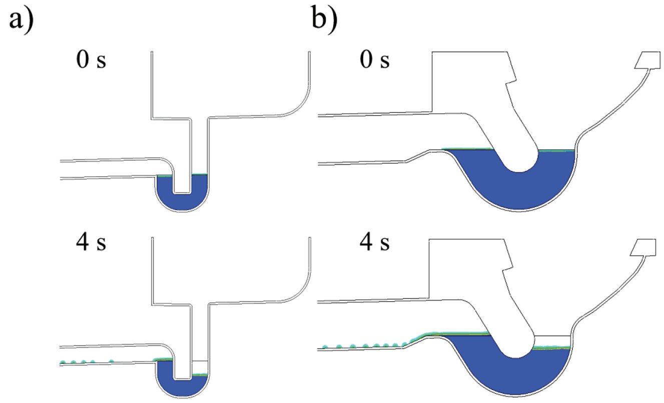

Fig. 8 *Minimal water drop in the trap, without compromising its functioning, p_n ≤ 300 Pa*
a) basin or sink, b) WC

There was more water suction from the trap and a negative pressure from 300 to 450 Pa, but the functioning of the trap was not compromised. The maximum recorded water drop in the trap was 25 mm (Fig. 9). Considering issues of safety and costs, assessing stacks to a negative pressure $p_n \leq 450$ Pa is an economical solution and is still relatively safe.

At a negative pressure from 450 to 475 Pa (sink, basin) and a negative pressure from 450 to 525 Pa (WC), water was sucked out of the trap, and the functioning of the trap was compromised. The maximum recorded drop in water in the trap was 35 mm, but air from the interior began to be sucked into the branch pipe (Fig. 10). This would be accompanied by unpleasant noises that would affect the comfort of a building's users. Assessing stacks at these negative pressures is not recommended.

At negative pressures of p_n > 475 Pa (sink, basin) and p_n > 525 Pa (WC), the water was completely sucked out of the trap; the trap ceased to function (Fig. 11). This process would undoubtedly be accompanied by the dissemination of annoying smells from the drainage system to the building interior. The WC was able to withstand higher negative pressure due to the sloping shape of the trap, which was able to draw in more significant amounts of air from the interior, p_n > 450 Pa. Assessing stacks at these negative pressures is not recommended.

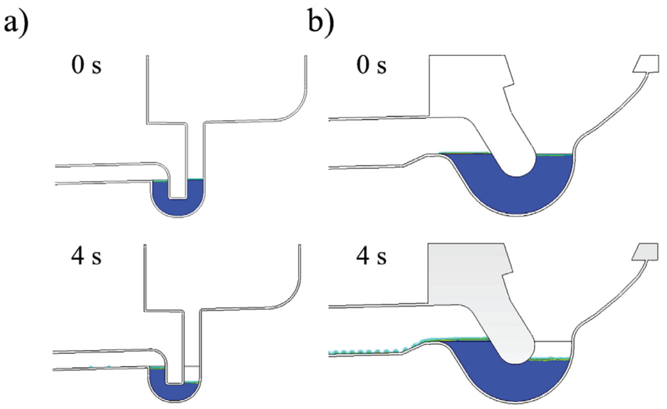

Fig. 9 *Drop in water in odor trap up to 25 mm, without compromising functioning, pn ≤ 450 Pa*
a) basin or sink, b) WC

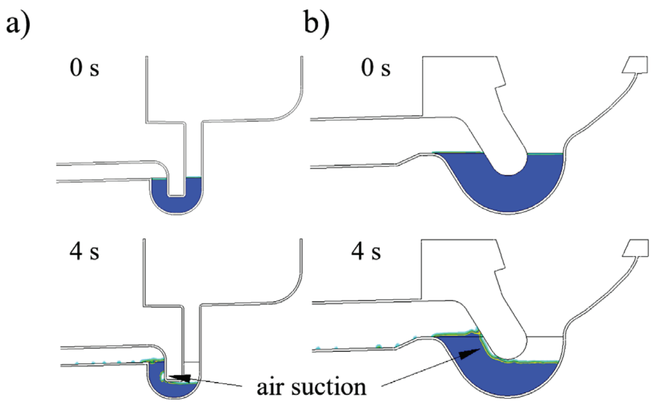

Fig. 10 *Intake of air from the interior, compromising the function of the trap*
a) basin or sink 450 < p_n ≤ 475 Pa, b) WC 450 < p_n ≤ 525 Pa

Tab. 2 *Effect of negative pressure on the water level in the WC trap*

Negative pressure p_n (Pa)	Effect on the water level
≤ 300	without compromising its functioning, drop in water minimal
300 to 450	without compromising its functioning, drop in water up to 25 mm
450 to 525	compromising its function, drop in water up to 35 mm, suctioning of air from the interior
> 525	loss of functioning, complete suction of water from the trap

Based on the simulation of the effect of negative pressure on the water level in the traps, it can be concluded that it is safest to assess the stacks for a negative pressure $p_n \leq 300$ Pa. After considering the costs and safety, it is acceptable to design stacks for a negative pressure $p_n \leq 450$ Pa.

5.3 Simulation of the effect of overpressure on the water level in the trap

The traps from Figs. 4a, c were tested for overpressures ranging from 0 to 1500 Pa. The high overpressure range was chosen based on experimental measurements from outside of Slovakia when the overpressure of 1500 Pa was measured. The overpressure was measured at the incorrectly chosen technical solution of the stack offset in a 9 – story building (Yabe et al., 2015). The above-mentioned water level conditions were observed in the trap, section 4. The best results in this test were achieved by the toilet trap that could withstand an overpressure p_o = 875 Pa without any loss of functioning. The trap for the basin and sink withstood an overpressure p_o = 725 Pa. The detailed simulation results are shown in Tables 3 and 4.

From a safety point of view, an overpressure of $p_o \leq 725$ Pa (sink, basin) and $p_o \leq 875$ Pa (WC) runs the lowest risk of the water bubbling or the ejection of water from the sanitary appliance. At these values, the water level in the trap only fluctuates, without any undesirable processes occurring (Fig. 12).

At an overpressure from 725 to 1025 Pa (sink, basin) and an overpressure from 875 to 1025 Pa (WC), there was water bubbling in the trap (Fig. 13). Due to the slanted shape of the trap, the toilet was able to overcome higher overpressure values, which caused more water to bubble. This process would be accompanied by the dissemination of annoying smells from the drainage system, which would bubble up into the interior of the building. Among other things, bubbling water would compromise the comfort of the building's users.

At an overpressure p_o > 1025 Pa, water was wholly ejected from the sanitary appliances. In addition to the spread of annoying smells, the surrounding areas and the comfort of the building's users would be degraded by the water from the traps (Fig. 14).

The problems with the high overpressure values cannot be solved by the correct design of the stack's dimensions. A properly resolved change in the direction of the stack can cause overpressures above 1000 Pa in the case of an incorrect design. Nowadays, there are various accessories for stacks, including positive pressure attenuators, which can sufficiently eliminate such high values generated (While and Hill, 2015).

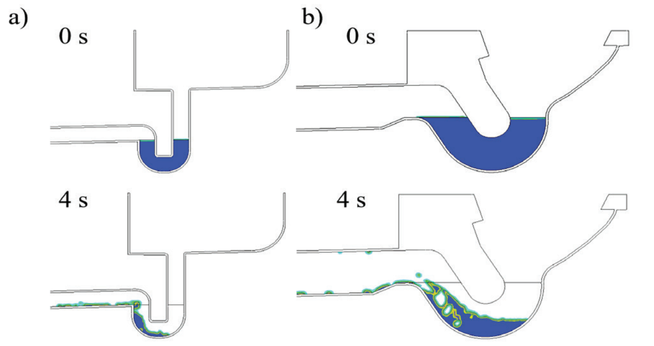

Fig. 11 *Complete suctioning of the water seal, loss of the functioning of the trap*
a) basin or sink p_n > 475 Pa, b) WC p_n > 525 Pa

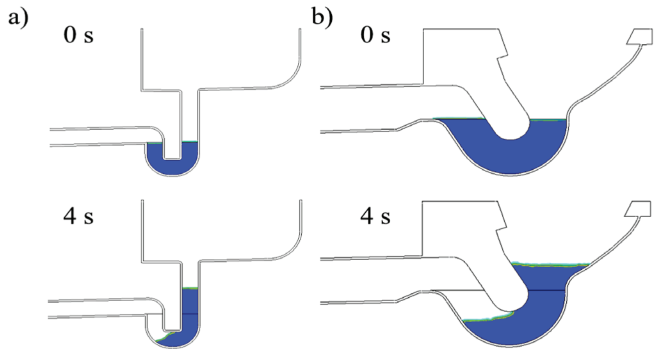

Fig. 12 *Fluctuations of the water level in the trap, without compromising any functioning*
a) basin or sink p_o < 725 Pa, b) WC p_o < 875 Pa

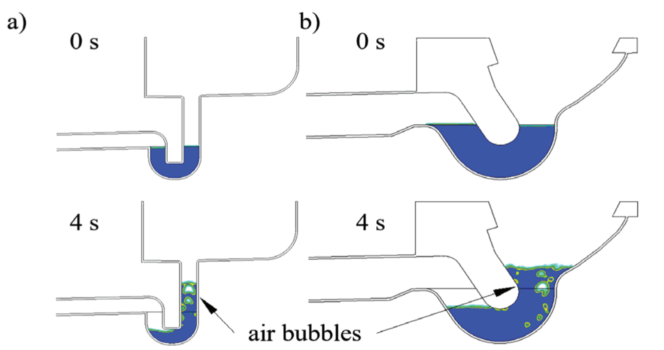

Fig. 13 *Bubbling water in the trap, loss of function*
a) basin or sink 725 < $p_o \leq$ 1025 Pa, b) WC 875 < $p_o \leq$ 1025 Pa

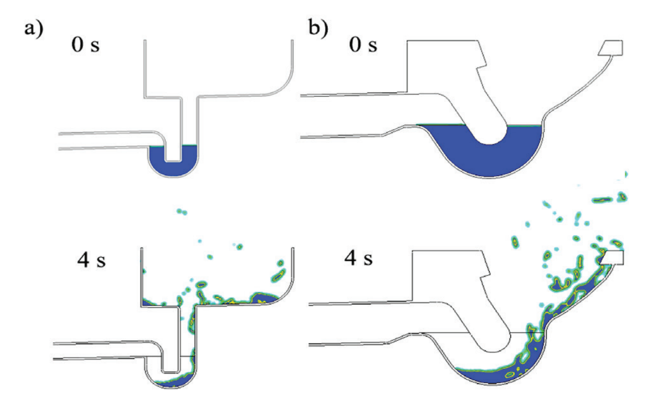

Fig. 14 *Complete ejection of water from sanitary appliances, loss of functioning*
a) basin or sink po > 1025, b) WC po > 1025

Tab. 3 *Effect of overpressure on the water level in the sink or basin trap*

Overpressure p_o (Pa)	Effect on the water level
≤ 725	without compromising functioning, water level fluctuations
725 to 1025	loss of function, water bubbling
> 1025	loss of function, complete ejection of water

Tab. 4 *Effect of overpressure on the water level in the WC trap*

Overpressure p_o (Pa)	Effect on the water level
≤ 875	without compromising functioning, water level fluctuations
875 to 1025	loss of function, water bubbling
> 1025	loss of function, complete ejection of water

5.4 Simulation of the effect of evaporation on the pressure resistance of the trap

To assess the effect of evaporation on the pressure resistance of the trap fittings 2, which are shown in Figs. 5a, b, were used. The first trap contained the following 3 water levels:

- 50 mm – the water level in the trap immediately after use of the sanitary appliance, Fig. 15a,
- 43 mm - the water level in the trap after 14 days of not using the sanitary appliance, Fig. 15b,
- 25 mm - the water level in the trap after 50 days of non-use of the sanitary appliance, Fig. 15c.

The second trap was experimentally adjusted so that the maximum water level in the trap immediately after use of the sanitary appliance was 43 mm (Fig. 15d). The negative pressure p_n = 475 Pa was generated in the stack, to which both traps were simulated. The negative pressure was chosen based on section 4.2; it represents the limiting value for a sink or basin trap with a 50 mm water seal.

The first trap to be simulated for negative pressure, i.e., p_n = 475 Pa was the one with a 50 mm water level, which was full of water. The functioning of the trap was not impaired, and approximately 26 mm of water remained in the trap after the pressure settled (Fig. 16a).

The same trap was used in the second simulation, but 7 mm of the water evaporated. The total height of the water in the trap was 43 mm. The functioning of the trap was not impaired, and approximately 27.5 mm of the water remained in the trap after the pressure settled (Fig. 16b).

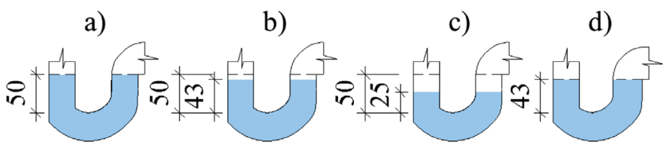

Fig. 15 *Simulated water heights in the trap*
a) 50 mm trap, b) 50 mm trap after 2 weeks of non-use, c) 50 mm trap after 50 days of non-use, d) 43 mm trap

The same trap was also used in the third simulation, but 25 mm of the water evaporated. The total height of the water in the trap was 25.0 mm. The functioning of the trap was not impaired, and approximately 24.5 mm of water remained in the trap after the pressure settled (Fig. 16c). In the fourth test, the trap was experimentally adjusted so that the height of the water level was

43 mm. The trap was full of water. Based on Formula (2), this trap should have the same pressure resistance as the trap from the second test. The water from the trap was sucked out so that an annoying smell would probably spread in the building (Fig. 16d).

Based on the simulation, it can be concluded that the pressure resistance of the trap is not affected by the evaporation of the water. The important factor is the height of the water seal (shape) in the trap and not the remaining height of the water level. Water evaporation is the trap's only threat, provided that less than 7 mm of water remains after the water has been sucked out. This remaining water could evaporate within 2 weeks of not using the sanitary appliance, and the trap would cease functioning.

6 SUMMARY OF RESULTS

Based on the simulation of the effect of pressure on the water in a trap, it can be stated that:

- the safest solution is to assess the stacks for a negative pressure of $p_n \leq 300$ Pa, which has a minimal effect on the water level in the trap,
- after taking into account the costs and safety, it is acceptable to design stacks for a negative pressure of $p_n \leq 450$ Pa when there is a drop in the water in the trap, which does not endanger its functioning,
- at a negative pressure of $p_n > 450$ Pa, the functioning of traps is compromised due to the suctioning of air from the interior; and when $p_n > 475$ Pa, the functioning of the trap ceases due to the suctioning of the water seal,
- when the overpressure of $p_o > 725$ Pa, water bubbles in traps, which leads to the spread of annoying smells in the building,
- when the overpressure of $p_o > 1025$ Pa, the water is ejected from sanitary appliances,
- the shape of a trap affects its pressure resistance,
- the evaporation of water from traps does not affect their pressure resistance, but the height of the shape of the water seal is particularly important.

7 CONCLUSION

The correct design of foul water stacks has a very important role, especially in high-rise buildings. To avoid undesirable effects that may arise when water is sucked or ejected from the traps, it is necessary to assess them for the correct limit values. The most important part of assessing stacks is assessing the maximum negative pressure because the overpressure can only be influenced by the correct design of the stack offset. Consideration must be given to direct vent stacks, which may exceed the maximum negative pressure if adequately designed according to the standards. Based on the simulation and as-

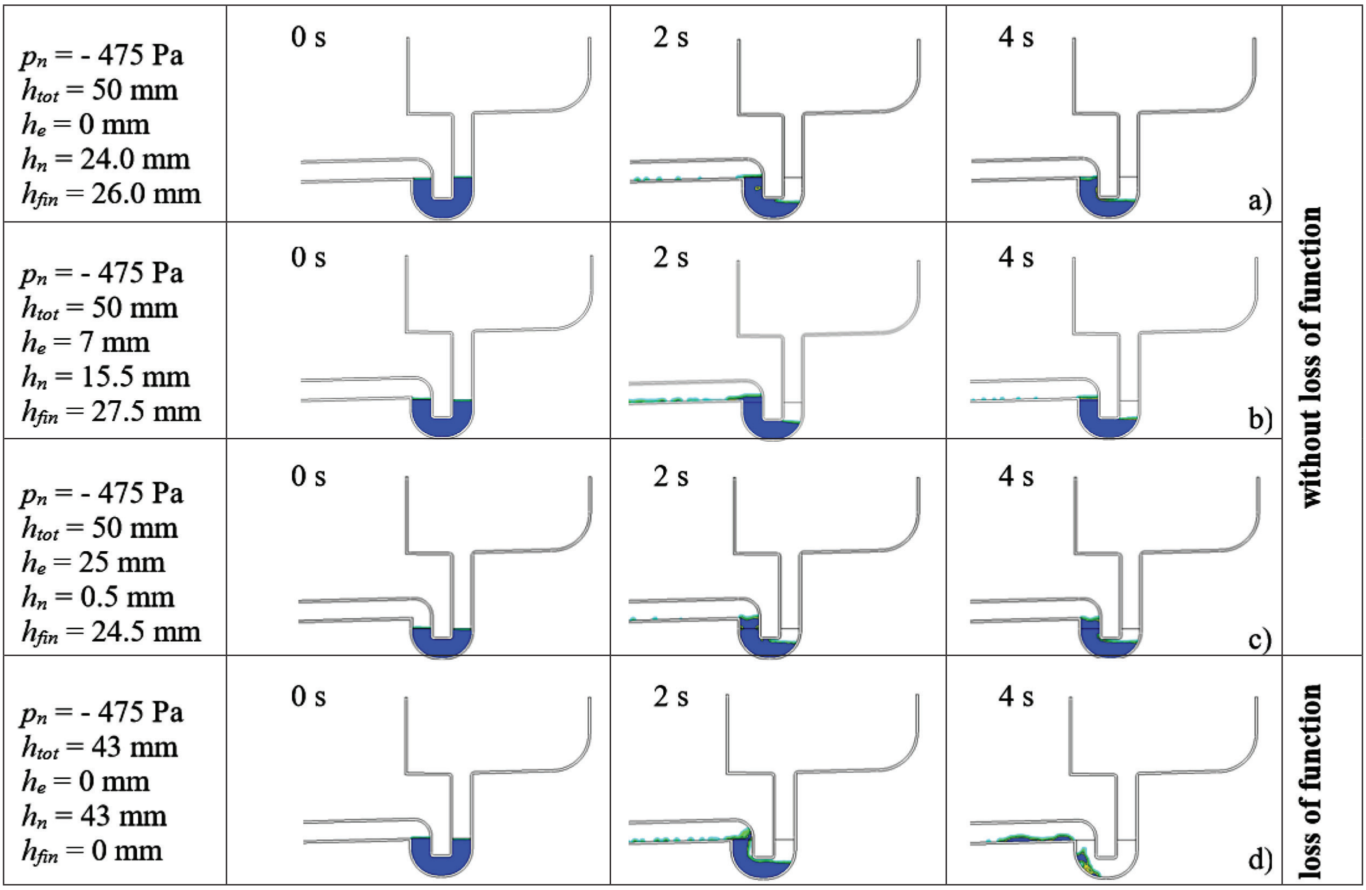

Fig. 16 *Assessment of the effect of evaporation on the pressure resistance of the trap*
p_n – negative pressure, h_{tot} – the total water level in the trap, h_e – drop in the water level in the trap due to evaporation, h_n – drop in the water level in the trap due to negative pressure, h_{fin} – final water level in the trap

suming a 50 mm high water seal, a safe and economical route is represented by assessing the stacks at a negative pressure of $p_n \leq 450$ Pa. Assessing stacks for a negative pressure of $p_n \leq 300$ Pa is a very safe solution but uneconomical. Very complicated stacks should be assessed for such a negative pressure value. Evaporation of water from the odor trap does not need to be taken into account because the height of the shape of the odor trap is important. Regardless of the height of the foul water stack, the offset or transition to the drain must be resolved correctly. At an overpressure of $p_o > 725$ Pa the function of the trap is compromised, such an overpressure value can already occur in a 9-storey building.

Acknowledgments

This work was supported by the Ministry of Education, Science, Research, and Sports of the Slovak Republic through the Scientific Grant Agency VEGA 1/0303/21 and KEGA no.005STU-4/2021.

REFERENCES

Cheng, L. – Ho, C. – Lu, H. (2004) *Current Design of High-Rise Building Drainage System in Taiwan.* CIB W062 Symposium pp. 329 - 345. Available at: https://www.irbnet.de/daten/iconda/CIB10515.pdf (accessed at 12/04/2022).

Dobromyslov, A. (1978) *Rasčet i konstruirovanije system kanalizacii zdanij (Calculation and construction drainage in buldings)*. 1st ed., Strojizda, Moscow.

Heinrichs, F. – Rickmann, B. – Sondergeld, K. – Störrlein, K. (2010) *Kommentar zum DIN 1986-100 and EN 12056-4. Gebäude und Grund stucksentwässerung (Comment on DIN 1968-100 and EN 12056-4. Drainage of buildings).* DIN Deutsches Institut für Normung, pp. 126–127 ISBN 978-3-410-20533-3.

Hung, H. C. – Chan, D. W. – Law, L. K. – Chan, E. H. – Wong, E. S. (2006) *Industrial Experience and Research into the Causes of SARS Virus Transmission in a High-Rise Residential Housing Estate in Hong Kong.* In: Building Serv. Eng. Res. Tech. 27 (2), 91–102. https://doi.org/10.1191/0143624406bt145oa

Gormley, M. – Kelly, D. – Campbell, D. – Xue, Y. – Stewart, C. (2021) *Building Drainage System Design for Tall Buildings: Current Limitations and Public Health Implications.* In: Buildings, 11 (2). https://doi.org/10.3390/buildings11020070

Gormley, M. – Aspray, T. – Kelly, D. (2020) *COVID-19: mitigating transmission via wastewater plumbing systems.* In: Water Management 173 (6), pp. 271–273. https://doi.org/10.1016/S2214-109X(20)30112-1

Öngören, A. – Materna, R. – Tanner, M. (2005) *Investigation of the effect of swept entry configuration on the air entertainment and self-siphoning behavior in gravity drainage systems.* CIB W062 Symposium pp. 160 - 170. Available at: https://www.irbnet.de/daten/iconda/CIB12091.pdf, (accessed at 12/04/2022).

Öngören, A. – Weiss, R. (2018) *Principles of a genuine high flow wastewater fitting with an in-pipe integrated ventilation.* CIB W062 Symposium 2018 pp. 17 - 24. Available at: https://www.irbnet.de/daten/iconda/CIB_DC32021.pdf, (accessed at 12/04/2022)

Pomogaeva, V. – Matechko, L. – Prokofiev, D. – Narezhnaya, T. (2018) *Investigation of the motion processes of wastewater in sewerage of high-rise buildings.* E3S Web of Conferences pp. 1 – 9. https://doi.org/10.1051/e3sconf/20183302013

Peráčková, J. (2018) *Dimenzovanie splaškových odpadových potrubí (Design of foul water stacks).* TZBinfo. Available at: https://voda.tzb-info.cz/kanalizace-splaskova/17916-dimenzovanie-splaskovych-odpadovych-potrubi, (accessed at 12/04/2022).

Scheutz, F. – Strockbine, N. A. (2015) *Escherichia.* In: Bergey's Manual of Systematics in Archaea and Bacteria. Eds. M. E. Trujillo, P. Dedysh, B. DeVos, B. Hedlund, P. Kampfer, F. A. Rainey et al. (Hoboken, NJ: John Wiley & Sons, Inc.). https://doi.org/10.1002/9781118960608.gbm01147

Valášek, J. (1986) *Vnútorná kanalizácia. Komentár k ČSN 73 6760. Dimenzovanie potrubia vnútornej kanalizácie (Design of drainage pipes)*. Vydavatelství úradů pro normalizaci a měření, Bratislava, SK, pp. 21-30 ISBN 59-313-83.

Valášek, J. (1982) *Vodovody a kanalizácia vo vysokých budovách, (Water supply and drainage in high-rise buildings)*. Bratislava: Alfa, Slovakia, pp. 131-157 ISBN 63-021-82.

Valášek, J. – Peráčková, J. – Žabička, Z. – Kabele, K. – Beňo, S. (2005) *Zdravotnotechnické zariadenia budov (Sanitary installations).* Bratislava: Jaga group, SK, pp. 317-319 ISBN 80-8076-013-6.

Vrána, J. (2021) *Větrání vnitřní kanalizace (Ventilation of drainage*). TZBinfo. Available at: https://voda.tzb-info.cz/kanalizace-splaskova/21769-vetrani-vnitrni-kanalizace (accessed at 12/04/2022).

While, S. – Hill, T. (2015) *High-rise Testing of Active Drainage System Compared with Conventional Venting on Two Test Towers.* CIB W062 Symposium pp. 11 - 29. Available at: https://www.irbnet.de/daten/iconda/CIB_DC30620.pdf (accessed at 12/04/2022).

Zheng, S. – Fan, J. – Yu, F. – Feng, B. – Lou, B. – Zou, Q., et al. (2020) *Viral Load Dynamics and Disease Severity in Patients Infected with SARS-CoV-2 in Zhejiang Province, China, Jan-Mar 2020: Retrospective Cohort Study.* In: BMJ 369, m1443. https://doi.org/10.1136/bmj.m1443

Yabe, S. – Otsuka, M. – Kawaguchi, T. – Sugimoto, R. (2015) *An Experimental Investigation of the Influence of Different Offset Piping Methods on the Drainage Performance of a Drainage Stack.* CIB W062 Symposium pp. 30 - 55. Available at: https://www.irbnet.de/daten/iconda/CIB_DC30620.pdf (accessed at 12/04/2022).

STUDOR (2022) *Company documents*. Available at: https://studor.net/en/page/ (accessed at 12/04/2022).

STN EN 12056. (2002) *Gravity drainage systems inside buildings*.

STN 73 6760. (2009) *Kanalizácia v budovách (Drainage inside buildings)*.

TNI CEN/TR 17426. (2019) *Sanitary appliances – Drainage systems for the application of sanitary appliances.*

Ansys. (2009) User Fluent 12.0 guide. Ansys. Available at: https://www.afs.enea.it/project/neptunius/docs/fluent/html/ug/main_pre.htm (accessed at 12/04/2022).

sciendo **Slovak Journal of Civil Engineering**

Vol. 30, 2022, No. 4, 39 –48
DOI: 10.2478/sjce-2022-0027

PHYSICAL-MECHANICAL PROPERTIES OF WATERPROOFING MATERIALS APPLIED TO ROOFS IN THE CONTEXT OF UV DEGRADATION

Jozef KOVÁČ[1*] Milan Palko[1] Angela Kleinová[2]

Abstract

The subject of the article is a physical-mechanical analysis of waterproofing materials exposed to an external environment. Physical and mechanical properties have a direct impact on the life of waterproofing materials and their later remediation. In the introduction, the factors influencing the properties of waterproofing materials are presented. The main part of the article covers the basic possibilities of testing the materials testing the materials, normative testing conditions, and critical aspects of their implementation. In this article we deal with the laboratory testing of a waterproofing membrane based on PVC-P in terms of its degradation from UV radiation, humidity, and the temperature.

Address

[1] Dept. of Building Construction, Slovak University of Technology in Bratislava, Slovakia

[2] Polymer Institute, Slovak Academy of Science in Bratislava, Slovakia

* ***Corresponding author:*** jozef.kovac@stuba.sk

Key words

- PVC-P,
- UV degradation,
- Humidity,
- Testing.

1 INTRODUCTION

One of the largest developments in plastics has occurred in the construction industry. Polymer products are widely used in construction to produce window profiles and thermal and noise insulation but are mostly used to produce waterproofing. As plastics in construction are not renewable, they must have a long service life and retain their properties. In the waterproofing industry, polymers appear in the form of films and are part of other sealants and coatings. However, it must not be forgotten that polymeric materials also degrade. Many of them release low molecular weight compounds during degradation processes, which can be harmful to health or endanger the environment due to their toxicity. It is therefore important to know the properties of plastics in different degradation environments, including whether they are undergoing a substantial change to thereby prevent the accumulation of plastic waste and protect the environment.

2 CLIMATIC FACTORS INFLUENCING THE SERVICE LIFE OF A ROOF STRUCTURE

The territory of the Slovak Republic lies in a temperate climate zone and is affected by polar and tropical climates. None of these influences prevail in our environment, so our climatic conditions are the result of alternating external influences. Roofing materials that are exposed to their external environment for a long time, especially sunlight, changes in temperature, rain, wind, snow, and air pollution, are degraded and lose their physical and mechanical properties. Even the most weather resistant materials are modified by the deposition of surrounding dust and debris, which can provide an opportunity for colonization of biological organisms such as mushrooms, algae, etc.

Solar radiation

Solar radiation can be divided into two parts: direct solar radiation and scattered solar radiation (diffuse). The solar spectrum is usually divided into three main parts, and we can accordingly distinguish ultraviolet radiation, visible solar radiation, and infrared solar radiation.

As a result of the absorption of light energy, chemicals are degraded, including degradation in polymers, due to various types of photochemical reactions. Polymers are most affected by solar radiation with a wavelength of 290-400 nm, which accounts for about 5% of the total solar radiation incident on the Earth’s surface. The extent of solar radiation depends on atmospheric pollution, the altitude, and the time of year or day (Mleziva, 2000).

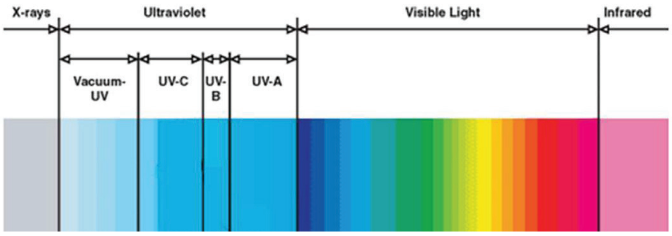

Fig. 1 *The spectrum of solar radiation*

The temperature and various changes

Rising temperatures due to solar radiation can directly lead to the degradation of materials. Elevated temperatures can accelerate harmful chemical reactions, result in the loss of volatile components, and soften some polymers. Changes in the temperature can be gradual or sudden (rain during a hot day), causing stress due to differential thermal expansion (Berdahl, 2006). Fluctuations in temperatures also contribute to degradation, causing dimensional changes that can result in internal stress and subsequent cracking. This type of disruption diffuses oxygen and ozone into the polymer, leading to accelerated degradation. At higher temperatures, it can lead to the migration of additives, especially plasticizers, stabilizers, etc. As a result, the polymers harden, and the mechanical properties are lost.

Humidity

Factors causing moisture on a surface in constructions are, e.g., rain, hail, snow, frost, and dew. In the case of surface damage due to external influences (e.g., UV radiation), moisture has negative effects on the waterproofing layer and helps to degrade the polymers. Its effect is to wash away catalysts, antioxidants, and light stabilizers. If water enters the polymer, it can cause swelling or act as a plasticizer. Polymers that contain oxidizable groups are most susceptible to water. If these groups are in the main chain, there is a significant reduction in molecular weight and a loss of strength (Mleziva, 2000).

Atmospheric gases and pollutants

Nitrogen, which forms most of the atmosphere (78 % by volume) is not very chemically reactive, but its reaction with oxygen (21 %) and steam (0.3-3 %) can cause the formation of various oxides and hydroxides. For example, iron corrosion products include FeO, Fe_2O_3, Fe_3O_4 and FeOOH. Some other important atmospheric components include oxides of carbon, sulfur, and nitrogen such as CO_2, SO_2 and NO_2, which are formed by combustion. When these gases are dissolved in water, acids are formed. These acids can promote corrosive chemical reactions. Another pollutant is carbon black, which is a strong absorber of sunlight. The presence of soot on a roof causes a change in the color of the surface layer (darkens) and thus leads to an undesirable increase in the temperature of the coating (Berdahl, 2006).

3 MATERIAL TESTING

When analyzing the basic physical characteristics in connection with ambient temperatures and UV degradation. UV degradation is one of the most important factors influencing the mechanical properties of materials such as reduced tensile strength, impact resistance, brittleness, and tensile cracking.

3.1 Natural testing

There are several exposure points around the world, each with a different climate, which can be used to predict the external life of materials. The selected site should be the one that is most representative of a general interest environment, but it is more common to select places with extreme climates and compare the resulting degradation with the degradation that occurs in the implementation environment. In this way, “natural” exposure is achieved, although UV, temperature and humidity levels may differ significantly from the levels that would be met during an operation. Among the most famous sites are e.g., Miami, Florida; Arizona; and the Hook of Holland in The Netherlands.

3.2 Accelerated external testing

Weather conditions can be further accelerated by a more efficient use of outdoor exposure. An example of this is the widespread use of Equatorial Mount with Mirrors for Acceleration (EMMA) and Equatorial Mount with Mirrors for Acceleration with Water (EMMAQUA) devices. These instruments have ten highly polished moving aluminum mirrors that amplify the sun’s rays focusing on the test specimen. The system achieves approximately nine times the exposure compared to a natural one; the observed rate of deterioration is on average 5-6 times faster. This is because aluminum mirrors reflect less harmful UV components of sunlight. Due to the high intensi-


Fig. 2 *Testing farm (left) EMMA (right) (Atlas, 2001)*

ty of radiation focused on the sample, temperatures of up to 150 °C can develop on the surface of the sample; air cooling must therefore be used (Johnson, 1996).

3.3 Laboratory testing

The main reason for using artificial weather methods is to accelerate degradation under controlled conditions so that the durability characteristics of a particular polymer can be evaluated in an acceptably rapid time. Laboratory tests may be continuously performed, with a naturally higher occurring irradiance than solar radiation, which does not interrupt the natural day, e.g., night cycles, seasonal changes, and weather conditions. Temperatures, temperature cycles, humidity, and total sun exposure can be manipulated to their maximum, which can lead to unrealistic levels at which adverse photochemical events could occur that would not occur with natural exposure. Therefore, it is necessary to consider these factors so that all the degradation processes affect the samples to the same extent. There are many commercial artificial acceleration techniques that are usually based on the same two or three light sources (Tochacek, 2014).

Light sources

Carbon arc sources were first used in 1918 to evaluate the degradation of colored textiles. Their spectral output is small in comparison with natural solar radiation, with the main radiation taking the form of three high-intensity peaks between 350-450 nm. In addition, they have a significant amount of radiation below 295 nm, although that can be removed using suitable filters. When used without filters for faster testing, some materials may be deformed compared to external tests.

Xenon arc sources were first used in 1954 (Xenotest 150). The xenon arc reproduces the entire spectrum of solar radiation. As a light source, it is widely used for degradation testing in the textile, polymer, paint, and automotive industries. The disadvantages of the xenon arc are that a high intensity of infrared radiation is generated, which must be removed to prevent the samples from overheating, and that both burners and filters deteriorate during use; therefore, their performance must be regularly checked. There are two types of cooling systems, i.e., water and air-cooled xenon lamps; this type of cooling has only a negligible effect on the spectral output of the lamps. In addition to narrow simulations of the solar spectrum, other advantages of the xenon arc include automatic control of the intensity of the light, temperature, light / dark time, and humidity, leading to a consistent and reproducible test method. In addition, the incorporation of atmospheric pollutants into the system makes these tools very useful in linking the behavior of materials to aggressive environmental factors (Johnson, 1996), (Tochacek, 2015).

Fluorescent sources are much cheaper than xenon sources and have the advantage of not generating unwanted heat. Lamps are available with various spectral outputs, the most common being UV-B and UV-A fluorescent lamps. The UV-B spectrum has a peak intensity at a wavelength of approximately 313 nm with a high intensity at wavelengths below the solar edge (i.e., 270 to 290 nm). As a result, they provide a strong acceleration of degradation, but cause undesirable or unnatural chemical reactions. UV-A bulbs provide a much closer reproduction of the solar spectrum up to about 350 nm and can therefore produce a much more accurate correlation with natural exposure. Since these sources of radiation have only a negligible thermal effect, a separate heat source is needed, which provides the user with an adequate temperature control. Thanks to these systems, it is possible to control the temperature, humidity, and light / dark cycles (Johnson, 1996), (Tochacek, 2015).

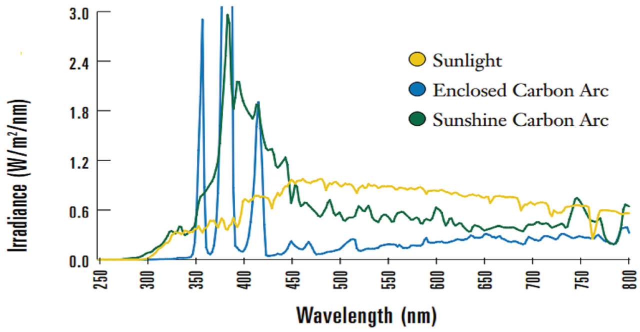

Fig. 3 *Spectral distribution of carbon arc radiation compared to solar radiation (Atlas, 2001)*

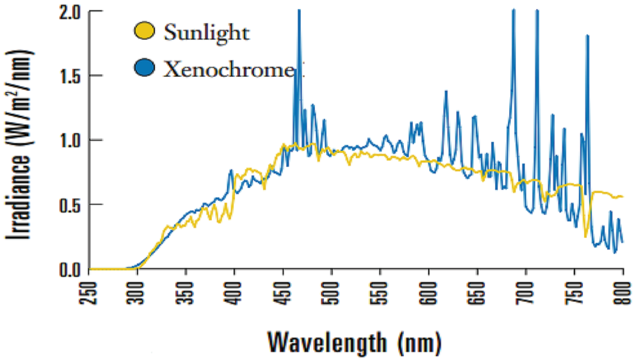

Fig. 4 *Spectral distribution of xenon arc radiation compared to solar radiation (Atlas, 2001)*

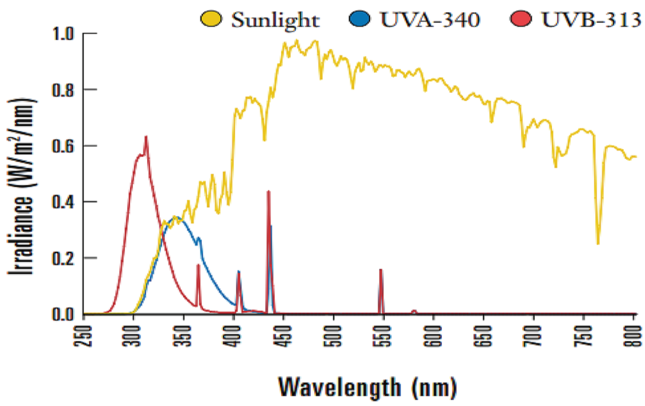

Fig. 5 *Spectral distribution of two types of fluorescent sources with a maximum at 313 vs. 340 nm compared to solar radiation (Atlas, 2001).*

4 TESTING OF PVC-P MATERIALS IN TERMS OF UV RADIATION AND HUMIDITY

4.1 Laboratory equipment for experimental measurements

Our testing mostly took place in the Laboratory for Roof Research at the Faculty of Civil Engineering of the Slovak

Fig. 6 *Manual hydraulic press (left), steel punch (right)*

University of Technology in Bratislava. The laboratory has devices for appropriate measurement of the basic characteristics of materials (weight, dimensions), devices simulating external conditions, and a device for determining the mechanical resistance of materials. An additional chemical analysis of the sample surface was performed in cooperation with Ing. Angela Kleinová and Mgr. Mária Kováčová, PhD., at the Institute of Polymers of the Slovak Academy of Sciences in Bratislava.

The following devices were used:

A) KERN PLJ 600-3CM digital laboratory scales

These scales are accurate digital laboratory balances with internal calibration and an automatic adjustment, which takes place every 3 hours or when the ambient temperature changes by 3 °C and with a weighing capacity of 600 g and a sensitivity of 0.001 g. We used a laboratory scale that continuously weighed the samples to evaluate the weight loss of the material tested.

B) Digital caliper

A digital caliper was designed for measuring dimensions with a maximum range of up to 300 mm. The sensitivity / tolerance of the device is 0.02 mm

C) 12 t manual workshop hydraulic press and steel punch

A Dema WP 12H hydraulic-pneumatic press with a working pressure of 12t, which was designed for compression and pressing, was used. The frame is reinforced and provides resistance to mechanical damage. The press comes with a set of pressure attachments for distribution of the weight on the printed element. The press was used to cut samples for the strength test.

The steel punch is designed for cutting samples for strength (tear) tests. It was made based on processed drawing documentation. The shape and dimensions are defined in STN EN 12311-2 as a dumbbell-shaped test specimen for method B.

D) Test machine M500-25CT - 20kN

The M500-25CT is a two-column, computer-controlled universal testing machine table for testing materials in tension, pressure, bending, cyclical stress, shear, and hardness. The

Fig. 7 *Test machine - M500-25 CT*

machine can test the mechanical properties of building materials and their joints at negative and positive temperatures (from + 70 °C to 280 °C). The machine is controlled using winTest ™ Analysis software.

E) QUV/spray

The QUV accelerated weather test device is used for the laboratory simulation of the harmful effects of weather conditions. It is used to predict the relative resistance of material exposed to an outdoor environment. Rain and dew are simulated using a condensation system or a water spray system. The harmful effects of sunlight are simulated by fluorescent UV lamps. The irradiation temperature and the daily sequence of UV periods and humidity periods are automati-

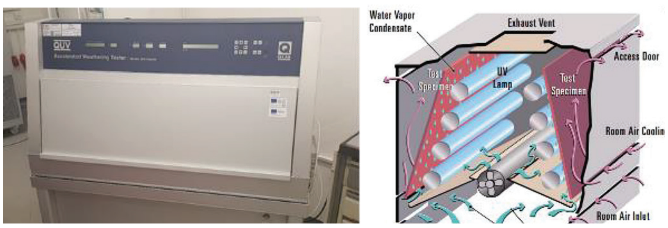

Fig. 8 *QUV/spray (left) condensation cycle for fluorescent UV devices (right)*

Fig. 9 *Nicolet 8700TM FT-IR spectrometer (left), Leica DVM6 microscope (right)*

cally controlled. Over a few days or weeks, the QUV device can damage the samples to an extent that would not show up in outdoor conditions for several months or years. The damage observed includes color fading, staining, cracking, cracking, bulging, loss of gloss, loss of strength, and embrittlement (Labimex, 2008).

F) NICOLET 8700TM infrared spectrometer

FTIR spectroscopy is used to determine the content of various organic and inorganic substances and their compounds in solid, liquid, and gaseous samples (food, soil, metals and their alloys, polymers, etc.) on the absorption spectra. The principle of the device is that the movement of one of the interferometer mirrors causes a change in the path between the interfering rays. The recorded luminous flux at the output of the interferometer (interferogram) is the Fourier transform of the detected optical spectrum, i.e., the natural spectrum (in the range of wave numbers) obtained after performing the inverse Fourier transform.

G) Leica DVM6 digital microscope

A Leica DVM6 digital microscope with a PlanAPO FOV 12.55 objective with a large magnification range (40x – 675x) at a high working distance (33 mm) was used. It has rapid magnification changes, thanks to a wide focal length range of 16: 1 and a highly sensitive 10-megapixel detector shooting in the best quality with first-class optics. A LAS X intelligent software measuring tool was used for various settings with the possibility of reporting for 2D and 3D measurements.

4.2 Laboratory testing

4.2.1 Samples

The aim was to obtain materials with similar properties, such as their thickness and its use in construction practice. The samples obtained from different manufacturers are as follows:

- Sample No. 1 (V1) – PVC-P – polyester-reinforced foil, 1.5 mm thickness
- Sample No. 2 (V2) – PVC-P – polyester-reinforced foil, 1.5 mm thickness
- Sample No. 3 (V3) – PVC-P – foil without reinforcing grid, 2.0 mm thickness
- Sample No. 4 (V4) – PVC-P – polyester-reinforced foil, 1.5 mm thickness

Sample No. 3 is a PVC-P waterproofing coating without a reinforcing grid; from our point of view, it is also necessary to deal with this type of waterproofing film, which is mainly used for processing details. Unfortunately, it was not possible to obtain it from other manufacturers to compare the film in the same way as it was in the case of the PVC- P with a reinforcing grid. Even so, the choice of this type of PVC-P was correct because it gave us a closer look at what its mechanical properties are compared to PVC-P with a reinforcing grid. In this case, the correctness of the methodology was defined by using material without a reinforcing grid. In this case, it is also important to determine the weight loss, i.e., the loss of the plasticizer itself, which has a direct impact on the dimensional stability of the material.

4.2.2 Preparation for the experimental measurement of UV degradation in the QUV

To carry out the experiment, it was necessary to prepare samples of the required dimensions for placement in the test apparatus. The device contains 24 frames, in each frame of which it is possible to place 2 samples with a maximum size of 75 mm x 150 mm. In the beginning, 12 samples (a total of 48 pieces) were prepared from each material. During the testing, the samples were selected and then replaced with new ones to obtain the required number of samples to perform the strength test. Before the start of the experiment, the weight of each sample was determined, and the average weight loss was monitored.

Degradation testing was performed under laboratory conditions according to the standard STN EN ISO 4892-3: Plastics - Methods of exposure to laboratory light sources. Part 3: Fluorescent UV lamps. Method A was chosen from Table No. 4 exposure cycles: Accelerated laboratory aging with UVA 340 type fluorescent lamps and selected cycle No. 2. The cycle corresponds to the standard testing of polymer products. Testing took place in a QUV device. Prior to start-up, the QUV / spray instrument was calibrated using a portable calibrator. The calibration process was performed every 1000 hours.

Tab. 1 *Exposure cycles from STN EN ISO 4892-3 – Table No. 4*

Method A: Artificial accelerated weathering with UVA-340 lamps				
Cycle No.	**Exposure period**	**Lamp type**	**Irradiance**	**Black-panel temperature**
2	8 h dry 0,25 h water spray 3,75 h condensation	UVA-340 (type 1A)	0,76 $Wm^{-2} \times nm^{-1}$ at 340nm UV lamps off UV lamps off	50 °C ± 3 °C Not controlled 50 °C ± 3 °C

Evaluation of UV degradation results

The quality of roofing is evaluated according to the following European standards and documents:

- EN 13956: 2013 - Waterproofing membranes and sheets - Plastic and rubber membranes and sheets for roof waterproofing - Definitions and characteristics
- EAD 030351-00-0402 - System of mechanically anchored flexible roof waterproofing coatings (from 29.5.2019 "ETAG 006"),
- MOAT 65 - UEAtc Technical Manual for the evaluation of PVC roof waterproofing systems.

Each of these documents evaluates the appropriate quality of all the properties that the waterproofing foil should meet. Before placing it on the market, the film is required to meet the requirements of the test standard EN 13956, where the criteria are not entirely sufficient concerning the expected service life. Some of the manufacturers use to include the information in their technical data sheet that their material had been tested for UV degradation for up to 5000 hours. For this reason, a procedure was chosen that compares UV degradation and then a strength test every 1000 hours.

The evaluation of the weight loss was recorded, so that the weight of the samples was recorded every 1000 hours; then the weight loss in percentages was recalculated.

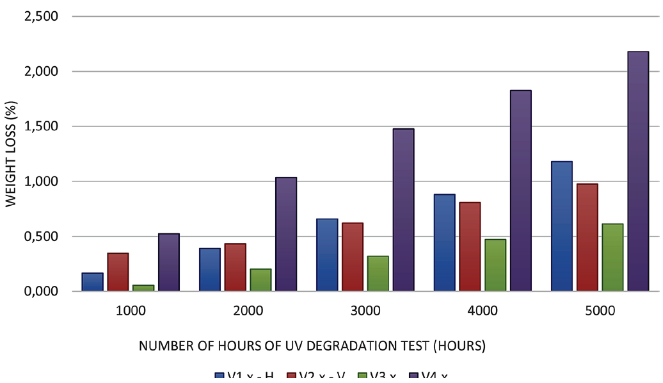

Graph 1 *Average weight loss for all types of PVC-P waterproofing tested*

Graph No. 1 shows a comparison of the total average weight loss value. Sample Nos. 1 and 2 are qualitatively among the best on our market. Sample No. 3 is a PVC-P film used to process details (without a reinforcing grid). We can observe that it has the smallest share of the percentage weight loss itself. Its UV stability is therefore higher, as it is used to process the most strenuous details of the roof cladding. Sample No. 4 is by a manufacturer whose products are often replaced in construction practice by higher quality materials designed by a designer. We can observe that the weight loss of this material has doubled. In this case, the weight loss was perceptible by touch and sight, versus plasticizers; the reinforcing grid stood out more on the surface, and the material itself was stiffer. The weight loss has a direct effect on the change in physical properties, e.g., the strength characteristics.

4.2.3 Preparation of the experimental measurements the strength test

The samples were gradually selected from the UV degradation device to perform a strength test after 1000, 2000, 3000, 4000, and 5000 hours. The test was also performed on samples without any UV degradation. For the implementation of the strength test according to STN EN 12311-2, it is necessary to prepare five pieces of the types of samples tested. From each sample in the QUV device, it was possible to prepare two samples for the market test. The preparation of the samples for the determination of strength properties was made according to STN EN 12311-2 for method B. They are dumbbell-shaped test specimens. A steel punch was designed and manufactured for making accurate samples. The samples were then cut using a manual hydraulic press. The strength / burst test was performed using the M500-25CT bursting device. The instrument is controlled by the winTest ™ Analysis software. It was necessary to set the boundary conditions such as the distance of the clamping jaws and the pull speed in the program, which is defined by the relevant standard STM EM 12311-2 to 100 mm / min.

Fig. 10 *Preparation of samples for the strength test*

Analysis of the results of the strength test

In terms of the presentation and clarity of the measurement results, three representative samples were selected from each material. Due to our experience with the implementation of the strength test, it was appropriate to test the samples without a reinforcing grid. The methodology requires that the samples must meet the same number of reinforcing fibers in one cut,

Fig. 11 Samples - photo before and after the strength test

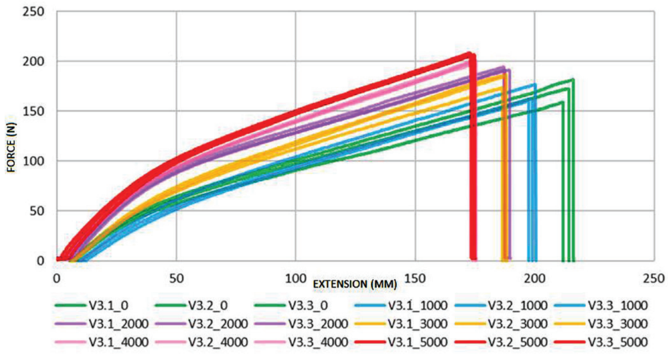

Graph 2 *Sample No. 3 comparison of the strength properties of the samples - without UV degradation and with UV degradation after 1000, 2000, 3000, 4000 and 5000 hours*

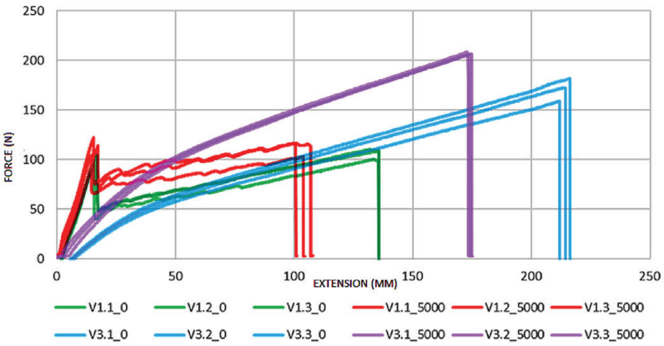

Graph 3 *Comparison of strength properties (Sample No. V1 with a reinforcing grid and Sample No. V3 without a reinforcing grid) without UV degradation and with UV degradation 5000 hours in the QUV machine.*

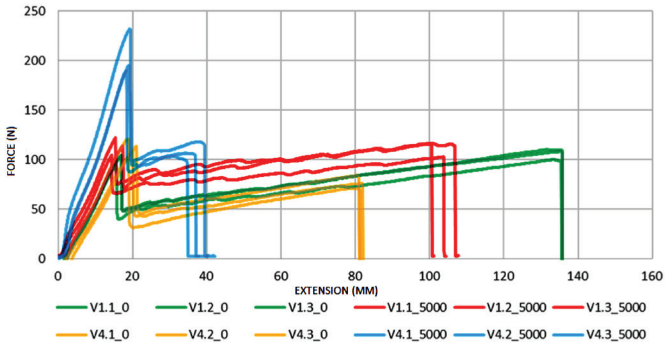

Graph 4 *Comparison of the strength properties (Sample Nos. V1 and V4 with a reinforcement grid) without UV degradation and with UV degradation, 5000 hours in QUV*

because according to the dumbbell shape selected for method B, the place where the failure is to occur is too narrow, and it is therefore very difficult to have the samples completely identical. This raises the question of whether this methodology is correct for testing similar types of PVC-P waterproofing membranes.

We can see the most representative results in terms of material degradation due to UV radiation in Graph No. 2. Sample No. 3 does not contain a reinforcing grid, so in this case we have a homogeneous material mixture. The graph confirms that the effect of UV radiation leads to a decrease in the plasticizers, which leads to a partial increase in strength and subsequently to an earlier failure. It is a roof covering which, thanks to its increased elasticity, is suitable for processing details (unaffected by the reinforcing grid). We can see the condition of the material before failure after rupture on the samples themselves; in this case there was an elongation of up to 215 mm.

Graph No. 3 represents a view of the individual properties of the coating with and without a reinforcing grid for the samples that were not exposed to UV radiation and samples with the UV degradation at a maximum of 5000 hours. Although the strength properties of the coating without a reinforcing grid are more favorable than the UV properties of a coating with a reinforcing grid, it is not appropriate to use this type of film in practice on common flat surfaces; as an advantage of the secondary function of the reinforcing grid, it resists impacts and local punctures, and at the same time ensures the cohesion of the material itself in the event of failure. For this reason, the use of an unreinforced coating is only recommended when machining the details.

Graph No. 4 compares coatings that are often alternated in their implementation. The coverings tested have almost identical parameters in the technical material sheets, but during the implementation of the experimental measurements, it was determined that the strength characteristics of these coverings are significantly different. A higher quality coating (V1) after exposure to UV degradation in the device after 5000 hours has better mechanical properties than a new lower quality coating (V4).

4.2.4 Preparation of the experimental measurements - infrared spectroscopy - analysis of the chemical changes on the surface of the material

The infrared spectra of the individual samples were recorded on a NICOLET 8700 ™ infrared spectrometer (Thermo Scientific, Madison, WI, USA) in the center of the infrared region (4000 - 650 cm^{-1}) with an Attenuated Total Reflection (ATR) using Germanium (Ge) as the optical material. The resolution was 4 cm^{-1}, and the number of scans for the measurements ranged from 32 to 64. For the infrared spectra obtained by the ATR technique in the case of using the Ge crystal, the maximum penetration of the infrared beam into the material was 0.66 µm at a wavelength of 1100 cm^{-1}.

For each series of samples, five measurements were made on each side of the samples from randomly selected locations, and the samples were composed of two different layers. The composition of the reinforcing bars was not involved in determining the chemical composition, but was relevant in monitoring the changes in the surface of the materials.

One representative spectrum was selected from each series of measurements for the evaluation, as the measured spectra differed only minimally within the measurements of the spectra of one sample. Nevertheless, it should be noted that when using the ATR technique, which scans the spectra from the surface (in this case from an area of about 2 mm^2, which is the contact area of the Ge crystal and the sample), it is also possible to detect the inhomogeneity of the chemical composition of the surface in the spectra. However, these are more time-consuming experiments (surface mapping using infrared microscopy) and therefore impractical for characterizing the surface of the material on a macroscale.

The measured spectra were evaluated using the OMNIC ™ v spectroscopic software 8.1. The results are presented in graphs as the dependence between the wavelength (the number of waves per unit length) and the absorbance (a dimensionless physical quantity expressing the amount of the visible spectrum of the electromagnetic radiation absorbed by a substance).

Analysis of results – infrared spectroscopy

As to Sample No. 4, changes in NH bonds were observed for the light and dark sides. In the light layer, which was probably stabilized by some type of UV stabilizer, the formation of and increase in the content of the polyene structures was observed after more than 3000 hours of aging. While this stabilizer is probably eliminated first and only when its effect disappears, the dehydrochlorination of the PVC then begins. At the same time, the spectra of the light layer after 4000 hours of aging also show changes in the CH region of the valence bonds (3040 - 2800 cm^{-1}), which is caused by the degrada-

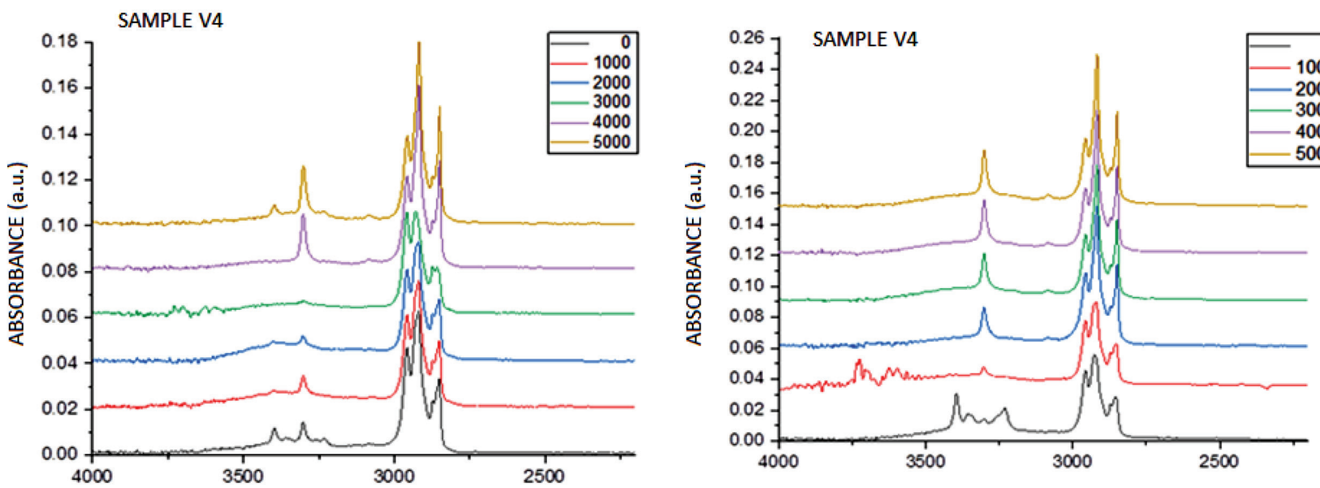

Graph 5 *Sample No. V4, light side (left) dark side (right), valence vibration area*

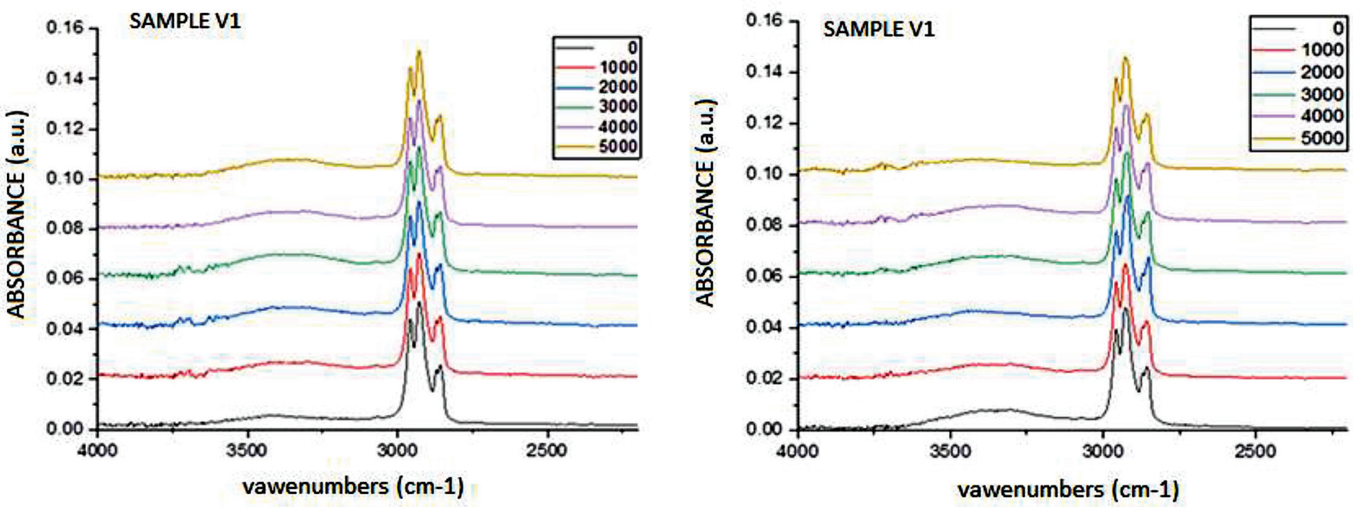

Graph 6 *Sample No. V1, light side (left), dark side (right), valence vibration area*

tion of the PVC chains and the formation of new terminal CH3 groups. This results in an increase in the absorbance values of these bonds (shorter polymer chains are formed, which also result in a deterioration of the mechanical properties).

Almost no changes in the spectra sensed in the central infrared region were observed in the spectra of the V1 (and V3) coverings during the aging of the material. The differences between the individual spectra are only in the region of the -OH valence and the deformation vibrations, which are caused by the binding of moisture to the material.

In conclusion, the infrared spectroscopy confirms the presence and loss of UV stabilizers, which have a direct effect on the mechanical properties that have been presented in the previous sections. The greatest changes are presented in Sample No. V4, where the greatest loss of weight and strength properties has also been confirmed. Infrared spectroscopy was also performed on the side not irradiated by the UV radiation, which gives us room in the future to solve not only degradation due to UV radiation, but also thermal aging.

4 CONCLUSION

Since plastics in construction do not belong among renewables, they must have a long service life and retain their own physical and mechanical properties. In construction, polymers appear in the form of waterproofing, whether on a substructure or roof. The subject of the paper is a physical-mechanical analysis of waterproofing materials for roof coatings loaded by the external environment over time (temperature, humidity, UV radiation, etc.). There are a few polymer-based roofing coatings on our market, but the most often used coatings in practice include PVC-P-based films. At present, manufacturers offer several variants of PVC-P films, which have significant differences in quality, but still meet the basic standards. Higher quality materials are often substituted for the sake of saving money, but they can result in damage to finances and health in the future.

The primary goal was an experimental analysis of waterproofing coating coverings in terms of UV radiation and humidity in a chamber for the accelerated aging of materials. Subsequently, secondary measurements were performed, namely, mass, strength and chemical analyses of the samples tested. The coefficient cannot be determined since a comparison of the experimental measurement with the measurement in external conditions requires a very long time. All the experimental measurements were based on the comparative method, the results of which are set out in the individual sections.

Our conclusion is that the experimental measurements point to a qualitative diversity of materials. We propose to proceed with the optimization of the methodology that evaluates the quality of the material and the fulfillment of quality requirements, which allows us to introduce new materials to the market. We propose to tighten the conditions according to the ETAG 006 or MOAT 65 documents, as experimental measurements have shown a large qualitative difference in materials that are often confused in construction practice. Furthermore, we propose the optimization of the technical materials supplied with the coatings. It is necessary to indicate the fulfillment of above-standard parameters, which demonstrably increase the service life of the material. We place emphasis on sufficient preparation of structural details from the point of view of their implementation in critically stressed areas. With the help of IR spectroscopy, other possibilities of examining the material were revealed. Degradation takes place on both sides of the surfaces. Degradation due to the temperature also occurs on the side that is not exposed to UV radiation. The reason is that, in addition to UV radiation and moisture, the material was also exposed to thermal aging at 50°C.

Acknowledgement

This research was supported by the Scientific Grant Agency of the Ministry of Education, Science, Research and Sport of Slovakia and the Slovak Academy of Sciences under VEGA 1/0396/21.

This research was supported by the Young Researcher 2019, No. 1602.

REFERENCES

Atlas Material Testing and Solutions, Weathering Testing Guidebook. [online] [quoted 27.12.2018]. Available from: http://www.strenometer.dk/files/downloads/guidebook.pdf

Beer H.R., Delgado A.H., Paroli R.M., Graveline S.P., *Durability of PVC Roofing Membranes – Proof by Testing After Long Term Field Exposure*. 10DBMC International Conference on Durability of Building Materials and Components, Lyon FR, 2005

Berdahl P., Akbari H., Levinson R., Miller W.A., Lawrence, *Weathering of roofing materials. Berkley National Laboratory, Environmental Energy Technologies Division*, Mail Stop 70-108B- 1 Cyclotron Road, Berkley, CA 94720, U.S., 2006

Bielek B., Bielek M., Vranay F., Lukášik D., Vranayová Z., Vilčeková S., Ehrenwald P., Híreš J., Majsniar V., Mikušová M. *Low-energy, green, sustainable building - climate - energy.* Slovak University of Technology in Bratislava, 2014. ISBN 978-80-227-4185-9.

Brian J. Whelan, Stanley P. Graveline, Ana H. Delgado, Karen Ky Liu, Ralph M. Paroli, Field *Investigation and Laboratory Testing of Exposed Poly (Vinyl Chloride) Roof Systems.* National Research Council of Canada – Institute for Research on Construction, Canada.

Bucko M., Hloch S., Vallíček J., Tozan H. Javadi Y. Ghosh A. *Influence of welding physical conditions on waterproofing membrane weld quality.* Croatia - Technical Journal 19, 2012 ISSN 1330-3651

Crewdson M., *Outdoor weathering must verify accelerated testing.* Q-Lab Weathering Research Service, 2007.

Gijsman P., *Review on the thermo-oxidative degradation of polymers during processing and in service*; e-Polymers 2008 No. 065; http://www.e-polymers.org ISSN 1618-7229.

Gregory R. Fedor and Patrick J. Brennan, *Comparison Between Natural Weathering and Fluorescent UV Exposures: UVA-340 Lamp Test Results*, 2011

Grip-Engineering Thümler GmbH. *Chambers for Tensile Tester* [online] [quoted 27.12.2018]. Available from: http://www.grip.de/pdf/TH2700_Datasheet.pdf

Johnson B.W., McIntyre R., *Analysis of test methods for UV durability predictions of polymer coatings,* Progress in Organic Coatings, 1996

Kicková M., Herditzky A., *History and development of plastic production* [online] [quoted 21.2.2019]. Available from: https://www.sjf.tuke.sk/transferinovacii/pages/archiv/transfer/11-2008/pdf/144-146.pdf

Kockott D., *Natural and artificial weathering of polymers*. Polym Degrad Stab, 1989

La Mantia F.P., Morreale M., Botta L., Mistretta M.C., Ceraulo M., Scaffaro R., *Degradation of polymer blends: A brief review.* Polymer Degradation and Stability, 2017

Labimex: Operating instructions QUV/spray, Labimex CZ, 2008

Lederer J. *Polyamide, Department of Chemistry, UJEP, CZ* [online]. [quoted 20.12.2018]. Available from: http://chemistry.ujep.cz/userfiles/files/PVC07022013.pdf

Liu H., Li B. Chen Z. Zhou T. Zhang Q., *Solar radiation properties of common membrane roofs used in building structures*. Materials and Design, 2016

Mleziva J., Šňupárek J. *Polymery výroba, struktura, vlastnosti a použití.* Prague, CZ, Sobotáles, 2000. ISBN 80-85920-72-7.

Nicolet FT-IR Spectrometer Brochure [Online] [quoted 10.05.2021] Available from: https://www.labwrench.com/documents/view/3512/thermo-scientific-nicolet-8700-ft-ir-spectrometer-brochure

Q-LAB, *Technical Manual LU-8047-TM – QUV Accelerated Weathering Tester*, 2016

Research and Markets, Polyvinyl Chloride (PVC) Global Supply Dynamics to 2020 - China Emerges as the Leader in Global Production. [online] [quoted 20.12.2018]. Available from: http://www.businesswire.com/news/home/20110110006117/en/Research Markets-Polyvinyl-Chloride-PVC-Global-Supply

Tocháček J., Vrátničková Z., *Polymer life-time prediction: The role of temperature in UV accelerated ageing of polypropylene an its copolymers*. Polymer Testing 36 (2014). CEITEC – Central European Institute of Technology, Brno, CZ

STN ISO 4892-3 – Plastics - Methods of exposure to laboratory light sources - Part 3: Fluorescent UV lamps

STN EN 12311-2 – Flexible sheets for waterproofing. Determination of tensile Properties. Part 2: Plastic and rubber sheets for roof waterproofing

EN 13956:2013 – Flexible sheet for waterproofing. Plastic and rubber sheets for roof waterproofing. Definitions and characteristics

EAD 030351-00-0402 – Systems of mechanically fastened flexible roof waterproofing sheets (superseding technical specification “ETAG 006” from 29.5.2019)

MOAT 65 – UEAtc Technical guide for the assessment of non-reinforced, reinforced and/ or backed roof waterproofing systems made of PVC

sciendo Slovak Journal of Civil Engineering
Vol. 30, 2022, No. 4, 49 – 54
DOI: 10.2478/sjce-2022-0028

REDESIGN OF AN INTAKE FISH PASS STRUCTURE

Lea ČUBANOVÁ[1*], Peter DUŠIČKA[1], Martin ORFÁNUS[1], Ján RUMANN[1]

Abstract

The article describes the process of redesigning the intake structure of the fish pass at the Žilina water structure in Slovakia. The existing intake structure does not meet the passability requirements for the target species of migratory fish. A design utilizing intake windows at various levels that cover fluctuations in the water level in the reservoir, which has been successfully used for other water structures, has been proposed. The new design was subjected to hydraulic calculations and simulations in the HEC-RAS 2D, 2D numerical model in order to achieve the required parameters such as the discharges, depths, and velocities within the limits for the specified fish zone.

Address

[1] Dept. of Hydraulic Engineering, Faculty of Civil Engineering, Slovak University of Technology in Bratislava, Slovak Republic

* ***Corresponding author:*** lea.cubanova@stuba.sk

Key words

- Fish pass,
- HEC-RAS 2D,
- Hydraulic parameters,
- Water intake,
- Velocity field,
- Depths.

1 INTRODUCTION

As a member of the EU, the Slovak Republic, is committed to making migration barriers passable (Directive 2000/60/EC), as is the case with other EU member states (Mader et al., 2020; Slavíková et al., 2020). This applies not only to the construction of new fish passes, but also the improvement of existing ones according to the latest knowledge and research (Directive DVWK 232/1996; Polák et al., 2015; Ocvirk et al., 2020) to meet the ecological requirements of the existing ichthyofauna.

The most significant problem in the passing of fish, either upstream or downstream, is attracting fish into the fish pass facility (Armstrong et al., 2020; O'Connor et al., 2017). The problematic sections are mostly the entrance (for upstream migrants) and the exit into the upstream water. For the entrance, it is recommended to locate it on a side of the hydropower plant close to the barrier and providing it with an additional attractive flow (Armstrong et al., 2020). The exit must also usually ensure the operation of the fish pass through a wide range of the water levels in the reservoir according to the operation of the water structure. A solution to these problems can be as follows: the upper pool can be used to adjust different headwater levels, while a second pool can be used to fine-tune the flow. On the other hand, a discharge control should be possible for the inflow, but for level fluctuations of 0.5 – 1.0 m, a vertical intake slot seems adequate; however, if the level differences are higher, several inflows with flow control functions should be included, as was used at the Váh cascade in Slovakia (Fig. 1) in the 1950s. The lateral positioning of the exit is also recommended, since this can lead any floating debris to bypass the entrance and also help to ensure that it is washed downstream during the cleaning process (Armstrong et al., 2020; Schmutz and Mielach, 2013).

2 MATERIALS AND METHODS

2.1 Description of the locality

The fish pass of the Žilina water structure on the Váh River (Fig. 2) was put into operation in 1998. It is unique in its length, i.e., 9 km, while overcoming a head of 25 m (Žilina, Váh basin, 2022). For the first time in the history of the Slovak Republic, an Environmental Impact Assessment (EIA) process was applied to this structure. Regular ichthyological monitoring, which has

Fig. 1 *The Váh cascade – the Drahovce water structure, inflow windows at different levels with control gates (photo from 2007, when the reservoir was empty)*

confirmed the occurrence of more than 30 species of fish, is carried out there; the most numerous species include: the common bleak (*Alburnus alburnus*), stone loach (*Barbatula barbatula*), barbel (*Barbus barbus*), common gudgeon (*Gobio gobio*), European chub (*Leuciscus cephalus*), and Eurasian minnow (*Phoxinus phoxinus*). The Váh River in this section is a typical foothill zone river, where there are fish of economic importance, as well as fish in the vulnerable category, which are included on the red list of fish in Slovakia with a special emphasis. The Váh River has a high diversity of species in this location; rheophilic (current) species logically predominate, as it is located in the upper part of the river (Čubanová and Rumann, 2018).

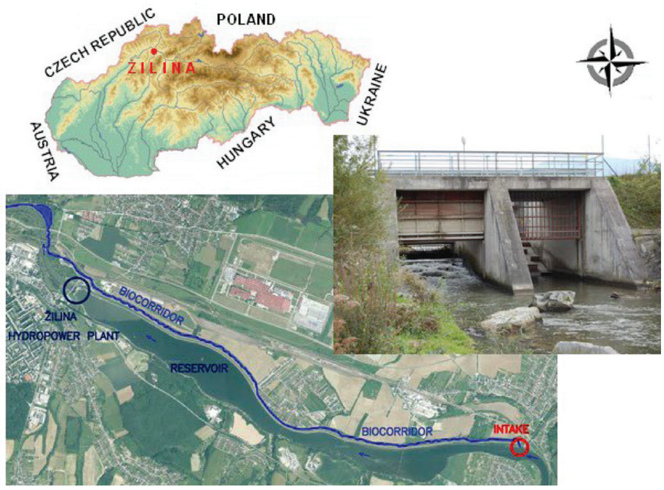

Fig. 2 *Map of the Slovak Republic with the area of interest – the fish pass of the Žilina water structure on the Váh River; the original intake structure is on the right*

2.2 Requirements according to the current regulations

The design parameters of the fish pass on the Žilina water structure at the time of its design were as follows (Čubanová and Rumann, 2018):

– a length of approximately 10 km,
– a trapezoidal cross section; the width at the river bed is 5 – 7 m,
– a water depth of 1 m,
– an operational flow rate of 2 $m^3 \cdot s^{-1}$,
– a flow velocity of 0.6 – 0.9 $m \cdot s^{-1}$ (maximum 1 $m \cdot s^{-1}$).

The riverbed itself meets passability requirements (O'Connor et al., 2017; Polák et al., 2015); the problem is the two-field intake structure. It is an automatic control gate with a flat sliding surface, i.e., a moving ramp (it is on its right side in Fig. 2), which must adjust to changes in the water levels in the reservoir according to the operations on the water structure. This structure is not very passable for the migrating ichthyofauna (the flow velocities exceed the limits); in addition, its functioning is strongly affected by its nearby confluence with the Varínka stream. Another problem that has emerged during the operation of this fish pass is at the outflow (for upstream migrating fish, this is the entrance to the fish pass), which is too far from the barrier itself. Moreover, for the fish, it is difficult to find it. Therefore, a redesign and reconstruction of the fish pass was proposed for these problem areas. The paper deals with the redesign of the existing intake structure.

According to updated ichthyological requirements in the valid Decree (Decree 383/2018) and the Methodological Guidelines (Polák et al., 2015), the barbel fish zone with an occurrence of Danubian salmon was selected as the target fish zone, with respect to the following fish species: the common barbel (*Barbus barbus*), nase (*Chondrostoma nasus*), East European bream (*Vimba vimba*), chub (*Leuciscus cephalus*), dace (*Leuciscus leuciscus*), bleak (*Alburnus alburnus*), grayling (*Thymallus thymallus*), and trout (*Salmo trutta*). According to the State Nature Conservancy of the Slovak Republic, passability is also required for the potential presence of Danube salmon (*Hucho hucho*) and protected low-skilled fish species. The focus of future monitoring will be on the mentioned fish species (after the reconstruction of the fish pass intake structure and its problematic parts).

The limit parameters recommended for a barrier-free fish pass in the barbel zone (Polák et al., 2015) are:

– a velocity of 1.2 $m \cdot s^{-1}$,
– a minimum depth of 50 cm,
– a minimum width at a water level of 5 m,
– a longitudinal slope of 1:70 – 1: 100,
– a resting pool after overcoming a head of 2 m,
– a chessboard layout of single stones (resulting in a sequence of spillovers and pools) protruding 30 – 40 cm above the riverbed bottom,
– good lighting and riparian planting.

2.3 Numerical simulations

The new intake structure is designed as a number of windows in the intake wall at various height levels (Fig. 3); it will be connected to the fish pass by a new channel through one of the existing fields of the original intake structure. The second field of the existing intake structure will be left as a bypass to improve the discharge in the fish pass to the required value (2 $m^3 \cdot s^{-1}$).

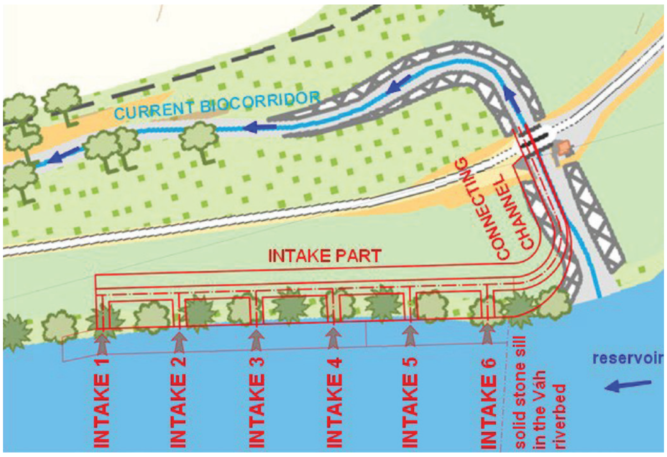

Fig. 3 *Layout of the redesigned intake structure*

The idea is that, after the overflow through the window while it is operating, the water will flow through a short connecting channel into the new fish pass channel, which will be located between the intake wall and a right-hand dike. The new channel of the fish pass (from the intake wall to the original intake structure) will have a zero longitudinal slope (a stream pool will be created).

There were 6 simulation sets according to the approval needed for the intake structure´s capacity. While the discharge in the main river was kept at an average discharge value of 95.6 $m^3 \cdot s^{-1}$, the operational water level at the Žilina water structure differs, depending on each intake window´s position, e.g., H = 352.2, 351.9, 351.6, 351.3, 351.0 and 350.7 m a. s. l.

The crucial criterion for assessing the suitability of the designed intake structure is to achieve the required discharge in the fish pass, cover the fluctuations of the operating levels, and not exceed the flow velocity limit, which was set for the inflow facility at 1.5 $m \cdot s^{-1}$ (this corresponds to a large chamber pool ramp with barriers in the barbel zone). The final design of the intake structure was selected from various proposed designs, which were simulated using a 2D hydrodynamic model. As a primary tool to determine the hydrodynamic conditions at the intake structure, the 2D HEC-RAS software (HEC-RAS Documentation, 2022) was used. The HEC-RAS 2D modelling tool can be used in situations involving detailed 2D channel and floodplain modelling, combined 1D and 2D modeling, simplified dam or levee failure studies, and numerous other tasks.

The 2D Full Momentum computational method, also known as the St. Venant equations for shallow water, was used. Solving the St. Venant equations involves higher computational demands and longer solution times. The advantage of this method is the large number of applicable scenarios, including dynamic flood waves, sudden expansion or contraction of flows, mixed flow regimes, and wave propagation (i.e., waves reflecting off walls and structures). If the flow is incompressible, then the unsteady differential form of the mass conservation (continuity) equation is (Eq. (1) (HEC-RAS Documentation, 2022):

$$\frac{\partial h}{\partial t} + \frac{\partial (hu)}{\partial x} + \frac{\partial (hv)}{\partial y} = q \tag{1}$$

where t is the time; u and v are the velocity components in the x- and y- directions, respectively; and q is a source/sink flux term. In vector form, the continuity equation takes the following form (Eq. (2) (HEC-RAS Documentation, 2022):

$$\frac{\partial h}{\partial t} + \nabla \cdot (hV) = q \tag{2}$$

where $V=(u,v)^T$ is the velocity vector, and ∇ is the gradient operator $\nabla=(\partial/\partial x, \partial/\partial y)^T$.

Integrating over a horizontal region with the normal boundary vector n and using the Gauss Divergence theorem, the integral form of the equation is obtained (Eq. (3) (HEC-RAS Documentation, 2022):

$$\frac{\partial}{\partial t}\iiint_{\Omega} d\Omega + \iint_{S} (V \cdot n) dS = Q \tag{3}$$

where the volumetric region Ω represents a three-dimensional space occupied by the fluid, and n is the unit vector normal to the side boundaries S. It is assumed that Q represents any flow that crosses the bottom surface (infiltration) or the top water surface of Ω (evaporation or rain). In this context, the volume Ω will represent a finite volume cell, and the integrals will be computed using information about the fine underlying topography. Every term of the momentum equation has a clear physical counterpart. From left to right, the terms are unsteady acceleration, convective acceleration, the Coriolis term, the barotropic pressure term, momentum diffusion, bottom friction, and wind forcing (HEC-RAS Documentation, 2022).

When the depth is very shallow, the bottom friction term dominates the equation. As a consequence, dry cells take the limit form $V = 0$. Because the conservation of momentum is directionally invariant, the momentum equation may be in any direction. In HEC-RAS, the momentum is computed as normal to each face (Eq. (4) (HEC-RAS Documentation, 2022):

$$\frac{\partial u_N}{\partial t} + (V \cdot \nabla) u_N - f_c u_T = -g\frac{\partial z_s}{\partial N} + \frac{1}{h}\nabla \cdot (v_t h \nabla u_N) - \frac{\tau_{b,N}}{\rho R} + \frac{\tau_{s,N}}{\rho h} \tag{4}$$

where fc is the Coriolis parameter; g is the gravitational acceleration; z_s is the water surface´s elevation; h is the depth of the water; $\tau_{b,x}$ and $\tau_{b,y}$ are bottom shear stresses in the x- and y- directions; R is the hydraulic radius; and $\tau_{s,x}$ and $\tau_{s,y}$ are surface wind stresses in the x- and y- directions, respectively.

The basic 2D computational methodology assumes that the vertical fluid motion is negligible; the velocity is vertically averaged at the cell center (the depth´s averaged flow); the energy head is computed at the cell center; the Manning's roughness coefficient assigned on the cell´s face uses the roughness value at the cell face´s center, and the Manning's roughness coefficient is constant across each cell face, although each cell face can have its own value (HEC-RAS Documentation, 2022).

The numerical model contains two calculation domains:

- the Váh riverbed together with the Varínka riverbed,
- the fish pass channel.

The domains are connected by an empirical scheme of the inflow structure with the capacity calculated according to the continuous results of the inflow velocities and water levels in both domains at the inflow windows (Bytčanková et al., 2021).

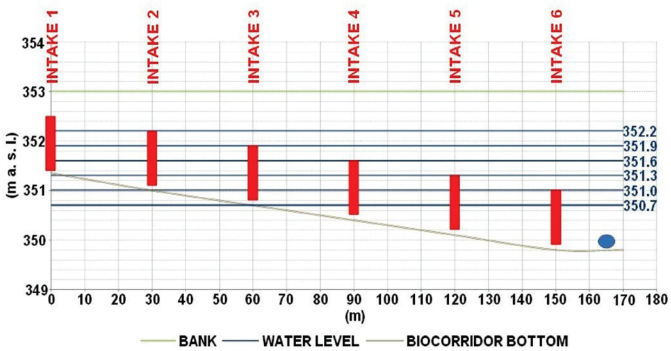

Fig. 4 *Position of the intake windows and the range of operating water levels in the reservoir (order of intake windows from the left, according to Fig. 3)*

3 RESULTS

The new intake structure, with 6 equal intake windows at an axial distance 30 m on the right bank of the reservoir close to the original one (Fig. 4), is designed for a free surface flow in the entire range of the operating levels (assumptions/requirements):

– the fixed top edge of the window is at least 20 cm above the maximum water level for the given window,
– in the range of the operating water levels, the depth of water in the given windows is 70 – 40 cm (in case the width of the opening is too small, the depth of water will be in a range of 60 – 30 cm); the width of the windows will narrow so that at the maximum water level, a discharge of 2 $m^3 \cdot s^{-1}$ will flow through the opening,
– a maximum flow velocity of 1.5 $m \cdot s^{-1}$ is acceptable in the window opening,
– the openings will be equipped with sluice gates without any discharge regulations (this means 2 positions, i.e., open or closed),
– at the end of the intake facility, a water supply structure will be built that will supply minimum discharges in the fish pass so that a minimum discharge of 2 $m^3 \cdot s^{-1}$ is in the fish pass itself; at the same time, it will serve as a backup facility during any failure of the intake structure, so that water will be supplied in the fish pass all the time,
– the regulation range of the possible discharge flow through this structure will be 0 – 2 $m^3 \cdot s^{-1}$.

After a series of calculations, the dimensions of each opening window were designed to be 1.1 m x 1.8 m (height x width). With these dimensions, the following requirements will be met:

– the fixed top edge of a window will be 30 cm above the maximum water level for that window,
– in the range of operating water levels, the depth of the water in the given window will be 80 – 50 cm,
– discharges through the window will be (Tab. 1):
  • at the target water level (at the same time as the maximum water level for the window), Q = 2.56 $m^3 \cdot s^{-1}$ (the difference in the water levels in the reservoir and the fish pass will be 0.37 m),
  • at the middle water level (15 cm less than the target water level), Q = 1.65 $m^3 \cdot s^{-1}$ (the difference in the water levels in the reservoir and the fish pass will be 0.33 m),
  • at the minimum water level (30 cm less than the target water level and the same as the next lower target water level), Q = 0.94 $m^3 \cdot s^{-1}$ (the difference in the water levels in the reservoir and the fish pass will be 0.29 m).

The simulation results show that the intake structure with an uncontrolled flow through the intake windows cannot provide a constant discharge to the fish pass due to the changes in the water level in the main reservoir. When the discharge drops below the required value of 2 $m^3 \cdot s^{-1}$, the water supply structure (built at the end of the intake wall) must supplement the missing discharge. Another way of doing this is to control the flow at the intake windows with the sluice gates of the higher-placed intake window. Based on the results of the numerical model and published hydraulic research on the issue of the distribution of vertical velocity (Velísková et al., 2018; Kašpar et al., 2021; Bytčanková et al., 2021), the course of vertical velocities in the intake opening is stated in Fig. 5 and Tab. 1.

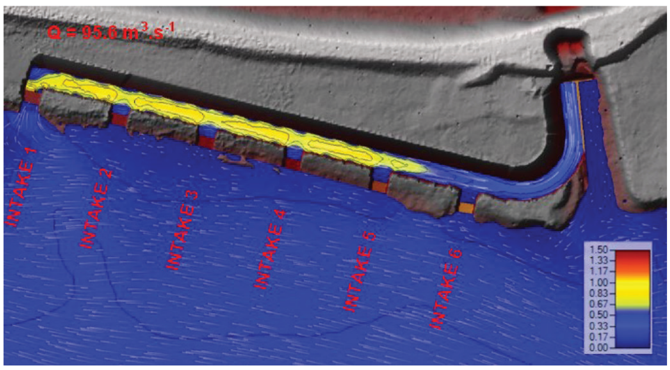

Fig. 5 *Simulated velocity field in the area of the intake structure at an average discharge of 95.6 $m^3 \cdot s^{-1}$ in the Váh River and an operational water level of 350.7 m a. s. l. at the Žilina water structure (order of intake windows from the left, according to Fig. 3)*

Tab. 1 *Final results from the hydraulic research for a single window*

water level in the intake window	discharge through the window	difference in the water level at the window	depth in the window	average velocity	velocity on the water surface	velocity at the bottom of the window
	($m^3 \cdot s^{-1}$)	(m)	(m)	($m \cdot s^{-1}$)	($m \cdot s^{-1}$)	($m \cdot s^{-1}$)
maximum	2.56	0.37	0.80	1.8	2.0	1.2
middle	1.65	0.33	0.65	1.4	1.6	1.0
minimum	0.94	0.29	0.50	1.0	1.1	0.7

4 CONCLUSIONS

There is a complex spatial flow in and around intake structures. Hydraulic calculations are performed under certain conditions. The velocities and discharges are also conditioned by the shape and width of the opening edge and other construction modifications on the intake structure, the connecting channel, and the fish pass bed. Based on the recommendations of an ecologist consultant, it would be necessary to further reduce velocities on the intake bed and immediately behind it. This can be achieved with several adjustments. One option is to increase the number of windows, which also means increasing the number of target water levels. This would reduce the difference in the water level between the target levels for each intake window. Another option, which would be also recommended, is to increase the roughness on the river bed bottom locally by individual/single stones (by keeping the number of intake windows to 6). It is assumed that such an adjustment would also reduce the discharge through the structure, which could be partially compensated for by increasing the width of the window. However, this would require more detailed research using 3D mathematical or physical models.

The intake structure is one of the key structures in the design of any type of fish pass. During a time of climate change, when the water levels in streams change, an intake structure with flow controls is the most suitable design with which to provide the operating conditions of fish passes. In the past, commonly used intake windows, which were placed on several levels covering the operational range of the water levels during the operation of water structures, have been a relatively simple solution. Verification of the complex 3D flow in and around these intake structures is the subject of verification on physical models, where it is possible to measure the discharges, depths, and velocities for different operating conditions, which can be achieved by the design of this structure to ensure its functionality after its construction.

Acknowledgments

This work was supported by the Ministry of Education, Science, Research and Sport of the Slovak Republic within the Slovak Research and Development Agency, Project Nos. APVV-20-0023 and APVV-18-0472.

REFERENCES

Armstrong, G. S. – Aprahamian, M. W. – Fewings, G. A. – Gough, P. J. – Reader, N. A. – Varallo, P. V. (2020) *Fish Pass Manual: Guidance Notes On The Legislation, Selection and Approval Of Fish Passes in England and Wales*. Institute of Fisheries Management, UK.

Bytčanková, L. - Rumann,J. - Dušička, P. (2021) *Analyzing the impact of intake structure on the flow at low pressure SHPP*. Pollack Periodica, vol. 16, no. 1, pp. 114-119.

Čubanová, L. - Rumann, J. (2018) *Field research of fish pass - case study Žilina water structure*. Journal of Landscape Management, Vol. 9, no. 2, pp. 11-15.

Decree 383/2018 (2018) *Vyhláška MŽP SR o technických podmienkach návrhu rybovodov a monitoringu migračnej priechodnosti rybovodov* (*On technical conditions for the design of fish passes and monitoring of the migration passability of fish passes)*. Bratislava, Ministry of the Environment of the Slovak Republic [in Slovak].

Directive 2000/60/EC (2000) *Water Framework Directive*. The European Union, Bruxelles, Belgium.

Directive DVWK-Merkblatt 232/1996 (1996) *Fischaufstiegsanlagen - Bemessung, Gestaltung, Funktionskontrolle (Fish passes – Design, dimensions and monitoring)*. German Association for Water Resources and Land Improvement, Bonn, Germany [in German].

HEC-RAS Documentation (2022) *HEC-RAS Hydraulic Reference Manual*. Available at: https://www.hec.usace.army.mil/confluence/rasdocs/ras1dtechref/latest/theoretical-basis-for-one-dimensional-and-two-dimensional-hydrodynamic-calculations/2d-unsteady-flow-hydrodynamics/hydraulic-equations (accessed at 15/06/2022).

Kašpar, T. - Fošumpaur, P.- Králík, M. - Zukal, M. (2021) *Parametric study of direct filling system of medium-head navigation locks*. Pollack Periodica, vol. 16, no. 2, pp. 43-49.

Mader, H. - Brandl, A. - Käfer, S. (2020) *Design and Function Monitoring of an Enature® Vertical Slot Fish Pass in a Large Potamal River in Carinthia/Austria*. *Water,* 12, no. 2: 551, pp. 1-26.

O'Connor, J. - Stuart, I. - Jones, M. (2017) *Guidelines for the design, approval and construction of fishways*. Arthur Rylah Institute for Environmental Research. Technical Report Series No. 274. Department of the Environment, Land, Water and Planning, Heidelberg, Victoria, Australia.

Ocvirk, E. - Gilja, G. - Bujak, D. - Cikojević, A. – Jelić, D. (2020) *Nomogrami za proračun funkcionalnosti tehničkih ribljih staza na malim pragovima (Nomograms for calculating the funcionality of technical fish passes on small sills)*. Hrvatske vode, 28, 111, pp. 9-20 [in Croatian].

Polák, V. - Mužík, V. - Druga, V. - Abaffy, A. - Rebenda, F. - Matok, P. - Mravcová, K. - Hránková, R. - Čomaj, **M. - Joštiaková, D. (2015)** *Určenie vhodných typov rybovodov podľa typológie vodných tokov: Metodické usmernenie (Determination of suitable types of fish passes according to the typology of streams: Methodological guidelines)*. Výskumný ústav vodného hospodárstva (Water Research Institute), Bratislava, Slovak Republic [in Slovak].

Slavíková, A. - Pravec, M. - Horecký, J. – Dobrovský, P. (2020) *Koncepce zprůchodnění říční sítě ČR, aktualizace 2020 (The concept of the river network passability of the Czech Republic, update 2020)*. MŽP ČR, Czech Republic [in Czech].

Schmutz, S. - Mielach, C. (2013) *Measures for ensuring fish migration at transversal structures. Technical paper*. International Commission for the Protection of the Danube River, Vienna, Austria.

Velísková, Y. - Chára, Z. - Schügerl, R. - Dulovičová, R. (2018) *CFD simulation of flow behind overflooded obstacle*. Journal of Hydrology and Hydromechanics, Vol. 66, No. 4, p. 448-456.

Žilina, basin of Váh **(2022)** *Slovak National Committee on Large Dams*. Available at: http://t3.skcold.sk/?id=58 (accessed at 15/06/2022).

Slovak Journal of Civil Engineering

Vol. 30, 2022, No. 4, 55 – 63
DOI: 10.2478/sjce-2022-0029

DETECTION OF CHANGES IN EVAPOTRANSPIRATION ON A CATCHMENT SCALE UNDER CHANGING CLIMATE CONDITIONS IN SELECTED RIVER BASINS OF SLOVAKIA

Anita KESZELIOVÁ[1], Roman VÝLETA[1], Michaela DANÁČOVÁ[1*], Kamila HLAVČOVÁ[1], Patrik SLEZIAK[2], Zoltán GRIBOVSZKI[3], Ján SZOLGAY[1]

Abstract

Potential changes in a hydrological regime caused by a changing climate represent a crucial source of uncertainty in water resources management. For example, in Slovakia, they may manifest themselves in a decrease in water resources, a change in the seasonality of runoff, and an increase in the extremes of floods and droughts. The research presented here focuses on using the hydrological balance equation to predict changes in the total catchment evapotranspiration under changing climate conditions. Using the TUW rainfall-runoff model and the KNMI and MPI climate change scenarios, the hydrological regime of eight selected basins in Slovakia was simulated for three thirty-year periods from 2010 until the year 2100. The results showed that the growth of total catchment evapotranspiration observed in recent decades is likely to increase further in the future.

Address

[1] Dept. of Land and Water Resources Management, Faculty of Civil Engineering, Slovak University of Technology in Bratislava, Slovakia

[2] Institute of Hydrology, Slovak Academy of Sciences, Bratislava, Slovakia

[3] University of West Hungary, Institute of Geomatics and Civil Engineering, Sopron, Hungary

* ***Corresponding author:*** michaela.danacova@stuba.sk

Key words

- Evapotranspiration,
- Hydrological balance,
- Seasonality,
- Climate changes.

1 INTRODUCTION

It is generally accepted that human activity has affected the Earth's climate and, thus, the global hydrological cycle. However, the strong natural variability of climates makes it difficult to estimate the human contribution to changes in the hydrological cycle on the catchment scale. The trends observed in the behaviour of various hydrological elements are not always significant statistically and therefor conclusive. On a local scale, more rain and less snow is expected in mountainous areas in a warmer climate. Anthropogenic warming also increases the water capacity of the atmosphere with consequences for increased evaporation and evapotranspiration over oceans and land, which can cause more extreme precipitation and increase the share of total annual precipitation. Randomly occurring extreme and other deviations from regional trends make the detection and attribution of changes even more difficult.

However, since all components of the hydrological cycle are directly or indirectly affected by rising air temperatures, this must also be reflected in the hydrological balance of a basin. Studying the relationship of the balance provides insight into the complex system of processes that operate in space and over time during the movement of water in nature through the soil, vegetation and the atmosphere. From the point of view of the hydrological balance, a changed precipitation regime can have both favourable and unfavourable effects on the replenishment of underground water supplies. Monitoring and predicting changes in the long-term regime of the key elements of the hydrological balance on a basin scale is, therefore, urgent. Through analyzing the balance, the indirect detection of changes in particular hydrological elements is also possible.

When computing a hydrological balance, it is crucial to integrate data on the hydrological cycle into a consistent set of figures, which must adequately represent the processes that must be considered on the given temporal and spatial scales. Integrating datasets from different sources requires a careful selection of the available data products of each variable, taking into account the appropriate spatial and temporal resolutions (Dorigo et al., 2021). The data selection determines whether and how the closure of the hydrological balance is ultimately achieved. Ideally, consistency between the selected data products would already be taken into account at the acquisition stage (Popp et al., 2020), but this is generally impossible due to the diversity of monitoring programs for the different components of the water cycle. Problematic elements include, for example, total evaporation from the catchment estimated by modelling or by analogy, estimates of the flow in unmeasured basins, or withdrawals from reservoirs estimated from observing changes in water levels (Pellet et al., 2019). Determining the values of total evapotranspiration and subsurface runoff is especially problematic. Using the example of the balance of 63 basins of the Amazon River, Posada and Poveda (2020) discussed the reasons for not closing the balance due to nonstationarity, which can make it difficult. From the point of view of the integration of the data from different sources, we can say that the larger the scales, the lower the uncertainty of determining the individual balance inputs due to the averaging of the data (Rodell et al., 2015). For example, when considering the hydrological balance of a basin over several decades, we can deal with the long-term average values of the inputs and ignore changes in all the forms of water accumulation in the basin. However, due to the difficulty of measuring evapotranspiration (ET) and the inaccuracy of estimating total rainfall in a catchment, the factors affecting changes in ET are the subject of research and debate (Duethmann and Blöschl, 2018). Territorial evapotranspiration values cannot be measured directly; the only possibility is assessing them indirectly.

A robust and straightforward option for estimating territorial evaporation is evaluating the hydrological balance equation on the basin level, especially when calculating its long-term average (Duethmann and Blöschl, 2018). Estimates of the evapotranspiration itself can be based on experimental on-site micrometeorological assessments (e.g., evaporimeters and lysimeters) (Hobbins et al., 2004), spatial estimates using remote sensing methods (Zhang et al., 2010; Gao et al., 2010), and outputs from rainfall-runoff models (e.g., Parajka et al., 2004; Huang et al., 2020). In addition, we can use spatial interpolation methods from empirical point estimates of actual evapotranspiration performed in a large number of ways of varying complexity (Hobbins et al., 2001; Lapin et al., 2016). Hydrological mapping can also estimate their values (e.g., Parajka et al., 2004). As a result of the above-mentioned problems, it is clear that if we accept the assumption of closure of the balance, the estimate of ET will contain the uncertainties mentioned above (Fekete et al., 2004; Wang et al., 2014 a, b). However, for practical reasons, we cannot consider this as a reason for cancelling the use of balance in hydrology (Safeeq et al., 2012). Therefore, to use the hydrological balance as a method for changes in the hydrological regime in a period of a changing climate, we can say that it is appropriate to try to use it on the scale of basins, with an annual time step, and for a sufficiently long period (on the order of decades).

Many studies have reported that evapotranspiration has regionally increased in many parts of the world in recent decades (Zhang et al., 2010). Investigations of trends in catchment evapotranspiration through the hydrological balance have generally noted an increase in recent decades (Domokos and Sass, 1990; Mills, 2001; Weingartner et al., 2007; Trenberth et al., 2007). A global study found positive (but only sometimes significant) trends in North and South America and Europe and negative trends in Africa and Siberia (Ukkola and Prentice, 2013). Many studies have been devoted to the river basins of North America (Milly and Dunne, 2001; Walter et al., 2004; Gao et al., 2010; Kramer et al., 2015; Xiao et al., 2020). National assessments have also been published (Mills, 2001; Weingartner et al., 2007; Duethmann and Blöschl, 2018; Mastrotheodoros et al., 2020; Xiao et al., 2020; Tomas-Burguera et al., 2021). Several results of the assessment of changes in the elements of the hydrological cycle in Slovakia also indicate that their regime has recently changed (e.g., Blaškovičová et al., 2019; Fendeková et al., 2018). Consistent trends regarding their development have been found, and some of these were significant (e.g., Lapin et al., 2016; Pramuk et al., 2016; Ďurigová et al., 2019; Halmová et al., 2019; Ďurigová, 2020). Overall, more work has been devoted to looking for trends in time series of the elements of the hydrological balance and changes in their regime than comparing changes in the overall balance. Impacts due to climate change concerning the general hydrological balance have been rare.

Rončák and Šurda (2019) and Rončák et al. (2019) have dealt with estimating the components of the water balance under a changing climate in selected basins of Slovakia. Using the spatially distributed WetSpa model, the KNMI and MPI regional climate models, and the SRES emission scenario for future estimates have shown an increase in the current evapotranspiration and a decrease in soil moisture in future horizons compared to the reference period of 1981-2010. Csáki et al. (2020) has developed a long-term climate-runoff model. Long-term evapotranspiration and runoff values have been projected for three periods (2011–2040, 2041–2070, 2071–2100) over the Zala River Basin in Hungary, using data of 12 regional climate models. According to the projections, by the end of the century, the annual evapotranspiration rate is expected to increase by 4-5% relative to the reference period (1981–2010).

In this study, we primarily focused on evaluating the equation of the hydrological balance in eight pilot catchments in Slovakia under changing climate conditions. The work does not aim at developing or testing new modelling procedures. The main goal is to gain new knowledge about the possible impacts of climate change on the hydrological balance using a series of published data in Sleziak et al. (2021).

2 MATERIAL AND METHODS

2.1 Pilot basins and data

The study herein follows up on Sleziak et al. (2021), from which we have adopted the climate and runoff data. We have selected eight watersheds as pilots (see Fig. 1). All the chosen basins lack anthropogenic influences. They cover the territory of Slovakia in a transect from west to east and represent different altitudinal zones. The basin sizes proved suitable for using a conceptual rainfall-runoff model with a daily step. Tab. 1 summarizes the main basin characteristics. The dimensions of the basins range from 238 km^2 (Myjava - Jablonica) to 2094 km^2 (Nitra - Nitrianska Streda); the mean elevations vary from 362 m a.s.l. (Myjava - Jablonica) to 1090 m a.s.l. (Váh - Liptovský Mikuláš). Using the inverse distance weighting method, precipitation from the individual climate stations was aggregated into average precipitation totals for the basins. The average daily air temperatures per watershed were calculated using the gradient method for the median elevation of the watershed. The average daily potential evapotranspiration per watershed was calculated by a modified Blaney–Criddle method.

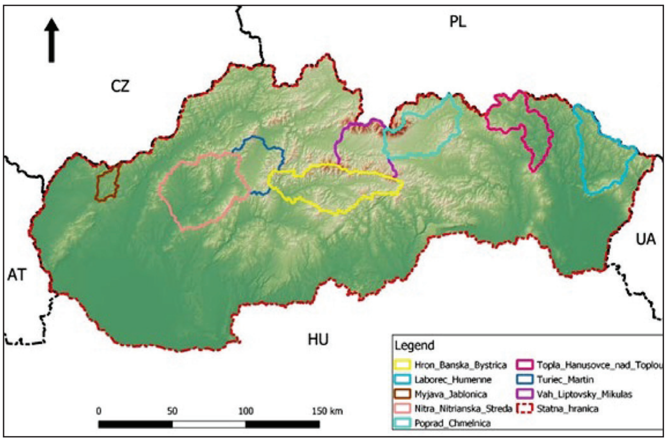

Fig. 1 *Topography of Slovakia and locations of the eight river basins selected*

Tab. 1 *Basic characteristics of the selected pilot catchments of Slovakia*

ID	Gauging station	River	Catchment area	Mean elevation
			[km^2]	[m a.s.l.]
5022	Jablonica (J)	Myjava	238.5	361.7
6730	Nitrianska Streda (NS)	Nitra	2093.7	419.5
9230	Humenné (H)	Laborec	1272.4	421.7
9500	Hanušovce nad Topľou (HnT)	Topľa	1050.0	435.4
6130	Martin (M)	Turiec	827.0	716.0
7160	Banská Bystrica (BB)	Hron	1766.5	844.4
8320	Chmeľnica (Ch)	Poprad	1262.0	878.1
5550	Liptovský Mikuláš (LM)	Váh	1107.2	1090.1

The data input (i.e., the mean daily air temperatures and daily precipitation totals) for the modelling of runoff in the period 2010 to 2100 were generated by two regional circulation models (RCMs). The Koninklijk Nederlands Meteorologisch Instituut (KNMI) and Max Planck Institute (MPI) models are based on the German ECHAM5 general circulation model (GCM) boundary conditions and represent a detailed integration of the atmospheric and oceanic dynamic equations with a grid point resolution of roughly 25 × 25 km (Lapin et al., 2012).

In impact studies conducted in Slovakia, the moderately pessimistic SRES A1B emission scenario is usually adopted. This emission scenario is between the SRES B1 (relatively low emission of greenhouse gases) and A2 (a rather high emission of greenhouse gases) scenarios (Minďáš et al., 2015). Outputs from both RCMs were downscaled into a network of climate stations (Lapin et al., 2012). Details are given in Fendeková et al. (2018). The outputs from both climate models for the basins studied were downscaled to the climatic stations and interpolated using the Inverse Distance Weighted (IDW) and altitude gradient methods on the basin's data. The values of the mean daily air temperatures and daily precipitation totals were used as the daily basin average data for the period between 2011 and 2100.

The data from Sleziak et al. (2021) contain the simulated runoff for the reference period (1981-2010) in a daily time step from eight basins in Slovakia and for three thirty-year periods from 2010 until 2100 (2011-2040, 2041-2070, 2071-2100). To simulate runoff driven by precipitation from the KNMI and MPI regional climate models in the Slovak basins selected, the conceptual rainfall-runoff (r-r) TUW model was chosen. The TUW model is a lumped model based on the structure of the widely used Swedish Hydrologiska Byrans Vattenbalansavdelning (HBV) model. The model has recently been proven to be suitable for analyses of the impact of climate change on water resources in several studies concerning Slovakia (e.g., Sleziak et al.,2016; Sleziak et al., 2018; Aleksić et al., 2021).

Sleziak et al. (2021) described three thirty-year periods (2011-2040, 2041-2070, and 2071-2100) separately and in detail for each pilot river basin. Changes in the long-term mean monthly climatic characteristics (air temperature and precipitation) according to both climate models are expected to be similar for each river basin. An increase in precipitation can be expected during the spring, autumn, and winter periods. Precipitation is expected to decrease in the summer. Based on the KNMI model, the largest increase in precipitation is expected to be in September (2071-2100). Interestingly, the maximum of the long-term mean monthly precipitation could be shifted from July to September in all three future periods. The MPI model predicts the largest precipitation increase to be in March for the period 2071-2100. The long-term mean monthly air temperatures will rise steadily according to both scenarios.

2.2 Methodology

Total evapotranspiration in a catchment's hydrological balance is the total amount of water in all its forms that evaporates from the catchment over a specified period of time. Several synonyms, such as actual evapotranspiration, climatic evaporation, territorial evaporation, and total evaporation are used (Keszeliová et al., 2021). Both "actual catchment evapotranspiration" and a total catchment or a basin evapotranspiration will be used herein.

The relationship between the volumes of water entering and leaving the area of a catchment during a given time interval Δt can be described as a conservation of mass by (e.g., Keszeliová et al., 2021):

$$Z + K + P_P + P_R + P_{PZ} = O_P + O_{PZ} + O_O + V + \Delta R \quad (1)$$

where the individual symbols represent the following volumetric quantities:

Z – vertical precipitation,
K – horizontal precipitation (e.g., condensation of water vapour),
P_P – the natural influx of water on a surface into a catchment,
P_R – the anthropogenic transfer of water into a catchment,
P_{ZP} – the natural groundwater inflow into a catchment,
O_P – the natural surface outflow of water from the catchment,
O_{PZ} – a natural underground outflow from a catchment,

O_O – abstractions of the surface and groundwater transferred outside the catchment,
V – the total evaporation of water from the territory (actual catchment evapotranspiration), which includes all forms of water evaporation and plant transpiration),
ΔR – change in the water storage in the catchment over the time interval Δt considered.

The values of the variables of the balance equation can be expressed in volumetric units or units of depth for the given catchment (precipitation depth, runoff depth).

When assessing the hydrological balance of natural catchments (without any anthropogenic effect on the budget) over a sufficiently extended period to ignore any change in storage, the equation may be simplified as:

$$Z = O + V \qquad /\Delta t \tag{2}$$

where: Z, O, and V are the atmospheric precipitation, runoff, and actual catchment evapotranspiration, respectively; and Δt is a relatively long period of time (Duethmann and Blöschl, 2018). By dividing both sides of the equation by the duration of the period under review (Δt), we can express its terms as the long-term average values of the river basin's atmospheric precipitation, runoff, and actual evapotranspiration (e.g., Keszeliová et al., 2021).

As a central part of this case study, we are addressing the question of how climate change may affect the hydrological balance. To analyze changes in the behaviour of the elements of a balance, the linear trends of its components in the eight pilot basins were evaluated. We have tested the acceptance of the trends observed by the standard Mann-Kendall test (e.g., Ďurigová et al., 2019). We have used the calendar year as the basis of the balance.

The TUW rainfall-runoff model, which produced the data analyzed herein, uses the inputs of the average basin values of the mean daily air temperatures, daily precipitation totals, and potential evapotranspiration. The model has 15 parameters that need to be calibrated. The evolution strategy, known as differential evolution (Mullen et al., 2011; Ardia et al., 2016), was used for the parameter optimization. It is considered successful in finding the global optimum of a real-valued function of real-valued parameters and does not need continuous or differentiable objective functions.

In Sleziak et al. (2021), the model was calibrated/validated consecutively for four 10-year periods between 1981-2019. The objective function for the runoff was the average of the Nash-Sutcliffe coefficient (NSE), and the logarithmic NSE (Nash and Sutcliffe, 1970) was applied. For simulating the future runoff conditions, parameters from the most recent calibration period (i.e., 2011-2019) were selected because it was assumed that this period should be similar (mainly in terms of the mean daily air temperatures) to a recent/warmer climate.

As seen in Fig. 2 below, it was decided that it was more acceptable to choose a period that could be similar in temperature to a future (i.e., warmer) climate. This consideration was also supported by a comparison of selected quality indicators of model simulations during the cross-validation in the periods 1981-1990, 1991-2000, 2001-2010, and 2011-2019.

3 RESULTS

A comparison of the development of the hydrological balance in the coming decades for both scenarios simultaneously and separately for the individual pilot basins is presented; they are sorted according to their average elevation. In addition, we have compared changes in the long-term averages of the main elements of the hydrological balance between the simulated reference (baseline) period of 1981-2010 and the projection periods of both scenarios in Figs. 3, 4, and 5. An assessment of the direction and significance of the trends of the elements of the hydrological balance is also presented.

Due to the uncertainties associated with the scenarios and the rainfall-runoff modelling, it is not appropriate to describe the outputs from the projections for the individual basins in detail. Instead, it is more relevant to evaluate the overall picture of the possible changes expected in the long-term hydrological balance for particular periods and the directions of the differences between them and within them.

The most important finding is that the future predictions are practically the same for both scenarios. Both projections do not assume significant changes in the overall hydrological balance compared to the baseline. It is essential that these scenarios allow for an increase in precipitation. The rising air

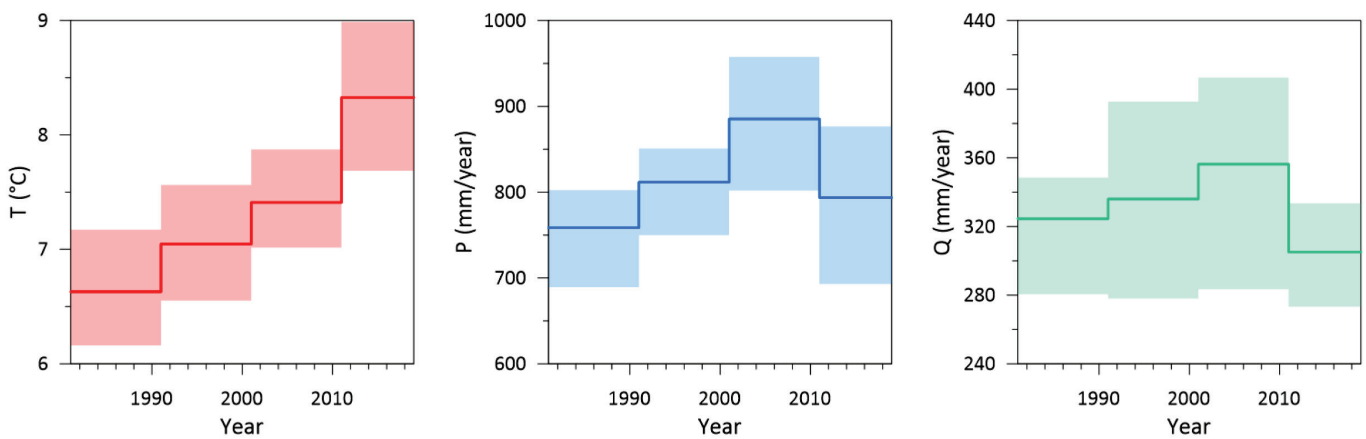

Fig. 2 *Changes in the hydroclimatic characteristics (long-term mean annual precipitation - P, air temperature - T, and runoff - Q) over four decades. The line represents the medians of these characteristics for each of the four periods (i.e., 1981-1990, 1991-2000, 2001-2010, and 2011-2019) for the eight river basins. The scatter (i.e., the 75th and 25th percentiles) indicates the variability between the basins.*

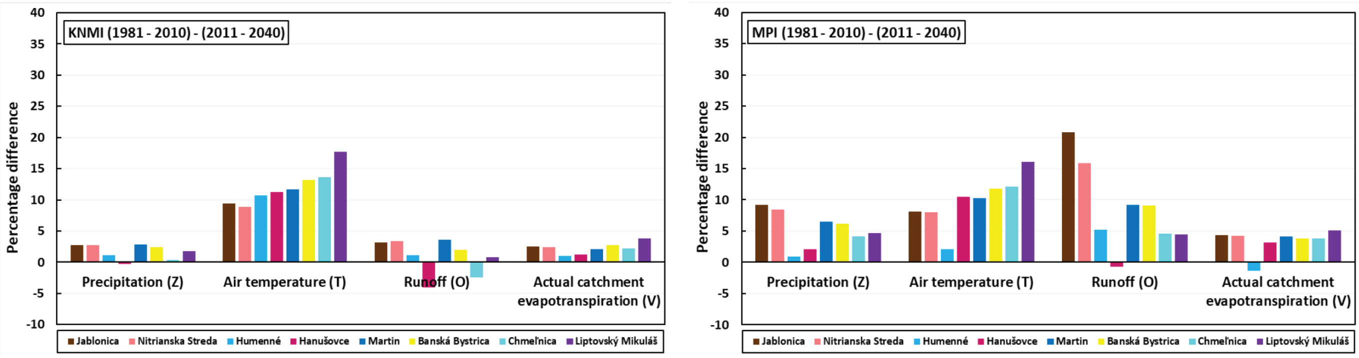

Fig. 3 *Comparison of changes in the values of elements of the hydrological balance for both scenarios (KNMI and MPI) in the pilot basins for 2011-2040 compared to the baseline period*

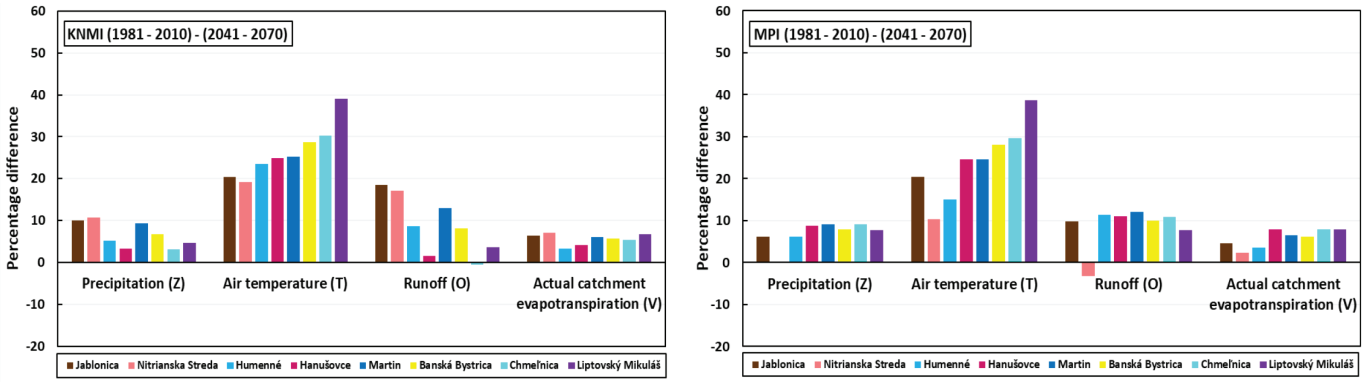

Fig. 4 *Comparison of changes in the values of the elements of the hydrological balance for both scenarios (KNMI and MPI) in the pilot basins for 2041-2070 compared to the baseline period*

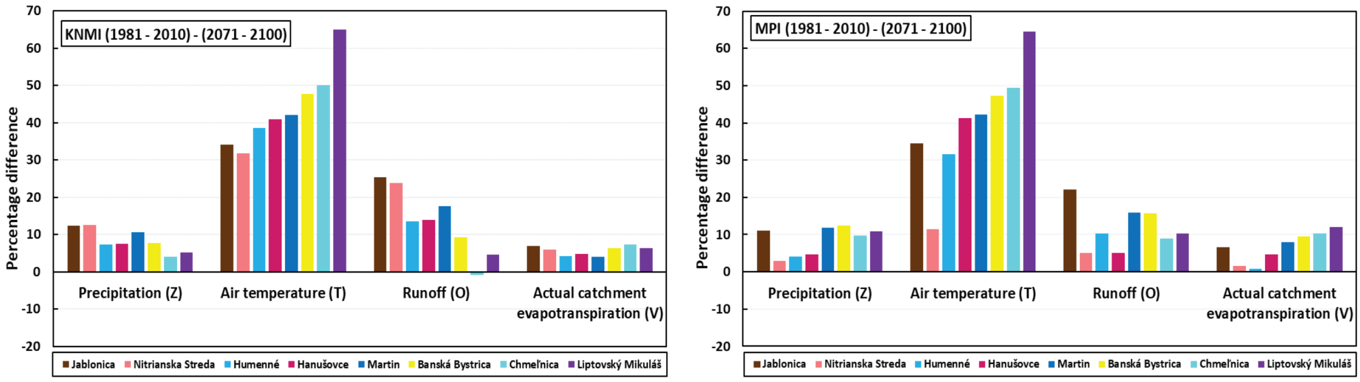

Fig. 5 *Comparison of changes in the values of the elements of the hydrological balance for both scenarios (KNMI and MPI) in the pilot basins for 2071-2100 compared to the baseline period*

temperature, which is not disputed, increases the territorial evaporation, but the increase in precipitation also enables the growth of the (long-term) average annual runoff. However, in this respect, it should be considered that both scenarios are based on the boundary conditions of the German ECHAM5 global circulation model.

The expected development of the long-term hydrological balance can be divided into two spatially divided groups of basins. These differ according to the share of runoff and territorial evapotranspiration based on the precipitation and in their vertical zonality. This division appears to the be same in both scenarios, as indicated in Figs. 6, 7, and 8.

The Myjava - Jablonica, Nitra – Nitrianska Streda, Turiec – Martin, and Váh – Liptovský Mikuláš basins show an increase

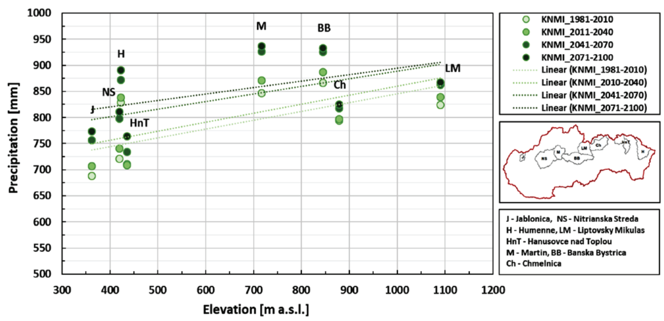

Fig. 6 *Analysis of the vertical zonality of the long-term averages of the precipitation totals in the pilot basins in relation to the average altitude of the pilot basins*

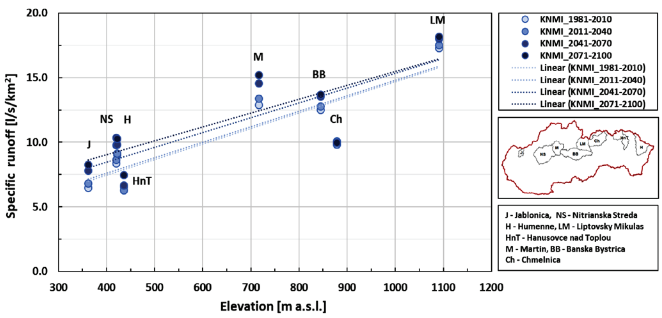

Fig. 7 *Relationship between the long-term average annual specific runoff and the average elevation of the pilot watersheds*

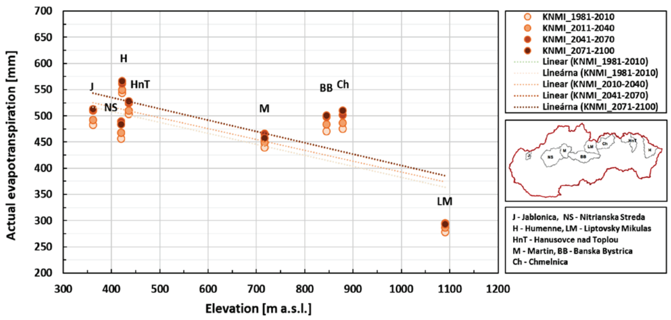

Fig. 8 *Relationship between long-term average annual actual catchment evapotranspiration and the average elevation of pilot watersheds*

in runoff and a decrease in territorial evaporation with increased altitudes. This is the same tendency that the basins on the western side of the Carpathian arc indicated in Keszeliová et al. (2021). The second group is formed by the catchments of Laborec - Humenné, Topľa – Hanušovce nad Topľou (east), Hron – Banská Bystrica, and Poprad – Chmeľnica (centre). The vertical zonality is preserved between the basins in the east and the centre but is not manifested within the regions.

When evaluating the trends of the hydrological balance components in the individual basins, we must remember that, over the long term, trends from thirty years cannot be considered representative. Here, we have mainly evaluated them by looking at an assessment of their significance (using the Mann-Kendall test at the 95 % level of significance). Tab. 2 contains an evaluative summary of the trends and their significance in the Váh catchment up to Liptovský Mikuláš for the baseline period (1981-2010) and all three thirty-year periods (2011–2040, 2041–2070, 2071–2100). Other basins were analyzed with the same approach too.

From this point of view, the "insignificant" evaluation prevails in Myjava - Jablonica, Laborec - Humenné, Hron – Banská Bystrica and Váh – Liptovský Mikuláš. On the other hand, significance prevails in the basins of Nitra – Nitrianska Streda and Topľa – Hanušovce nad Topľou, and there is a mixed picture in the basins of Poprad – Chmelnica and Turiec - Martin. As for the direction, we indicate that an increase in the range of average annual values prevails.

From a detailed analysis of the results of this study in an individual calendar month, the nature of the intra-annual distribution of the runoff does not differ from the results of similar studies in the Slovak Republic; the latest results were published by Sleziak et al. (2021) for the same set of basins using the same data. The general picture can be characterized relatively simply. The runoff increases at the beginning of the calendar year compared to the baseline scenario (the first two to four months). A similar picture occurs towards the end of the year, but the increase is not so significant (two to three months), and the flow is generally lower. In the rest of the year, a decrease in monthly flows can be expected compared to the baseline scenario. The difference between the rainfall and runoff shows a mirroring image of the fluctuations. However, when looking at the long-term balance, the two scenarios only signal a redistribution in the seasonality of the monthly flows. The overall balance does not deteriorate. Moreover, even an increase in the annual runoff (and total evapotranspiration) through all three periods in the future is possible.

4 DISCUSSION

Impact studies are inherently burdened by a cascade of uncertainties inherent in all steps of assessing the impact of climate change on runoff using hydrological modelling (e.g., Dankers and Kundzewicz, 2020), and their impact is linked. In the beginning, the uncertainties are inherent in the climate scenarios and their downscaling; the problems associated with determining the inputs and parameterising the rainfall-runoff models follow. To better quantify the uncertainties in the modelling chain, several authors have proposed to compare regional outputs from multi-scenario systematically and from multi-modelling simulations (Vetter et al., 2015; Hattermann et al., 2017, 2018; Krysanova and Hattermann, 2017; Krysanova et al., 2016, 2017). In our country, such approaches are still lacking.

Tab. 2 *Trends (positive – arrow up, negative - arrow down) and their statistical significance (YES or NO) at the 95 % level from the Mann-Kendall test in the series of the areal averages of the components of the hydrological balance (precipitation, air temperatures, runoff, actual catchment evapotranspiration) in the Váh catchment up to Liptovský Mikuláš for the baseline period (1981-2010) and all three periods in the future (2011–2040, 2041–2070, 2071–2100)*

Scenarios	Periods				Component of the hydrological balance
	1981-2010	2011-2040	2041-2070	2071-2100	
KNMI	↑ NO	↑ NO	↑ NO	↓ NO	Precipitation (Z)
	↓ NO	↑ YES	↑ YES	↑ YES	Air temperature (T)
	↑ NO	↓ NO	↑ NO	↓ NO	Runoff (O)
	↑ NO	↑ NO	↑ NO	↓ NO	Actual evapotranspiration (V)
MPI	↑ NO	↑ NO	↑ NO	↓ NO	Precipitation (Z)
	↑ NO	↑ YES	↑ NO	↑ YES	Air temperature (T)
	↑ NO	↑ NO	↑ NO	↓ NO	Runoff (O)
	↑ NO	↑ NO	↓ NO	↑ NO	Actual evapotranspiration (V)

From this point of view, the study presented has several defects. Regarding the structure and parameterization of the TUW model, we used conceptual rainfall-runoff modelling with a daily step. The use of the conceptual model is adequate because distributed r-r models that have proven themselves elsewhere in the region, such as WASIM and WETSPA, would bring about significant complications with parameterization and its dependence on climate change. The choice of daily steps has also limited the selection of scenarios. Scenario data that are downscaled to precipitation and climate stations with a daily step was necessary. Such data are usually not available from the available RCMs for the territory of Slovakia. There is a deficit in multi-emission and multi-RCM climate scenarios downscaled to the individual climate stations in Slovakia. To cope with the problem, regional climate models were selected with expert assistance in cooperation with specialists from the National Climate Program. The same applies to the SRES emission scenario. In doing so, the scope for evaluating the uncertainties of the outputs were consciously narrowed (but this applies to most imported studies from the recent past in the Slovak Republic). On the other hand, the selected models and the emission scenarios are considered to reproduce the climate of Slovakia's instrumental period adequately and were almost exclusively applied in the recent past in impact studies (e.g., Fendeková et al., 2018). However, the fact that new types of RCP emission scenarios are insufficiently applied in Slovakia could not be resolved.

Uncertainties associated with modelling runoff with conceptual models have long been known and discussed in the literature (e.g., Uhlenbrook et al., 1999). Methodological progress has been directed towards verifying and quantifying uncertainties caused by the models' structures and parameterization. Here, we avoided the complexity of such a solution by assuming that a model calibrated in a warmer period from the recent past could be sufficiently characteristic of the climate conditions in the future. The study from which the runoff modelling results were used (Sleziak et al., 2021) analyzed the calibration and cross-validation of the TUW model over several periods and showed that the calibration from the last warm period did not indicate acceptable validation results in less warm periods in the past. A similar conclusion was also valid for the opposite procedure. Therefore, we indirectly assumed that such a calibration would be suitable for a warmer future in our case.

5 CONCLUSIONS

From the point of view of the hydrological balance, the results signal the possibility of a change in the seasonal distribution of runoff. However, the changes in the long-term balance between future periods and the baseline were insignificant. Rather, the overall long-term balance could remain at the current level. In the hydrological balance with an annual step, the shift of the increased runoff to the winter and early spring appearing in our results compensates for the decrease in runoff and the increase in potential evaporation in summer. This is how the projections of both scenarios used appear, which to some extent, could increase the credibility of the findings. These results also support the plausibility of the downscaling and modelling. At the same time, however, they clearly show that since the common denominator of both scenarios is the same emission scenario and the same GCM, it will be necessary to introduce a multi-scenario assessment containing both extremes of the possible development of emissions.

The phenomenon that the overall hydrological balance may not significantly change appears less often in discussions about the impact of climate change on Slovakia's hydrological regime. Therefore, its confirmation or avoidance with a multi-scenario and multi-model approach would be more than necessary. For a viable proposal for climate change adaptation, it is essential to have a more comprehensive selection of emission and climate scenarios and parallel multi-model studies prevent our thinking from always being headed in the same direction.

Acknowledgements

This work was supported by the Slovak Research and Development Agency under Contracts Nos. APVV-19-0340 and APVV-20-0374; and VEGA 1/0782/21.

REFERENCES

Aleksić, M. - Sleziak, P. - Hlavčová, K. (2021) *Parameterization of the rainfall-runoff model in changing climate*. Pollack Period. Vol. 16, No. 3, pp. 64-69. DOI: https://doi.org/10.1556/606.2021.00340

Ardia, D. - Mullen, K. M. - Peterson, B. G. - Ulrich, J. (2016) '*DEoptim': Differential Evolution in 'R'.* R package version 2.2-4

Blaškovičová, L. - Jeneiová, K. - Poórová, J. - … - Paľušová, Z. (2019) *Determination of hydrological characteristics, sub-task: Hydrological Drought Assessment - Assessment of changes and trends of monthly and annual flow rates.* Unpublished report, Slovak Hydrometeorological Institute, p. 64.

Csáki, P. - Gyimóthy, K. - Kalicz, P. - Szolgay, J. - Zagyvai-Kiss, K. A. – Gribovszki, Z. (2020) *Multi-model climatic water balance prediction in the Zala River Basin (Hungary) based on a modified Budyko framework.* J. Hydrol. Hydromech., 68, 2020, 2, 200–210.DOI: 10.2478/johh-2020-0016

Dorigo, W. A. - Dietrich, S. - Aires, F. - … - Aich, V. (2021) *Closing the Water Cycle from Observations across Scales: Where Do We Stand?*, Bulletin of the American Meteorological Society, 102(10), E1897-E1935. DOI: 10.1175/BAMS-D-19-0316.1

Duethmann, D. - Blöschl G. (2018) *Why has catchment evaporation increased in the past 40 years? A data-based study in Austria. 2018*. Hydrology Earth System Sciences, 22 (10), pp. 5143-5158. DOI: https://doi.org/10.5194/hess-22-5143-2018

Ďurigová, M. - Hlavčová, K. - Komorníková, M. - Kalická, J. - Ballová, D. - Bacigál, T. (2019) *Analysis of changes in average monthly flow rates in Slovakia in recent decades*. Acta Hydrologica Slovaca. Vol. 20, No. 1, pp. 10-21. DOI: https://doi.org/10.31577/ahs-2019-0020.01.0002

Ďurigová, M. (2020) *Detection of changes in hydrometeorological time series under conditions of climate change in Slovakia* (in Slovak). Dissertation thesis. Faculty of Civil Engineering, Slovak University of Technology in Bratislava. SvF-104305-42099.

Fekete, B. M. - Vörösmarty, C. J. - Roads, J. O. - Willmott, C. J. (2004) *Uncertainties in precipitation and their impacts on runoff estimates.* Journal of Climate, 17(2), pp. 294-304. DOI: https://doi.org/10.1175/15200442(2004)017<0294:UIPATI>2.0.CO;2

Fendeková, M. - Poórová, J. - Slivová, V. - … - Vráblikova, D. (2018) *Hydrological drought in Slovakia and forecast of its development (in Slovak),* Comenius University in Bratislava, Faculty of Natural Sciences. 1st ed., 298 pp. ISBN 978-80-223-4510-1

Gao, H. - Tang, Q. - Ferguson, C. R. - Wood, E. F. - Lettenmaier, D. P. (2010) *Estimating the water budget of major US river basins via remote sensing*. International Journal of Remote Sensing 31 (14), pp. 3955-3978. DOI: https://doi.org/10.1080/01431161.2010.483488

Halmová, D. - Pekárová, P. - Bačová-Mitková, V. (2019) *Long-term trend changes of monthly and extreme discharges for different time periods*. Acta Hydrologica Slovaca Vol. 20, No. 2, pp. 122-130. DOI: https://doi.org/10.31577/ahs-2019-0020.02.0014

Hattermann, F. F. - Krysanova, V. - Gosling, S. N. - … - Samaniego, L. (2017) *Cross-scale intercomparison of climate change impacts simulated by regional and global hydrological models in eleven large river basins*. Climatic Change, 141, No. 3, pp. 561-576. DOI: https://doi.org/10.1007/s10584-016-1829-4

Hattermann, F. F. - Vetter, T. - Breuer, L. - … - Krysnaova, V. (2018) *Sources of uncertainty in hydrological climate impact assessment: a cross-scale study*. Environmental Research Letters, 13(1), 015006. DOI: 10.1088/1748-9326/aa9938

Hobbins, M. T. - Ramírez, J. A. - Brown, T. C. - Claessens, L. H. (2001) *The complementary relationship in estimation of regional evapotranspiration: The complementary relationship areal evapotranspiration and advection-aridity models.* 170 2001; Water Resour. Res. 37 (5), pp. 1367-1387. DOI: https://doi.org/10.1029/2000WR900358

Huang, Y. - Franssen, H. J. - Herbst, M. - Hirschi, M. - Michel, D. - Seneviratne, S. I. Teuling, A. J. - Vogt, R. - Detlef, S. - Pütz, T. - Vereecken, H. (2020) *Evaluation of different methods for gap filling of long-term actual evapotranspiration time series measured by lysimeters.* Vadose zone j. 2020; 19 (1). DOI: https://doi.org/10.1002/vzj2.20020

Keszeliová, A. - Hlavčová, K. - Danáčová, M. - Danáčová, Z. - Szolgay, J. (2021) *Detection of Changes in the Hydrological Balance in Seven River Basins Along the Western Carpathians in Slovakia.* Slovak Journal of Civil Engineering, Vol. 29, No. 4, 2021, pp. 49-60. DOI: https://doi.org/10.2478/sjce-2021-0027

Kramer, R. - Bounoua, L. - Zhang, P. - Wolfe, R. - Huntington, T. - Imhoff, M. - Thome, K. - Noyce, G. L. (2015) *Evapotranspiration Trends Over the Eastern United States During the 20th Century.* Hydrology 2 (2), pp. 93-111. DOI: https://doi.org/10.3390/hydrology2020093

Krysanova, V. - Hattermann, F. (2017) *Intercomparison of climate change impacts in 12 large river basins: overview of methods and summary of results.* Climatic Change, 141(3), pp. 363-379. DOI: 10.1007/s10584-017-1919-y

Krysanova, V. - Kundzewicz, Z. W. - Piniewski, M. (2016) *Assessment of climate change impacts on water resources*. Chap. 148. In: V. Singh, ed. Handbook of applied hydrology. 2nd ed. New York: McGraw-Hill.

Krysanova, V. - Vetter, T. - Eisner, S. - … - Hattermann, F. F. (2017) *Intercomparison of regional-scale hydrological models and climate change impacts projected for 12 large river basins worldwide—a synthesis*. Environmental Research Letters, 12(10), 105002. DOI: 10.1088/1748-9326/aa8359

Lapin, M. - Bašťák, I. - Gera, M. - Hrvol', J. - Kremler, M. - Melo, M. (2012) *New climate change scenarios for Slovakia based on global and regional general circulation models.* Acta Meteorol. Univ. Comen. 2012, 37, pp. 25-74.

Lapin, M. - Damborská, I. - Gera, M. - Melo, M. - Hrvoľ, J. (2016) *Potential and current evapotranspiration in Slovakia in the period 1951-2015 and scenarios of possible development until 2100*. In: Proceedings of the International Conference in Kutná Hora, 28.-29.4.2016. Soil and agricultural drought, Prague, VÚMOP, pp. 210-225. ISBN 978-80-87361-55-9.

Mastrotheodoros, T. - Pappas, Ch. - Molnár, P. - Burlando, P. - Manoli, G. - Parajka, J. et al. (2020) *More green and less blue water in the Alps during warmer summers.* Nat. Clim. Chang. 10 (2), pp. 155-161. DOI: https://doi.org/10.1038/s41558-019-0676-5

Mills, G. (2001) *Ireland's water budget - model validation and a greenhouse experiment.* Irish Geography 34 (2), pp. 124-134. https://doi.org/10.1080/00750770109555783

Minďáš, J. - Bartík, M. - Škvareninová, J. - Repiský, R. (2015) *Functional effects of forest ecosystems on water cycle - Slovakia case study.* J. For. Sci., 64: 331-339. DOI: https://doi.org/10.17221/46/2018-JFS

Milly, P. C. D. - Dunne, K. A. (2001) *Trends in evaporation and surface cooling in the Mississippi River Basin.* Geophys. Res. Lett. 28 (7), pp. 1219-1222. DOI: https://doi.org/10.1029/2000GL012321

Mullen, K. M. - Ardia, D. - Gil, D. - Windover, D. - Cline, J. (2011) *DEoptim: An R Package for Global Optimization by Differential Evolution.* Journal of Statistical Software, 40(6), pp. 1-26. DOI: http://www.jstatsoft.org/v40/i06/

Nash, J. E. - Sutcliffe, J. V. (1970) *River flow forecasting through conceptual models, part I-A: discussion of principles.* Journal of Hydrology, 10(3), pp. 282-290. DOI: https://doi:10.1016/0022-1694(70)90255-6

Parajka, J. - Szolgay J. - Mészároš, I. - Kostka, Z. (2004) *Grid-based mapping of the long-term mean annual potential and actual evapotranspiration in upper Hron river basin,* J. Hydrol. Hydromech., Vol. 52, 2004, No. 4, pp. 7 - 18.

Pellet, V. - Aires, F. - Munier, S. - Fernández Prieto, D. - Jordá, G. - Dorigo, W. A. - Polcher, J. - Brocca, L. (2019) *Integrating multiple satellite observations into a coherent dataset to monitor the full water cycle*—Application to the Mediterranean region. Hydrol. Earth Syst. Sci., 23, pp. 465-491. DOI: https://doi.org/10.5194/hess-23-465-2019

Popp, T. - Hegglin, M. I. - Hollmann, R. - … - Willén, U. (2020) *Consistency of Satellite Climate Data Records for Earth System Monitoring*. Bulletin of the American Meteorological Society, 101(11), E1948-E1971. DOI: https://doi.org/10.1175/BAMS-D-19-0127.1

Posada Gil, D. - Poveda G. (2020) *Consistency of Long-Term Trends and Closure of the Surface Water Balance in the Amazon River Basin*. Earth and Space Science Open Archive, pp. 1-22. DOI: https://doi.org/10.1002/essoar.10505844.1

Pramuk, B. - Pekárová, P. - Škoda, P. - Halmová, D. - Bačová Mitková, V. (2016) *The identification of changes in the regime of daily discharges in Slovakia.* Acta Hydrologica Slovaca, Vol. 17, No. 1, 2016, pp. 65 - 77.

Rodell, M. - Beaudoing, H. K. - L'Ecuyer, T. S. - … - Woodet, E. F. (2015) *The observed state of the water cycle in the early twenty-first century.* J. Climate, 28, 8289-8318. DOI: https://doi.org/10.1175/JCLI-D-14-00555.1

Rončák, P. - Šurda P. (2019) *Water balance estimation under a changing climate in the Turiec River basin.* Acta Hydrologica Slovaca, Vol. 20, No. 2, 2019, pp. 160-165. DOI: https://doi.org/10.31577/ahs-2019-0020.02.0019

Rončák, P. - Vitková, J. - Šurda P. (2019) *The components of water balance in changing climate in future horizons in Slovakia.* SGEM 2019 conference proceedings: 19th International Multidisciplinary Scientific GeoConference, Water Resources. Forest, Marine and Ocean Ecosystems, Sofia: STEF92 Technology, p. 545-552. DOI: 10.5593/sgem2019/3.1/S12.070

Safeeq, M. (2012) *Forests and Water in the Sierra Nevada: Kings River Experimental Watershed and Ecosystem Monitoring Project*. University of California Merced USDA Forest Service, PSW Research Station, Fresno, California.

Sleziak, P. - Szolgay, J. - Hlavčová, K. - Parajka, J. (2016) *The Impact of the Variability of Precipitation and Temperatures on the Efficiency of a Conceptual Rainfall-Runoff Model.* Slovak Journal of Civil Engineering, 2016, Vol. 24, pp. 1-7. DOI: 10.1515/sjce-2016-0016

Sleziak, P. - Szolgay, J. - Hlavčová, K. - Duethmann, D. - Parajka, J. - Danko, M. (2018) *Factors controlling alterations in the performance of a runoff model in changing climate conditions*. J. Hydrol. Hydromech. 2018, Vol. 66, pp. 381-392. DOI: https://doi.org/10.2478/johh-2018-0031

Sleziak, P. - Výleta, R. - Hlavčová, K. - Danáčová, M. - Aleksić, M. - Szolgay, J. - Kohnová, S. (2021) *A Hydrological Modeling Approach for Assessing the Impacts of Climate Change on Runoff Regimes in Slovakia*. Water 2021, 13, 3358. DOI: https://doi.org/10.3390/w13233358

Tomas-Burguera, M. - Beguería, S. - Vicente-Serrano, S. M. (2021) *Climatology and trends of reference evapotranspiration in Spain.* Int J. Climatol Vol. 41 (S1). DOI: https://doi.org/10.1002/joc.6817

Trenberth, K. E. - Smith, L. - Qian, T. - Dai, A. - Fasullo, J. (2007) *Estimates of the Global Water Budget and Its Annual Cycle Using Observational and Model Data*. Journal of Hydrometeorology 8 (4), pp. 758-769. DOI: https://doi.org/10.1175/JHM600.1

Ukkola, A. M. - Prentice, I. C. (2013) *A worldwide analysis of trends in water-balance evapotranspiration*. Hydrol. Earth Syst. Sci. 17 (10), pp. 4177-4187. DOI: https://doi.org/10.5194/hess-17-4177-2013.

Uhlenbrook, S. - Seibert, J. - Leibundgut, Ch. - Rodhe, A. (1999) *Prediction uncertainty of conceptual rainfall-runoff models caused by problems in identifying model parameters and structure.* Hydrological Sciences Journal, 44:5, pp. 779-797. DOI: https://doi.org/10.1080/02626669909492273

Vetter, T. - Huang, S. H. - Aich, V. - Yang, T. - Wang, X. - Krysanova, V. - Hattermann, F. (2015) *Multi-model climate impact assessment and intercomparison for three large-scale river basins on three continents*. Earth System Dynamics, 6(1), pp. 17-43. DOI: https://doi.org/10.5194/esd-6-17-2015

Wang, S. - Huang, J. - LI, J. - Rivera, A. - Mckenney, D. W. - Sheffield, J. (2014a) *Assessment of water budget for sixteen large drainage basins in Canada.* Journal of Hydrology, 512, pp. 1-15. DOI: https://doi.org/10.1016/j. jhydrol.2014.02.058

Wang, S. - Mckenney, D. W. - Shang, J. - Li, J. (2014b) *A national-scale assessment of long-term water budget closures for Canada's watersheds*. Journal of Geophysical Research-Atmospheres, 119(14), 8712- 8725. DOI: https://doi.org/10.1002/2014JD021951

Walter, M. T. - Wilks, D. S. - Parlange, J. - Schneider, R. L. (2004) *Increasing Evapotranspiration from the Coterminous United States.* J. Hydrometeor 5 (3), pp. 405-408. DOI: https://doi.org/10.1175/1525-7541(2004)005<0405:IEFTCU>2.0.CO;2.

Weingartner, R. - Viviroli, D. - Schädler, B. (2007) *Water resources in mountain regions: a methodological approach to assess the water balance in a highland-lowland system.* Hydrol. Process., 21 (5), pp. 578-585. DOI: https://doi.org/10.1002/hyp.6268

Xiao, M. - Gao, Ming - Vogel, Richard M. - Lettenmaier, Dennis P. (2020) *Runoff and Evapotranspiration Elasticities in the Western United States: Are They Consistent With Dooge's Complementary Relationship?* Water Resour. Res., Vol. 56, (8). https://doi.org/10.1029/2019WR026719

Zhang, K. - Kimball, J. S. - Nemani, R. R. - Running, S. W. (2010) *A continuous satellite-derived global record of land surface evapotranspiration from 1983 to 2006.* Water Resour. Res., Vol. 46, (9). DOI: https://doi.org/10.1029/2009WR008800